

# Derivation of land-surface backscatter signatures from SAR time series for flood and wetland delineation

DISSERTATION

eingereicht bei der  
Fakultät für Mathematik und Geoinformation  
der Technischen Universität Wien

zum Zwecke der Erlangung des akademischen Grades eines  
Doktors der Naturwissenschaften (Dr. rer. nat.)

von

Dipl.-Geoökologe Stefan Schlaffer

Matrikelnummer: 1029163

unter der Leitung von  
Prof. Dr. Wolfgang Wagner  
Department für Geodäsie und Geoinformation

Gutachter:

Prof. Dr. Nazzareno Pierdicca

Dr. habil. Laurent Pfister

Wien, am 25. Jänner 2017

Dipl.-Geoökol. Stefan Schlaffer





# Derivation of land-surface backscatter signatures from SAR time series for flood and wetland delineation

DISSERTATION

submitted to the  
Faculty of Mathematics and Geoinformation  
at the Vienna University of Technology

in partial fulfillment of the requirements for the degree of  
Doktor der Naturwissenschaften (Dr. rer. nat.)

by

Dipl.-Geoökologe Stefan Schlaffer  
Registration number: 1029163

under the supervision of  
Prof. Dr. Wolfgang Wagner  
Department of Geodesy and Geoinformation

Reviewers:

---

Prof. Dr. Nazzareno Pierdicca

---

Prof. Dr. Josef Jansa

Vienna, 25 January 2017

---

Dipl.-Geoökol. Stefan Schlaffer



# Eidesstattliche Erklärung

Hiermit erkläre ich, dass ich diese Arbeit selbstständig verfasst habe, dass ich die verwendeten Quellen und Hilfsmittel vollständig angegeben habe und dass ich die Stellen der Arbeit, die anderen Werken oder dem Internet im Wortlaut oder dem Sinn nach entnommen sind – einschließlich Tabellen, Karten und Abbildungen – in jedem Fall unter Angabe der Quelle als Entlehnung kenntlich gemacht habe.

Wien, Jänner 2017

.....

Stefan Schlaffer  
Florianstr. 3  
92224 Amberg  
Deutschland

Parts of this cumulative thesis have been published in peer-reviewed journals:

**Schlaffer, S.**, Matgen, P., Hollaus, M., Wagner, W., 2015. Flood detection from multi-temporal SAR data using harmonic analysis and change detection. *International Journal of Applied Earth Observation and Geoinformation*, 38: 15–24. doi:10.1016/j.jag.2014.12.001

**Schlaffer, S.**, Chini, M., Dettmering, D., Wagner, W., 2016. Mapping Wetlands in Zambia Using Seasonal Backscatter Signatures Derived from ENVISAT ASAR Time Series. *Remote Sensing*, 8: 402. doi:10.3390/rs8050402

**Schlaffer, S.**, Chini, M., Giustarini, L., Matgen, P., 2017. Probabilistic mapping of flood-induced backscatter changes in SAR time series. *International Journal of Applied Earth Observation and Geoinformation*, 56: 77–87. doi:10.1016/j.jag.2016.12.003

Parts of the work on this thesis have been carried out in the framework of the following research projects:

European Space Agency (ESA) Fully Automated Aqua Processing Processing Service (FAAPS), contract 4000105037/11/NL/US.

ESA Support To Science Element (STSE) Water Cycle Feasibility Study (WATCHFUL), contract 4000107122/12/I-NB.

Forschungsförderungsgesellschaft (FFG) Austrian Space Applications Program (ASAP) WetMon – Enabling an operational Sentinel-1 wetland monitoring service for the EODC, contract 848001.

# Acknowledgements

This thesis could not be complete without mentioning the people whose feedback and support helped me reach this point. First of all, I owe gratitude to my supervisor Wolfgang Wagner, whose door was always open for discussions. I would especially like to express my gratitude to Patrick Matgen, whose great feedback and support helped me find my way and were a constant source of motivation. My time in Luxembourg would not have been as productive without the collaboration with my colleagues there, foremost Marco Chini, Laura Giustarini and Renaud Hostache, who were so supportive and never tired of discussing new ideas and providing me with their comments. I also owe great debt to my other co-authors, Markus Hollaus and Denise Dettmering, for their valuable feedback and support. Furthermore, I am grateful for the interesting discussions with Daniel Sabel and Felix Greifeneder during their time at TU Vienna.

I also owe a great deal of gratitude to my friends Ronald Pöpl and Michael Hornacek, who showed such patience and gave me support in critical times along the way.

Finally, I thank my parents Christa and Wolfgang, whose love and support have accompanied me throughout my life and without whom I would not be where I am today.

I acknowledge the financial support of the Austrian Federal Ministry of Science, Research and Economy for funding my stay at Luxembourg Institute of Science and Technology through its Marietta Blau scholarship program.



# Abstract

Remote sensing plays an important role for mapping and monitoring of floods and wetlands. Synthetic aperture radars (SAR) are of special importance due to their ability to penetrate cloud cover and their high sensitivity to the occurrence of surface water and variations in soil moisture. During flood events this sensitivity typically leads to deviations from backscatter behaviour that is observed under non-flooded conditions. These alterations are typically mapped using change detection techniques in which the changes between a pre- and a post-flood SAR image are quantified and classified. However, a number of open research questions exist with respect to automatic detection of flood-induced backscatter changes: (i) in change detection, selection of a suitable pre-flood reference image is often not trivial. This is especially the case when user intervention should be minimised, a constraint often imposed by the requirements of automatic processing chains. (ii) Numerous studies have demonstrated the importance of seasonality in backscatter from different land-surface types, which is typically not addressed explicitly in change detection methodologies. (iii) A number of confounding factors exist that contribute to the overall uncertainty of the delineated flood extents, such as ambiguous radar signatures of different land-cover types and the contribution of speckle. Traditionally, binary flood maps include no information on the expected uncertainty introduced by these factors whereas more recently, flood mapping methodologies have been proposed that result in fuzzy or probabilistic flood maps.

The overall objective of this thesis is to address these open questions by introducing and evaluating a novel change detection framework for mapping flood-induced deviations from long-term backscattering behaviour. For this purpose, backscatter signatures were derived by characterising seasonality using harmonic analysis of ENVISAT Advanced SAR (ASAR) Wide Swath time series spanning multiple years ( $> 50$  scenes). The estimated harmonic model parameters were analysed and discussed for complex wetland areas in the context of ancillary data on hydrological and biophysical processes. The model residuals were used as a measure of the flood-induced deviation from average seasonal backscattering behaviour. Finally, a Bayesian approach was applied for deriving probabilistic flood maps from the residuals.

The results show that harmonic analysis of SAR time series can be effectively used for deriving seasonal signatures characteristic of different land-surface types. Moreover, the applicability of the model parameters for classifying different wetland backscattering classes is demonstrated. The use of the model residuals for delineating areas that were inundated during non-seasonal events indicates that seasonal harmonic model estimates can serve as a reliable

estimate of the seasonal backscattering behaviour a land surface would display under non-flooded conditions. The probabilistic flood mapping approach is shown to provide reliable maps and can be used for characterising uncertainty caused by some of the aforementioned factors.

In conclusion, the proposed approach provides a framework for characterising seasonal backscattering behaviour and detecting flood-induced backscatter changes in SAR time series. An outlook to using the proposed method in the context of novel SAR missions such as Sentinel-1 is provided.

**Keywords:** SAR, Floods, Wetlands, ENVISAT ASAR Wide Swath, Time series analysis, Hydrology

# Kurzfassung

Fernerkundung spielt eine wichtige Rolle bei der Kartierung und Überwachung von Überschwemmungsereignissen und Feuchtgebieten. Radarsensoren mit synthetischer Apertur (SAR) kommt hierbei eine besondere Bedeutung zu. Zum einen bieten diese die Möglichkeit, auch dichte Wolkendecken zu durchdringen und zum anderen besitzen sie eine hohe Sensitivität gegenüber dem Vorkommen von Oberflächenwasser sowie für Veränderungen im Bodenfeuchtezustand. Diese Sensitivität führt während Überschwemmungsereignissen zu starken Abweichungen von dem Rückstreuverhalten, welches eine Landoberfläche unter nicht-überschwemmten Bedingungen aufweisen würde. Solche Abweichungen werden für gewöhnlich mittels Change Detection kartiert, wobei Änderungen zwischen zwei SAR-Aufnahmen quantifiziert und klassifiziert werden. Dabei wird eine Aufnahme verwendet, die den Zustand während der Überschwemmung zeigt sowie eine Referenzaufnahme, die vor oder nach dem Ereignis, also unter nicht-überschwemmten Bedingungen, aufgenommen wurde.

Eine Reihe offener Fragen existiert jedoch bezüglich der automatischen Erkennung von Änderungen im Rückstreuverhalten, die durch Überschwemmungen erzeugt worden sind: (i) die Auswahl geeigneter Referenzaufnahmen für die Verwendung in Change Detection ist oft schwierig und kann nicht objektiv durchgeführt werden. Dies ist insbesondere dann von Bedeutung, wenn die Anzahl der nötigen Eingriffe seitens des Benutzers minimiert werden soll, was im Rahmen automatischer Prozessierungsketten oftmals der Fall ist. (ii) Eine Anzahl von Studien hat gezeigt, dass die Saisonalität im Rückstreukoeffizienten für verschiedene Landoberflächentypen von großer Bedeutung sein kann. Diese Saisonalität wird in Change-Detection-Ansätzen im Allgemeinen nicht explizit berücksichtigt. (iii) Eine Anzahl verschiedener Faktoren trägt zur Unsicherheit der abgeleiteten Überschwemmungskarten bei, so z.B. die zweideutigen Radarsignaturen verschiedener Landoberflächentypen sowie der Einfluss von Speckle. Traditionell enthalten binäre Überschwemmungskarten keine zusätzliche Information über die Unsicherheiten, welche aufgrund solcher Faktoren zu erwarten sind. In jüngerer Zeit hingegen wurden erstmals Karten mittels probabilistischer Methoden oder Fuzzy-Logik produziert, mittels derer einige solcher Unsicherheiten ausgedrückt werden können.

Die Zielsetzung dieser Dissertation ist die Beschreibung und Validierung einer Methodik zur Detektion und Kartierung plötzlicher Änderungen im SAR-Rückstreuverhalten, wie sie durch Überschwemmungen herbeigeführt werden können. In diesem Rahmen sollen die o.g. Fragen adressiert werden. Zu diesem Zweck wurden Rückstreusignaturen abgeleitet, indem die Saisonalität im Rückstreukoeffizienten auf Basis mehrjähriger SAR-Zeitreihen ( $> 50$  Szenen)

mittels eines harmonischen Modellansatzes charakterisiert wurde. Hierzu wurden ENVISAT Advanced SAR (ASAR) Wide-Swath-Zeitreihen verwendet. Die geschätzten Modellparameter wurden am Beispiel eines komplexen Feuchtgebietes analysiert und im Zusammenhang mit zusätzlichen Informationen zu hydrologischen und biophysikalischen Prozessen diskutiert. Die Modellresiduen wurden als Maß für die Abweichung vom langjährigen mittleren Rückstreuverhalten genutzt. Mittels eines Bayesschen Ansatzes wurde schließlich probabilistische Überschwemmungskarten abgeleitet.

Die Ergebnisse zeigen, dass harmonische Analyse einen effizienten Ansatz darstellt, um saisonale Rückstreusignaturen verschiedener Landoberflächentypen aus SAR-Zeitreihen abzuleiten. Weiterhin wurde die Anwendung der harmonischen Modellparameter für die Klassifizierung verschiedener Rückstreutypen in Feuchtgebieten demonstriert. Darüber hinaus zeigt die Anwendung der Modellresiduen für die Ableitung nicht-saisonal überschwemmter Gebiete, dass harmonische Modelle als eine angemessene Schätzung des mittleren saisonalen Rückstreukoeffizienten dienen können. Es wurde außerdem gezeigt, dass der probabilistische Ansatz zur Überschwemmungskartierung zuverlässige Karten erzeugt und zur Charakterisierung der Unsicherheit herangezogen werden kann, die durch einige der zuvor genannten Faktoren verursacht wird.

Der vorgestellte Ansatz bietet einen Rahmen, mittels dessen die Saisonalität im Rückstreuverhalten von Landoberflächen charakterisiert und Abweichungen davon detektiert werden können. Weiterhin werden mögliche Perspektiven im Hinblick auf neue SAR-Missionen wie z.B. Sentinel-1 aufgezeigt.

**Schlagwörter:** SAR, Überschwemmungen, Feuchtgebiete, ENVISAT ASAR Wide Swath, Zeitreihenanalyse, Hydrologie





# Contents

|          |   |           |
|----------|---|-----------|
| <b>1</b> | <b>Introduction</b>   | <b>1</b>  |
| 1.1      | Motivation . . . . .  | 1         |
| 1.2      | State-of-the-art . . . . .  | 2         |
| 1.2.1    | Flood delineation from SAR imagery . . . . .  | 2         |
| 1.2.2    | Backscatter temporal signatures . . . . .   | 6         |
| 1.3      | Objectives . . . . .  | 10        |
| 1.4      | Structure of the thesis . . . . .   | 11        |
| 1.5      | Material and methods . . . . .  | 12        |
| 1.5.1    | Backscatter seasonality characterisation . . . . .  | 12        |
| 1.5.2    | Flood extent classification . . . . .   | 15        |
| 1.5.3    | Data and pre-processing . . . . .   | 17        |
| 1.6      | Summary of the publications . . . . .   | 20        |
| 1.6.1    | Mapping wetlands in Zambia using seasonal back-scatter signatures derived from ENVISAT ASAR time series . . . . . | 20        |
| 1.6.2    | Flood detection from multi-temporal SAR data using harmonic analysis and change detection . . . . .               | 22        |
| 1.6.3    | Probabilistic mapping of flood-induced backscatter changes in SAR time series . . . . .                           | 23        |
| 1.6.4    | Author contributions . . . . .  | 24        |
| <b>2</b> | <b>Mapping wetlands in Zambia using seasonal backscatter signatures derived from ENVISAT ASAR time series</b>     | <b>25</b> |
| 2.1      | Introduction . . . . .  | 25        |
| 2.2      | Material and Methods . . . . .  | 29        |
| 2.2.1    | Study Area . . . . .  | 29        |
| 2.2.2    | Datasets and Pre-Processing . . . . .   | 31        |
| 2.2.3    | Data Analysis . . . . .   | 35        |
| 2.3      | Results and Discussion . . . . .  | 39        |
| 2.3.1    | Wetland Backscatter Signatures . . . . .  | 39        |
| 2.3.2    | Regional Mapping of Wetland Backscattering Classes . . . . .  | 48        |

|          |  |            |
|----------|--|------------|
| 2.4      | Conclusions . . . . .  | 51         |
| <b>3</b> | <b>Flood detection from multi-temporal SAR data using harmonic analysis and change detection</b> | <b>55</b>  |
| 3.1      | Introduction . . . . .   | 55         |
| 3.2      | Material and Methods . . . . .   | 59         |
| 3.2.1    | Harmonic analysis of SAR time series . . . . .   | 59         |
| 3.2.2    | Preprocessing . . . . .  | 60         |
| 3.2.3    | Flood delineation . . . . .  | 62         |
| 3.2.4    | Study area and datasets . . . . .  | 64         |
| 3.2.5    | Validation approach . . . . .  | 65         |
| 3.3      | Results and Discussion . . . . .   | 65         |
| 3.3.1    | Time-series analysis . . . . .   | 67         |
| 3.3.2    | Flood extent classification . . . . .  | 69         |
| 3.4      | Perspectives . . . . .   | 74         |
| 3.5      | Conclusions . . . . .  | 75         |
| <b>4</b> | <b>Probabilistic mapping of flood-induced backscatter changes in SAR time series</b>             | <b>77</b>  |
| 4.1      | Introduction . . . . .   | 77         |
| 4.2      | Methods . . . . .  | 80         |
| 4.2.1    | Flood probability estimation and classification . . . . .  | 81         |
| 4.2.2    | Data processing and parameter estimation . . . . .   | 81         |
| 4.2.3    | Test case and validation approach . . . . .  | 85         |
| 4.3      | Results and Discussion . . . . .   | 88         |
| 4.3.1    | Backscatter PDF for permanent water bodies and impact of $\theta_{\text{ref}}$ . . . . .         | 88         |
| 4.3.2    | Backscatter PDF for land . . . . .   | 89         |
| 4.3.3    | Flood probability maps . . . . .   | 92         |
| 4.4      | Conclusions . . . . .  | 95         |
| <b>5</b> | <b>Synthesis</b>   | <b>97</b>  |
| 5.1      | Scientific impact . . . . .  | 97         |
| 5.2      | Limitations . . . . .  | 99         |
| 5.3      | Perspectives . . . . .   | 100        |
|          | <b>Bibliography</b>  | <b>103</b> |

|   |  |     |
|---|--|-----|
| A | Supplementary figures to Chapter 2: Mapping wetlands in Zambia using seasonal backscatter signatures derived from ENVISAT ASAR time series | 125 |
| B | CV   | 133 |



# List of Figures

|     |   |    |
|-----|---|----|
| 1.1 | Conditional probability density functions of two normally distributed populations $F$ and $nF$ . . . . .  | 18 |
| 1.2 | Pre-processing chain applied to ENVISAT ASAR WS Level 1b data. . . . .  | 20 |
| 2.1 | (a) Location of the study area within the Zambezi and the Kafue River basins; (b) digital elevation model of the study area; (c) land cover. . . . .  | 30 |
| 2.2 | Mean monthly rainfall from WorldClim (Hijmans et al., 2005) for the Kafue River basin and mean monthly runoff at Itezhi-Tezhi for the period 1978–1991 (source: GRDC). . . . .                  | 31 |
| 2.3 | Mean Aqua MODIS NDVI with 250 m resolution (MYD13Q1) for September in the (a) Kafue Flats and (b) Lukanga Swamps along with location of AOIs. . . . .   | 31 |
| 2.4 | ENVISAT ASAR Wide Swath scenes acquired on (a) 10 November 2006 (dry season) and (b) 30 March 2007 (wet season). . . . .  | 33 |
| 2.5 | ASAR $\sigma^0$ time series for different local incidence angle ranges in AOIs $A$ – $F$ as well as soil moisture from ERA-Interim/Land and altimeter water heights in the Kafue Flats. . . . . | 41 |
| 2.6 | ASAR $\sigma^0$ time series for different local incidence angle ranges in AOI G (top) as well as soil moisture from ERA-Interim/Land and altimeter water heights in the Lukanga Swamps. . . . . | 42 |
| 2.7 | Fitted parameters $c_i$ , $s_i$ of harmonic model terms (a) $i = 1$ , (b) $i = 2$ and (c) $i = 3$ for the different AOIs $A$ – $F$ and $\theta$ ranges. . . . .                                 | 46 |
| 2.8 | RGB composite of harmonic terms derived for (a) $15^\circ < \theta \leq 25^\circ$ ; (b) $25^\circ < \theta \leq 35^\circ$ ; (c) $35^\circ < \theta \leq 45^\circ$ . . . . .                     | 49 |
| 2.9 | Result of wetlands classification for the entire study area and the Kafue Flats. . . . .  | 52 |
| 3.1 | Monthly rainfall at Pershore College. . . . .   | 65 |

|     |   |    |
|-----|---|----|
| 3.2 | (a) ASAR scene acquired 23 July 2007 over the Severn River. (b) Non-flood ASAR scene acquired 22 August 2005. (c) HAND index. . . . .   | 66 |
| 3.3 | Time series of $\sigma^0(30^\circ)$ , harmonic model fitted to all observations and harmonic model after excluding flood observations for two different points located in agricultural areas. . . . .   | 68 |
| 3.4 | $\sigma^0(30^\circ)$ in dB measured by ENVISAT ASAR on (a) 3 March 2007, (b) 17 January 2008 and (c) 18 January 2010 over the study area. . . . .   | 69 |
| 3.5 | (a) Standardised residuals of the harmonic model for the scene acquired over the Severn River on 23 July 2007. (b) Change in backscatter between 22 August 2005 and 23 July 2007. (c) Kernel densities for figure (a). (d) Kernel densities for figure (b). . . | 71 |
| 3.6 | Extracted flood extents for 23 July 2007 using (a) the harmonic model approach and (b) change detection. . . . .  | 72 |
| 3.7 | Detail of extracted flood extents around Tewkesbury for 23 July 2007 using the (a) harmonic model approach (b) and change detection. . . . .  | 73 |
| 4.1 | Location of the study area. . . . .   | 83 |
| 4.2 | Calibrated ENVISAT ASAR WS scenes acquired over the River Severn on 23 July 2007 at (a) 10:27 and (b) 21:53. (c) Reference map derived from airborne imagery acquired on 24 July 2007 at 11:30. . . . .   | 86 |
| 4.3 | Relationship between $\sigma^0$ and $\theta$ for a pixel sampled over (a) land and (b) permanent water. . . . .   | 89 |
| 4.4 | Histograms and estimated Gaussian probability density functions of $\sigma^0$ from permanent water bodies after normalisation to (a) $30^\circ$ and (b) $40^\circ$ . . . . .  | 90 |
| 4.5 | (a) Harmonic model residuals $\varepsilon$ for a single land pixel and centred samples from permanent water; (b) corresponding density functions. . . . .   | 91 |
| 4.6 | Flood probability maps for 23 July 2007 after normalisation to $\theta_{\text{ref}} = 40^\circ$ at (a) 10:27 and (b) 21:53 and after normalisation to $\theta_{\text{ref}} = 30^\circ$ at (c) 10:27 and (d) 21:53. . . . .                                      | 93 |
| 4.7 | Reliability diagrams referring to flood probability maps for 23 July 2007 (a) morning and (b) evening. . . . .  | 94 |

|     |   |     |
|-----|---|-----|
| 4.8 | Differences between $p_F$ and $f_F$ in the reference map after normalisation to $\theta_{\text{ref}} = 40^\circ$ at (a) 10:27 and (b) 21:53 and after normalisation to $\theta_{\text{ref}} = 30^\circ$ at (c) 10:27 and (d) 21:53. . . . .   | 95  |
| A.1 | Local incidence angles of ASAR scenes averaged over the Kafue Flats. . . . .  | 126 |
| A.2 | Harmonic model parameters (a) $\bar{\sigma}^0(15^\circ - 25^\circ)$ [dB], (b) $\bar{\sigma}^0(25^\circ - 35^\circ)$ [dB], (c) $\bar{\sigma}^0(35^\circ - 45^\circ)$ [dB], (d) $A_1(15^\circ - 25^\circ)$ [dB], (e) $A_1(25^\circ - 35^\circ)$ [dB], (f) $A_1(35^\circ - 45^\circ)$ [dB], (g) $\phi_1(15^\circ - 25^\circ)$ [DoY], (h) $\phi_1(25^\circ - 35^\circ)$ [DoY], (i) $\phi_1(35^\circ - 45^\circ)$ [DoY]. . . . . | 127 |
| A.3 | Harmonic model parameters (a) $A_2(15^\circ - 25^\circ)$ [dB], (b) $A_2(25^\circ - 35^\circ)$ [dB], (c) $A_2(35^\circ - 45^\circ)$ [dB], (d) $\phi_2(15^\circ - 25^\circ)$ [DoY], (e) $\phi_2(25^\circ - 35^\circ)$ [DoY], (f) $\phi_2(35^\circ - 45^\circ)$ [DoY]. . . . .   | 128 |
| A.4 | Harmonic model parameters (a) $A_3(15^\circ - 25^\circ)$ [dB], (b) $A_3(25^\circ - 35^\circ)$ [dB], (c) $A_3(35^\circ - 45^\circ)$ [dB], (d) $\phi_3(15^\circ - 25^\circ)$ [DoY], (e) $\phi_3(25^\circ - 35^\circ)$ [DoY], (f) $\phi_3(35^\circ - 45^\circ)$ [DoY]. . . . .   | 129 |
| A.5 | RGB composite of harmonic model components used for wetland extent mapping in the Kafue River Basin. . . . .  | 130 |
| A.6 | Box-Whisker-Plots of the Height Above Nearest Drainage (HAND) index for each of the derived classes. . . . .  | 131 |



# List of Tables

|     |   |    |
|-----|---|----|
| 1.1 | Characteristics of ENVISAT ASAR WS medium resolution imagery. . . . .   | 19 |
| 2.1 | Characteristics of selected AOIs. . . . .   | 36 |
| 2.2 | Estimated $\overline{\sigma^0}$ in dB for each AOI and different ranges of $\theta$ . . . . .                                       | 45 |
| 2.3 | Reclassification table. . . . .   | 50 |
| 3.1 | Aggregation scheme of CORINE land-cover classes into urban and open terrain. . . . .  | 67 |
| 3.2 | Producer's and user's accuracies for the water class across all land-cover classes and for urban and open areas separately. . . . . | 73 |
| 4.1 | <i>Rel</i> values obtained for the two ASAR scenes and different values of $\theta_{\text{ref}}$ . . . . .                          | 93 |



# List of Mathematical Symbols

|                            |   |
|----------------------------|---|
| $A_i$                      | Amplitude of $i$ -th harmonic term [dB]   |
| $b_l$                      | Centre of the $l$ -th bin   |
| $B_l$                      | $l$ -th bin   |
| $c_i$                      | Cosine coefficient of $i$ -th harmonic term [dB]  |
| $f_F$                      | Flooded fraction  |
| $f_i$                      | Frequency of $i$ -th harmonic [ $\text{yr}^{-1}$ ]  |
| $k$                        | Number of harmonic terms in harmonic model [-]  |
| $K$                        | Number of medoids used for clustering [-]   |
| $L$                        | Number of bins [-]  |
| $M$                        | Class separability index  |
| $n$                        | Number of 10-day time steps per year [-]  |
| $n_R$                      | Number of pixels in reference flood map [-]   |
| $n_{R,l}$                  | Number of pixels in reference flood map falling in probability bin $B_l$ [-]                  |
| $N$                        | Number of observations [-]  |
| $s_i$                      | Sine coefficient of $i$ -th harmonic term [dB]  |
| $s_\varepsilon$            | Standard deviation of residuals [dB]  |
| $t$                        | Time  |
| $\beta$                    | Dependency of $\sigma^0$ in terms of $\theta$ : $\beta = d\sigma^0/d\theta$ [dB deg $^{-1}$ ] |
| $\varepsilon$              | Harmonic model residual [dB]  |
| $\varepsilon^{\text{std}}$ | Standardised harmonic model residual [-]  |
| $\phi_i$                   | Phase angle of $i$ -th harmonic term [-]  |
| $\lambda$                  | Wavelength [cm]   |
| $\sigma^0$                 | Backscatter coefficient [dB]  |
| $\overline{\sigma^0}$      | Backscatter coefficient averaged over time $t$ [dB]   |
| $\hat{\sigma}^0$           | Harmonic model estimate of backscatter coefficient [dB]                                       |
| $\sigma_s^0$               | Backscatter contribution by the ground surface [dB]   |
| $\sigma_{sv}^0$            | Backscatter contribution by interactions between ground surface and vegetation [dB]           |
| $\sigma_v^0$               | Backscatter contribution by the vegetation [dB]   |

|                         |  |
|-------------------------|--|
| $\tau$                  | One-way transmissivity of the vegetation [-]                             |
| $\theta$                | Local incidence angle [deg]  |
| $\theta_{\text{ref}}$   | Reference local incidence angle for normalisation [deg]                  |
| $p(\varepsilon)$        | Probability density of $\varepsilon$                                     |
| $p(\varepsilon F)$      | Conditional probability density of $\varepsilon$ for a flooded pixel     |
| $p(\varepsilon nF)$     | Conditional probability density of $\varepsilon$ for a non-flooded pixel |
| $p(F)$                  | Prior probability of a pixel being flooded                               |
| $p(nF)$                 | Prior probability of a pixel not being flooded                           |
| $p(F \varepsilon), p_F$ | Posterior probability of a pixel being flooded given $\varepsilon$       |
| $p(o b_l)$              | Calibration function   |

# List of Acronyms

|        |  |
|--------|--|
| AOI    | Area of Interest                                       |
| ASAR   | Advanced Synthetic Aperture Radar                      |
| CCI    | Climate Change Initiative                              |
| CD     | Change Detection                                       |
| CLC    | CORINE Land Cover                                      |
| CORINE | Coordination of Information on the Environment         |
| DAHITI | Database for Hydrological Time Series of Inland Waters |
| DEM    | Digital Elevation Model                                |
| DOY    | Day of Year  |
| ECMWF  | European Centre for Medium-range Weather Forecasts     |
| ENL    | Equivalent Number of Looks                             |
| EO     | Earth Observation                                      |
| ERS    | European Remote Sensing Satellite                      |
| ESA    | European Space Agency                                  |
| GCP    | Ground Control Point                                   |
| GIEMS  | Global Inundation Extent from Multi-Satellites         |
| GPOD   | Grid Processing On Demand                              |
| GRDC   | Global Runoff Data Centre                              |
| HAND   | Height Above Nearest Drainage                          |
| HH     | Horizontal transmit – Horizontal receive               |
| HM     | Harmonic Model   |
| IWS    | Interferometric Wide Swath                             |
| JERS-1 | Japan Earth Resource Satellite 1                       |
| LiDAR  | Light Detection and Ranging                            |
| MODIS  | Moderate Resolution Imaging Spectrometer               |
| NDVI   | Normalised Difference Vegetation Index                 |
| NEST   | Next ESA SAR Toolbox                                   |
| PDF    | Probability Density Function                           |
| RA-2   | Radar Altimeter 2                                      |
| SAR    | Synthetic Aperture Radar                               |

|      |                                      |
|------|--------------------------------------|
| SRTM | Shuttle Radar Topography Mission     |
| UK   | United Kingdom                       |
| VV   | Vertical transmit – Vertical receive |
| WS   | Wide Swath                           |





# Chapter 1

## Introduction

### 1.1 Motivation

Floods are among the most frequent and devastating natural hazards. Based on reinsurance data it has been estimated that, between 1980 and 2015, hydrological extreme events accounted for 14% of disaster fatalities and losses amounting to more than 930 billion US\$ (MunichRe, 2016). A recent study places a number of almost 1 billion people in areas that are prone to river or coastal flooding with the highest numbers located in Asia (Jongman et al., 2012). A substantial increase in losses is to be expected due to population growth in flood-prone areas, especially in growing economies and developing countries, as well as climate change (Winsemius et al., 2015). In consequence, the Sendai Framework for Disaster Risk Reduction assigns high priority to the development and dissemination of scientific methods for disaster mapping, monitoring and forecasting (United Nations, 2015).

As the number of *in-situ* runoff monitoring stations is declining in many regions of the world (Vörösmarty, 2002), earth observation (EO) technology is becoming increasingly important as a source of information for mapping and monitoring of floods (Yan et al., 2015). Data acquired by airborne platforms typically are of high spatial resolution, however, only cover relatively small areas, are costly to acquire and systematic acquisition is often not possible. Spaceborne sensors, on the other hand, are characterised by coarser spatial resolution but larger footprints and often low revisit times (Di Baldassarre et al., 2011). In addition to their use in disaster management, EO data can be of benefit in flood forecasting, either by being used for calibrating hydraulic models (Schumann et al., 2013; Tarpanelli et al., 2013) or for data assimilation (García-Pintado et al., 2013; Matgen et al., 2010).

In contrast to optical systems, synthetic aperture radar (SAR) sensors can

be operated during day and night times and are relatively insensitive to extreme weather conditions due to their ability to penetrate clouds and heavy rainfall (Danklmayer et al., 2009). Examples include the two-satellite Sentinel-1 constellation of the European Space Agency (ESA) with a repeat cycle of six days (Torres et al., 2012) and the four-satellite COSMO-SkyMed constellation, which can provide high-resolution imagery at a revisit time as short as six hours (Covello et al., 2010). The amount of data generated by such novel missions makes it increasingly difficult for operators to produce flood maps using manual or semi-automated processing chains as these require a substantial amount of user interaction. As timeliness is critical for the use of EO-derived maps in disaster situations a central requirement for operational flood mapping services is the need for as little intervention by the operator as possible (Twele et al., 2016). Moreover, automatic procedures can help to increase the objectivity and reproducibility of the derived flooded areas (Matgen et al., 2011). However, so far only few fully automatic flood mapping frameworks have been proposed (e.g. Martinis et al., 2015; Twele et al., 2016; Westerhoff et al., 2013), while others require at least some interaction with the user (e.g. Pulvirenti et al., 2011b). In the following, the current state-of-the-art in flood delineation from SAR imagery is reviewed.

## 1.2 State-of-the-art

### 1.2.1 Flood delineation from SAR imagery

In SAR images, calm, open water bodies appear as dark areas due to their specular properties whereas land surfaces are typically composed of various types of scatterers leading to higher amounts of energy being returned to the radar antenna (Richards, 2009). As a result, SAR images often show high contrast between flooded and non-flooded land surfaces. Not surprisingly, numerous flood mapping approaches for medium and high-resolution SAR data have been proposed in recent years. The list of applied methodologies ranges from simple manual (Bartsch et al., 2012; Chini et al., 2013) and automatic radiometric thresholding (Schumann et al., 2009) to more elaborate techniques such as image grey-value distribution modelling and region growing (Giustarini et al., 2013; Matgen et al., 2011; Pulvirenti et al., 2016), modelling using active contours (Horritt et al., 2001), fuzzy set theory (Martinis and Twele, 2010; Pierdicca et al., 2008) and probabilistic methods (D’Addabbo et al., 2016; Giustarini et al., 2016; Refice et al., 2014; Westerhoff et al., 2013). It should be noted that this list is by no means exhaustive. Each of these approaches

holds its advantages and disadvantages in connection with different types of input data. While simple thresholding approaches yield acceptable results for medium-resolution imagery while being computationally inexpensive, context-sensitive approaches are more suitable for high-resolution imagery where high within-class variability might lead to noisy results using pixel-based approaches (Martinis et al., 2009).

Despite the aforementioned high contrast in SAR imagery between calm water surfaces and land areas, a number of factors can cause confusion between the two classes. Dry, bare areas, for example, display similar backscatter values as open water surfaces, which can lead to a substantial overestimation of the flood extent, e.g. in arid regions (O’Grady et al., 2011). Specular reflection properties have been found for smooth artificial surfaces, such as tarmac roads, airfields and parking lots (Giustarini et al., 2013). Vegetation protruding from the water surface as well as waves caused by wind and heavy rain, on the other hand, have the opposite effect on the classification as these factors can lead to increases in the backscatter coefficient,  $\sigma^0$ , by several dB depending on incidence angle, polarisation and wavelength (Santoro and Wegmüller, 2014). In the case of flooded vegetation,  $\sigma^0$  is typically elevated as a result of double-bounce scattering between the water surface and vertical vegetation parts such as trunks and stems. This effect is strongly influenced by the interaction between observation system parameters, such as wavelength, polarisation and incidence angle (Henderson and Lewis, 2008), with environmental parameters, such as vegetation structure and water level (Pulvirenti et al., 2011a). While longer wavelengths such as L-band are typically used for mapping flooded forests (e.g. Hess et al., 2003), C-band radar may be preferable in the presence of herbaceous vegetation (Zhang et al., 2016). In urban areas, flood delineation from SAR data is hampered by radar shadow and layover (Mason et al., 2014). Nevertheless, high-resolution data from platforms such as TerraSAR-X have successfully been applied to detect inundation in urban areas (Giustarini et al., 2013; Mason et al., 2010, 2014), while the use of coarser-resolution data typically leads to an underestimation of the flood extent, partly due to the occurrence of mixed pixels (Kuenzer et al., 2013b; Schumann et al., 2011). More recently, interferometric coherence has been used as a complementary source of information to map floods in urban settlements (Pulvirenti et al., 2016). Another factor contributing to potential misclassification is speckle which is a noise-like feature inherent to SAR imagery. It is a result of the coherent combination of the contributions of individual scatterers distributed within a resolution cell (Woodhouse, 2005). Speckle simulation studies have shown its impact on the quality of SAR-derived flood maps (Giustarini et al., 2015). The

influence of speckle typically is addressed during image pre-processing using image filtering or multilooking (Richards, 2009).

These different factors lead to uncertainties in SAR-based flood maps which can impact their subsequent use, e.g. for deriving water stages (Schumann et al., 2008) or calibrating hydraulic models (Di Baldassarre et al., 2009). Typical producer’s accuracy values that have been reported in the literature range between ca. 58% (Mason et al., 2010) and 81% in urban areas and between ca. 65% (O’Grady et al., 2011) and 90% (Mason et al., 2012) in open areas. For low-density boreal forests, producer’s accuracies  $> 73\%$  have been reported (Cohen et al., 2016). The variations in classification accuracies—which rarely exceed 90% (Grimaldi et al., 2016)—are a result of different combinations of image properties (e.g. spatial resolution), classification method and study area. The characterisation of these uncertainties would add to the value of EO-derived flood maps and may help to foster the use of remote sensing products in flood management and increase their usefulness for decision makers (Schumann et al., 2016). Moreover, for directly assimilating EO-derived flood maps into hydrodynamic models assimilation filters require a characterisation of the uncertainties associated with the observations in order to produce optimal estimates (Giustarini et al., 2016; Matgen et al., 2015).

The task of characterising these uncertainties has been addressed in recent years by introducing methodologies resulting in flood maps that show uncertain flood extents. In such cases, flood extents are typically coded as values in the interval  $[0,1]$ , where the extremes mark certainly non-flooded and flooded pixels and intermediate values quantify different degrees of uncertainty. Most of these approaches are based on fuzzy-set theory (Martinis and Twele, 2010; Pierdicca et al., 2008) and Bayes’ theorem (D’Addabbo et al., 2016; Giustarini et al., 2016; Westerhoff et al., 2013). For example, Pierdicca et al. (2008) applied different fuzzy membership functions to flood mapping from SAR images and to incorporate contextual information. However, different shapes and parameterisations of membership functions are possible and selection of a suitable set may not always be straightforward. A probabilistic approach to grey-value histogram modelling was used by Giustarini et al. (2016). The parameters of flooded and non-flooded probability density functions (PDFs) were estimated from a flood image based on the assumption that the image histogram is a mixture of two normally distributed populations, namely flooded and non-flooded pixels. Additionally, the authors introduced the reliability diagram (Wilks, 2011) as a tool for evaluating the quality of probabilistic flood maps.

When estimating the distribution parameters of backscatter from flooded and non-flooded areas based on single images, the  $\sigma^0$  PDF of non-flooded

pixels typically is a mixture of different land-cover types and, therefore, may be multimodal itself. A common approach in flood mapping to account for backscattering behaviour of different land surface types within a scene is change detection, i.e. by quantifying alterations in an observed variable such as intensity or backscatter coefficient  $\sigma^0$  (Mercier et al., 2009). Additionally, change detection makes it possible to separately classify permanent water and areas affected by a flood event. A considerable number of techniques can be found in the literature, some of which were reviewed by Lu et al. (2004). They can mainly be categorised in approaches that consist of classifying a change image, e.g. difference (Bruzzone and Fernández-Prieto, 2000; Long et al., 2014) or ratio images (Nagler and Rott, 2000), and post-classification comparison techniques (e.g. Munyati, 2000).

Simple change detection has yielded satisfying results by computing differences between a flood and a pre-flood image and applying threshold classifiers to the obtained change image (Long et al., 2014). However, manual thresholding often requires substantial intervention by the operator such as histogram inspection and, therefore, its use within automatic processing chains is limited. Moreover, robustness with respect to the aforementioned interfering factors such as water surface roughness is often not given. Matgen et al. (2011) have proposed an approach consisting of grey-value distribution modelling, region growing and change detection for classification refinement. The approach holds considerable potential for use in automatic processing chains and has later been adapted to high-resolution imagery from TerraSAR-X which has facilitated the mapping of flooding in urban areas (Giustarini et al., 2013). Approaches based on graph theory can also increase robustness in high-resolution imagery by taking into account contextual information (Frey et al., 2012; Martinis et al., 2011).

Nevertheless, selection of a suitable reference image is not a straightforward task as it should represent the best possible characterisation of the backscatter signatures found in the area of interest. At the same time, it should share the geometric properties of the flood image. In order to fulfil the first requirement the reference scene should have been acquired during the same season as the flood image (Hostache et al., 2012), especially in regions with a pronounced seasonality in soil moisture and vegetation growth, e.g. in the humid and semi-arid tropics (Dostálová et al., 2014). In combination with the often irregular coverage encountered with imagery from SAR sensors this can make the selection of an appropriate reference image a difficult and time-consuming task. So far, only few studies have addressed this problem, e.g. by proposing semi-automatic approaches for selecting reference scenes from an image archive

(Hostache et al., 2012).

The use of image time series spanning multiple years may offer ways to overcome the problem of selecting a suitable reference image. Westerhoff et al. (2013) introduced an approach that takes into account information from a large archive of historic SAR data. Conditional histograms of water and land backscatter intensity were built using the historic time series and a mask of permanent water bodies. After this training step, each  $\sigma^0$  observation was labelled as either pertaining to the land or the water population using a probabilistic approach. However, the quality of the obtained results was not evaluated with respect to an independent benchmark dataset. Moreover, the empirical histograms for the land class were trained using tiles of  $1^\circ \times 1^\circ$  size, thereby, losing information on spatial context and mixing information from a large number of different land-cover classes, some of which might exhibit similar backscatter characteristics as, e.g. open water bodies. This may offer an explanation for the observed misclassification in dry regions where water and land histograms overlapped. The mixing of different land-cover types may be avoided by only considering backscatter observations made at the same location and, thereby, in the same land-cover class, assuming no land-cover change during the observation period. Furthermore, the effect of seasonality in  $\sigma^0$  from land, which has been considered important for change detection by Hostache et al. (2012), was not taken into account. It should also be noted that the approach by Westerhoff et al. (2013) does not represent a change-detection approach *per se* as no distinction between permanent and flood water surfaces is made. Nevertheless, the study by Westerhoff et al. (2013) is one of the few studies to date in which the full amount of information contained in SAR time series has been used for mapping flood events.

Open questions, therefore, remain with respect to how backscatter signatures of non-flooded land surfaces can be reliably estimated for use as reference data in a change detection setting. In the following section, different methods are described for estimating land-surface backscatter signatures.

## 1.2.2 Backscatter temporal signatures

SAR backscatter from land surfaces is a product of the complex interactions of sensor parameters, such as polarisation, wavelength and viewing geometry, with different scattering mechanisms taking place at the Earth's surface, such as surface, sub-surface, volume or double-bounce scattering. The latter, in turn, are a function of land-surface properties, such as soil water content, vegetation structure and surface roughness (Richards, 2009). Backscatter  $\sigma^0$

from a vegetated land surface is often partitioned using an additive model (e.g. Attema and Ulaby, 1978)

$$\sigma^0 = \tau^2 \sigma_s^0 + \sigma_v^0 + \sigma_{sv}^0, \quad (1.1)$$

where  $\sigma_s^0$  and  $\sigma_v^0$  are the contributions of the ground surface and the vegetation, respectively,  $\tau^2$  is the two-way transmissivity of the vegetation and  $\sigma_{sv}^0$  represents the interaction between surface and vegetation, e.g. from double-bounce scattering. A flood event will typically affect the contributions of  $\sigma_s^0$  and  $\sigma_{sv}^0$  as a water layer will drastically alter the reflection properties of the ground surface (Kasischke and Bourgeau-Chavez, 1997). Under certain assumptions, parameters for modelling these individual contributions can be estimated from ground measurements, however, these are usually unavailable when moving beyond the site scale (Santoro et al., 2011). For example, Pulvirenti et al. (2011a) modelled X-band backscatter from bare soil and wheat plants at different growth stages (parameterised using plant height, density, biomass, stem radius and leaf area index) under flooded and non-flooded conditions using an electromagnetic model. The obtained backscatter signatures were compared to COSMO-SkyMed image time series acquired during and after a flood event and the obtained patterns were successfully related to the flood duration of different vegetated and bare-soil plots. In a study carried out for flooded boreal forests, Cohen et al. (2016) modelled X-band backscatter signatures as a function of canopy closure and tree height. Backscatter displayed relatively high sensitivity to flooding in the low-density forests present in the study area. In denser forests, longer wavelengths such as L-band are usually preferred for monitoring floods due to lower attenuation by the forest canopy (e.g. Hess et al., 2003). The significant responses to flooding resulted in high accuracy values for the classification of inundated boreal forests (Cohen et al., 2016).

For estimating the parameters of the applied scattering models, however, the studies made use of extensive information on vegetation and surface properties that had to be collected on the ground (Pulvirenti et al., 2011a) or derived from airborne laser scanning data (Cohen et al., 2016). For mapping purposes at larger scales and in automatic processing chains such data are typically not available. Statistical models, which are parameterised using information from time series, on the other hand, show great potential for characterising backscatter signatures of land surfaces in support of retrieving, e.g. soil moisture (Wagner et al., 1999a), forest cover (Quegan et al., 2000) and water bodies (Santoro and Wegmüller, 2014). During flood events,  $\sigma^0$  has been reported to suddenly decrease or increase, depending on the land cover of the observed

area (Martinis and Rieke, 2015). While different land surface types have been reported to show varying degrees of temporal stability in their backscatter behaviour (Wagner et al., 2008), a flood event can, therefore, be assumed to cause deviations from backscattering behaviour that would be expected under non-flooded conditions. In the following paragraphs, an overview of different approaches for backscatter signature estimation based on multi-temporal SAR imagery is provided.

Santoro et al. (2015) extracted descriptive statistics such as minimum backscatter and temporal variability from ENVISAT C-band SAR time series and applied them for mapping permanent water bodies at the global scale. In the case of pure water and land pixels, high classification accuracy was achieved while in regions with strong seasonal variations in surface water extent, the applied two-metric approach was found to be problematic as a simple indicator of temporal variability does not distinguish between seasonal changes in backscatter intensity and essentially random changes that occur over permanent water bodies due to wind-induced waves. In another study, a land-cover classification problem involving the classes urban areas, forests, water bodies and agricultural areas could be solved by using temporal variability and long-term interferometric coherence as input features to a neural network classifier. For the water class, the authors report confusion with agricultural fields as both classes exhibited both low coherence and high temporal variability in backscatter intensity (Bruzzone et al., 2004). Low coherence in agricultural areas is caused by differences in vegetation growth stage and movement of plant parts whereas over water surfaces waves lead to low coherence (Pulvirenti et al., 2016).

As mentioned before, the use of simple temporal variability features neglects the seasonal patterns present in SAR time series. While  $\sigma^0$  time series over water display high temporal variability, land surfaces are subject to seasonal changes in precipitation and temperature which in turn control soil moisture and vegetation growth and, thereby,  $\sigma^0$  as a result of equation 1.1. Indeed, distinct seasonal backscatter patterns have been reported for a wide range of different land-cover types and climates. In one of the first studies targeting the analysis of multi-temporal SAR data, Cihlar et al. (1992) analysed airborne C-band imagery acquired over Southern Canada during a full annual cycle and encountered characteristic seasonal signatures for different land-cover types. Backscatter from herbaceous vegetation showed high sensitivity with respect to changes in biomass. Forests displayed distinctly lower annual backscatter amplitude whereas urban areas had very low temporal dynamics. In a study carried out for the United Kingdom, non-forest areas as well as young

( $\leq 5$  years) forest stands displayed distinct seasonality in C-band  $\sigma^0$  as well as sensitivity to precipitation patterns.  $\sigma^0$  from old-growth pine stands, on the other hand, was more stable throughout the year. The differences were large enough for a successful forest/non-forest mapping based on descriptive time series statistics (Quegan et al., 2000). Blaes et al. (2007) analysed temporal C-band  $\sigma^0$  profiles of different crop types (e.g. winter wheat, sugar beet, maize, grassland) throughout a growing season. While some crops always showed higher or lower average  $\sigma^0$ , it was also possible to discern signal increases due to crop growth and decreases due to harvest. Saich and Borgeaud (2000) have reported that, while crop-characteristic temporal backscatter signatures carry over across subsequent years, significant anomalies can be caused by variations in rainfall, temperature and local incidence angle. Although sensors operated in C-band are typically regarded as less suitable than L-band for soil moisture mapping in densely forested areas Woodhouse et al. (1999) have reported that backscatter measured by the scatterometer on board the European Remote Sensing (ERS) satellite closely followed the seasonality in average precipitation over tropical forest. It is, however, not known whether this was due to variations in vegetation properties or in soil moisture. Strong seasonal cycles in  $\sigma^0$  have also been reported in other climate zones, e.g. in semi-arid and arid Africa due to wetting and drying (Dostálová et al., 2014), and in arctic regions, where it has been attributed mainly to frost and snow cover dynamics (Antonova et al., 2016).

In contrast to the time series analysis methods based on average backscatter and temporal variability previously applied to SAR data (e.g. Bruzzone et al., 2004; Quegan et al., 2000; Santoro et al., 2015), analysis in the frequency domain (Wilks, 2011) has the potential to provide additional information on the contributions of periodic processes occurring on different time scales to the overall temporal variability in  $\sigma^0$ . In optical remote sensing, Fourier analysis and other function fitting methods have been applied in a number of studies, for example with applications in derivation of land surface phenology (e.g. Brooks et al., 2012; Eastman et al., 2009), land-cover and vegetation type classification based on time-series similarity (Evans and Geerken, 2006; Lhermitte et al., 2008) and change detection (Verbesselt et al., 2010). Verbesselt et al. (2010) applied harmonic analysis to detect phenological changes in Normalised Difference Vegetation Index (NDVI) time series. By analysing the residuals, breakpoints with respect to seasonality and trend were detected. In a recent study aimed at the validation of soil moisture datasets derived from scatterometer and radiometer time series, seasonality has been addressed using harmonic function fitting (Pierdicca et al., 2015). As sinusoidal shapes have also been

reported for SAR backscatter time series in mid-latitudes (Cihlar et al., 1992) similar approaches may hold considerable potential for analysing backscatter behaviour under undisturbed conditions and for application in change detection frameworks for delineating floods.

### 1.3 Objectives

As shown in Section 1.2, major knowledge gaps exist with respect to automatic change detection in flood mapping which are summarised in the following:

- In change detection frameworks, backscatter behaviour under non-flooded conditions are typically assessed using a reference image acquired before the flood event. However, only very few studies have dealt with an objective selection of suitable reference images (e.g. Hostache et al., 2012). Recently, first attempts have been made to estimate backscattering behaviour under non-flooded conditions making use of the information contained in SAR time series, however, only a small number of studies has been carried out in this context.
- Previous studies have highlighted the importance of seasonal patterns in backscatter time series from land surfaces for deriving backscatter signatures. However, only few studies have explored the benefits of harnessing this information in comparison to the use of simpler indicators of temporal variability. Harmonic functions have been applied for studies on land-surface phenology and anomalies from average seasonal behaviour (e.g. Verbesselt et al., 2010) but so far not in the context of flood mapping using SAR data.
- The vast majority of flood mapping approaches yields binary maps showing flooded and non-flooded areas. However, uncertain flood maps, e.g. produced by probabilistic approaches, would add to the value of EO-derived flood maps and their use in decision making and flood forecasting. So far, only very few studies have been published that aim at including information derived from SAR time series in probabilistic flood mapping approaches (e.g. Westerhoff et al., 2013) and possible methodologies have only marginally been explored and validated.

In the light of these open questions, the main objective of this thesis is to introduce and evaluate a novel framework for mapping flood-induced deviations from SAR backscatter behaviour under non-flooded conditions. For

this purpose, long-term backscatter behaviour is characterised by analysing medium-resolution C-band SAR time series by means of a harmonic model. In detail, the following objectives are addressed:

1. characterisation of backscatter signatures of different land surface types using a harmonic model;
2. delineation of flooded areas based on deviations from long-term seasonal backscatter behaviour;
3. derivation of probabilistic flood maps from time series in order to characterise uncertainties in the classification of flooded areas.

A secondary aim is the application of the estimated time series parameters for delineating different land-surface and wetland types. It should be noted that only open flood water is addressed, whereas flooded vegetation or flooded urban areas are not within the scope of this study. An outline of the thesis is given in the following.

## 1.4 Structure of the thesis

As harmonic models have rarely been used for the analysis of SAR time series, the derived model parameters are first analysed and discussed for different land-surface types in the context of ancillary information on hydrological processes and vegetation cover. The potential of the derived backscatter signatures for discriminating different land-cover types based on their backscatter seasonality is explored.

After the analysis of the information content of the harmonic model parameters, the next step consists of an assessment of the potential of the harmonic model for modelling and delineating isolated flood events as deviations from non-flooded backscattering behaviour. As floods typically cause a shift in scattering mechanisms towards specular reflection or double-bounce scattering, a flood event which does not occur periodically will cause significant deviations from the harmonic model trained using “undisturbed” data. Therefore, an analysis of the harmonic model residuals is carried out to assess whether this shift in backscattering behaviour can be used for an accurate mapping of flooded areas. In this context, the idea of using a harmonic model as pre-flood reference image in a change detection framework is introduced. The results are evaluated with independent reference data and compared to a more traditional change detection approach, in which a pre-flood and a flood image are used.

Furthermore, the potential of the harmonic model for locating flood images in a SAR time series spanning multiple years is addressed.

Subsequently, the previously introduced change detection approach is extended using a probabilistic framework. The class-conditional probabilities of each backscatter observation are computed based on backscatter PDFs parameterised using multi-temporal SAR imagery. Such a probabilistic approach allows a characterisation of flood mapping uncertainties that arise due to water surface roughness, mixed pixels, etc.

This thesis is structured as follows: Chapter 1 introduces the study and describes the state-of-the-art in flood delineation and backscatter signature estimation. Furthermore, the applied methodology is outlined. Chapter 2 contains an assessment of the ability of the harmonic model to characterise seasonal backscatter variations in a river floodplain, which is characterised by complex hydrological and vegetational processes, and presents an application in wetland mapping. Chapter 3 introduces a change detection framework based on a harmonic model for flood delineation. This framework is extended in Chapter 4 by implementing a probabilistic change detection approach. Finally, Chapter 5 summarises the study and its scientific impact and identifies limitations and perspectives for future work with respect to current satellite missions.

## 1.5 Material and methods

### 1.5.1 Backscatter seasonality characterisation

In equation 1.1, the backscatter coefficient  $\sigma^0$  from a land surface is described as a result of the combination of the contributions from ground ( $\sigma_s^0$ ) and vegetation ( $\sigma_v^0$ ) layers as well as the interactions between ground and vertical structures ( $\sigma_{sv}^0$ ). Under non-flooded conditions,  $\sigma_v^0$  is influenced mainly by the vegetation growth stage, while  $\sigma_s^0$  and  $\sigma_{sv}^0$  are affected by the soil moisture state through its influence on soil reflection and backscattering (Wang et al., 1995). As both vegetation growth and soil moisture dynamics are governed by climatic forcing, a series of  $\sigma^0$  observations along a time scale  $t$  will show a strong periodic component and, therefore, can be written as

$$\begin{aligned}\sigma_s^0(t) &= \overline{\sigma_s^0} + \sigma_{s,\text{per}}^0(t) + \sigma_{s,\text{anom}}^0(t), \\ \sigma_v^0(t) &= \overline{\sigma_v^0} + \sigma_{v,\text{per}}^0(t) + \sigma_{v,\text{anom}}^0(t), \\ \sigma_{sv}^0(t) &= \overline{\sigma_{sv}^0} + \sigma_{sv,\text{per}}^0(t) + \sigma_{sv,\text{anom}}^0(t),\end{aligned}\tag{1.2}$$

where  $\overline{\sigma_s^0}$ ,  $\overline{\sigma_v^0}$  and  $\overline{\sigma_{sv}^0}$  are the backscatter contributions from ground surface, vegetation and ground-vegetation interactions averaged over time, respectively. Analogously,  $\sigma_{s,\text{per}}^0$ ,  $\sigma_{v,\text{per}}^0$  and  $\sigma_{sv,\text{per}}^0$  ( $\sigma_{s,\text{anom}}^0$ ,  $\sigma_{v,\text{anom}}^0$  and  $\sigma_{sv,\text{anom}}^0$ ) denote the periodic (non-periodic) portions of the  $\sigma^0$  contributions of ground surface, vegetation and ground-vegetation, respectively.

As the individual contributions of the terms in equation 1.1 are usually unknown,  $\sigma^0$  measured at time  $t$  can alternatively be simplified as

$$\sigma^0(t) = \overline{\sigma^0} + \sigma_{s,\text{per}}^0(t) + \sigma_{v,\text{per}}^0(t) + \sigma_{sv,\text{per}}^0(t) + \sigma_{\text{anom}}^0(t) \text{ and} \quad (1.3)$$

$$\sigma^0(t) = \overline{\sigma^0} + \sigma_{\text{per}}^0(t) + \sigma_{\text{anom}}^0(t), \quad (1.4)$$

where  $\overline{\sigma^0}$  is the backscatter coefficient averaged over  $t$  and  $\sigma_{\text{per}}^0$  ( $\sigma_{\text{anom}}^0$ ) denotes the combined periodic (non-periodic) variations from ground surface, vegetation and ground-vegetation interaction. While  $\sigma_{\text{per}}^0$  comprises variations between different seasons in “normal” years,  $\sigma_{\text{anom}}^0$  includes backscatter variations due to wetter or drier years as well as extreme events such as floods, which cause different scattering mechanisms like specular reflection to dominate the picture. Since the three periodic terms in equation 1.3 do not necessarily have the same sign and magnitude,  $\sigma_{\text{per}}^0(t)$  may have a shape that departs from a strictly sinusoidal function, e.g. by being asymmetric or showing secondary and tertiary maxima.

At this stage it should be noted that the intensity measured by the sensor, which is directly related to  $\sigma^0$ , also contains the multiplicative contribution of speckle. Speckle is a noise-like phenomenon inherent to coherent measuring techniques such as SAR and is caused by the combination of the contributions by individual scatterers within a resolution cell. Although speckle is a deterministic process, it is usually modelled as stochastic noise as the individual scatterers are unknown and can be assumed to be randomly distributed within a cell (Woodhouse, 2005). Different filtering techniques have been developed for restoring  $\sigma^0$  by filtering in the spatial (e.g. Lee, 1983; Lopes et al., 1993) and in the temporal domain (Quegan et al., 2000). The multiplicative speckle can be modelled as additive noise after carrying out a logarithmic transformation of the backscatter values (Dekker, 1998). SAR images are typically transformed to the decibel (dB) scale using

$$\sigma^0 [\text{dB}] = 10 \log_{10} \left( \sigma_{\text{lin}}^0 \right). \quad (1.5)$$

This conversion also strongly affects the distribution of speckle. While speckle on the linear scale is assumed to follow a Gamma distribution (Ulaby et al.,

1986), on the logarithmic scale it approaches a normal distribution as the number of looks increases (Xie et al., 2002). For simpler notation,  $\sigma^0$  will be assumed to be scaled in dB in the remainder of this text. As the non-periodic component  $\sigma_{\text{anom}}^0$  can also be assumed to be normally distributed, equation 1.4 can be written as an additive linear model:

$$\sigma^0(t) [\text{dB}] = \overline{\sigma^0} + \sigma_{\text{per}}^0(t) + \varepsilon(t), \quad (1.6)$$

where  $\varepsilon$  comprises both logarithmically transformed speckle as well as non-periodic variations  $\sigma_{\text{anom}}^0$ .

Periodic cycles can be mathematically expressed using a series of  $k$  trigonometric functions, each with a sine and a cosine term (Bloomfield, 2000), which means that equation 1.6 can be written as

$$\sigma^0(t) = \overline{\sigma^0} + \sum_{i=1}^k \left[ c_i \cos\left(\frac{2\pi it}{n}\right) + s_i \sin\left(\frac{2\pi it}{n}\right) \right] + \varepsilon(t) = \hat{\sigma}^0(t) + \varepsilon(t), \quad (1.7)$$

where  $c_i$ ,  $s_i$  are the cosine and sine coefficients, respectively, of the  $i$ -th harmonic term and  $n$  is the number of time steps per year. The  $k$  sinusoids represent cycles occurring with a frequency  $f_i = 1, 2, 3, \dots, k \text{ yr}^{-1}$ . The maximum which is possible for  $k$  is set by the Nyquist frequency, which is half the sampling rate of a signal, i.e.  $n/2$ . Below that number,  $k$  should be chosen high enough to reproduce the seasonality caused by the underlying climatic and vegetation growth processes. In a study on harmonic modelling of NDVI time series, a number of  $k = 3$  was used to resolve processes occurring at four-monthly cycles (Verbesselt et al., 2012). Moreover, higher-order harmonics can be used to model departures from sinusoidal behaviour such as the ones mentioned earlier in this section (Bloomfield, 2000). Since flood events typically occur at a much shorter time scale ( $< 1$  month), this number was also adopted here in order to minimise their effect on the parameter fitting. Equation 1.7 essentially represents a multiple linear regression model with offset  $\overline{\sigma^0}$  and predictors  $\cos(2\pi it/n)$  and  $\sin(2\pi it/n)$  (Wilks, 2011). The  $2k + 1$  parameters—namely  $\overline{\sigma^0}$ ,  $c_i$  and  $s_i$ —can be estimated using least-squares approximation since it was shown earlier that  $\varepsilon$  can be regarded as an additive, normally distributed residual term. In order to minimise the effect of unequal sampling on the parameter estimation, equation 1.7 was fitted to 10-day composites computed from the  $\sigma^0$  observations. It should also be noted that  $\hat{\sigma}^0$  represents a non-speckled estimate of the seasonal mean backscatter coefficient, as the averaging of many  $\sigma^0$  observations taken over time effectively removes

the contribution of speckle.

It should be noted that the described approach assumes that the time series is not affected by any changes that would alter its mean and variance, e.g. land-cover changes. For example, a change from agricultural land to urban area would likely result in a higher mean  $\sigma^0$  and lower temporal variability. In that case, two harmonic models would have to be fitted, one before and one for the period after the breakpoint.

### 1.5.2 Flood extent classification

As the proposed flood mapping approach is targeted to be used in automatic processing chains, one fundamental requirement for the classification of pixels as either flooded or non-flooded is a minimum of intervention by the operator. In the past, a considerable number of flood classification methods has been proposed for assigning class labels to pixels in SAR images. Most of them rely on the images displaying a multimodal histogram. The larger mode is typically composed of the contributions of different non-flooded land surfaces while the second (and possibly third etc.) mode is caused by the occurrence of flooded areas (Bartsch et al., 2008). In the simplest case, a threshold grey value is used as decision boundary for separating flooded from non-flooded pixels. As manual thresholding is often not practicable due to the requirement of minimal user interaction, automatic thresholding methods, such as the algorithms by Otsu (Otsu, 1979) and Kittler-Illingworth (Martinis et al., 2009), have been applied. If the multimodality of the flood or change image is not distinct—mainly because the flooded area is small in comparison to the image extent—different split-based approaches can be applied (Chini et al., 2016; Martinis et al., 2009).

As in this study the non-flood reference was estimated using a harmonic model (equation 1.7), the change in  $\sigma^0$  induced by the flood event is expressed by the residual term  $\varepsilon$  computed as

$$\varepsilon(t) = \sigma^0(t) - \hat{\sigma}^0(t), \quad (1.8)$$

where  $\hat{\sigma}^0(t)$  is the harmonic model estimate of  $\sigma^0(t)$ . When an agricultural land surface is flooded, it is assumed that  $\sigma^0$  will undergo a sudden drop as the dominant scattering mechanism changes from volume and/or surface scattering towards specular reflection, i.e.  $\varepsilon$  will become strongly negative for flooded areas while non-flooded pixels will assume values distributed around zero. As  $\hat{\sigma}^0$  is computed separately for each pixel, an image showing  $\varepsilon$  is

available for every time step  $t$ .

For classifying flooded areas, two principal ways are in general possible, which are explored in the framework of this study. In the first case, the image showing  $\varepsilon(t)$  can be treated like an image showing the difference between two dates. In this case, any of the methods mentioned in Section 1.2 suitable for change detection can be used for classification. In the presented work, Otsu's algorithm (Otsu, 1979) is applied as it represents a well-known and straightforward approach for finding an optimal threshold. It is based on the objective to maximise between-class variability while at the same time minimising within-class variance. Before this, the  $\varepsilon$  image is standardised by computing for each pixel  $p$  the ratio  $\varepsilon^{\text{std}}(p) = \varepsilon(p) / s_\varepsilon(p)$ , where  $s_\varepsilon(p)$  is the standard deviation of the  $\varepsilon$  time series at point  $p$ . This approach typically still suffers from the aforementioned limitation of missing bimodality of the  $\varepsilon^{\text{std}}$  image histogram if the flooded area is small in comparison to the full extent of the image. Therefore, areas of the  $\varepsilon^{\text{std}}$  image which could be regarded as being highly unlikely to be flooded due to their high elevation above the river are masked using a topography-derived mask. The Hand Above Nearest Drainage (HAND) index (Nobre et al., 2011; Rennó et al., 2008) is chosen for this purpose as it consists of a drainage-normalised and flowpath-coherent topographical map (Nobre et al., 2016) and retains the elevation units of the input digital elevation model. If large areas have a high elevation above the drainage network, the masking of such areas will lead to an increasingly bimodal  $\varepsilon^{\text{std}}$  histogram. In this study, HAND is derived from hydrologically consistent DEMs provided by the HYDROSHEDS project (Lehner et al., 2008). Details of the computation are given in Chapter 3.2 and by Rennó et al. (2008).

In the second case, statistical properties of flooded and non-flooded classes are estimated based on historic SAR data. For the classification, a probabilistic approach is applied, in which the flood probability of each backscatter value is computed based on Bayes' theorem. Under the assumption that a pixel at a certain point in time can have either state  $s = F$  (flooded) or  $s = nF$  (non-flooded) the posterior probability of the pixel belonging to class  $F$  given an observation  $x$  is defined as

$$p(F|x) = \frac{p(x|F)p(F)}{p(x)}, \quad (1.9)$$

where

$$p(x) = p(x|F)p(F) + p(x|nF)p(nF), \quad (1.10)$$

and  $p(x|F), p(x|nF)$  are the conditional PDFs of making the observation  $x$

when the pixel is flooded and non-flooded, respectively.  $p(x)$  is the probability density of  $x$  when the pixel is either flooded or non-flooded and  $p(F)$  represents our prior knowledge about the probability of the pixel being flooded. If no prior information is available, a so-called non-informative prior can be used, i.e.  $p(F) = p(nF) = 0.5$ . This has been done by several authors in the past (Giustarini et al., 2016; Westerhoff et al., 2013). The idea is illustrated in Figure 1.1 for two classes with normally distributed features  $x$  with different class means ( $m_F, m_{nF}$ ) and equal variances ( $s_F^2 = s_{nF}^2$ ). The optimal decision boundary is located at the intersection of the class conditional PDFs. For SAR, the place of the observable  $x$  can be filled by  $\sigma^0$  or, for example,  $\Delta\sigma^0$  if a difference image is used. In this case, as harmonic model residuals  $\varepsilon$  are used, equation 1.9 can be written for each pixel  $P$  and time step  $t$  as

$$p(F|\varepsilon[P, t]) = \frac{p(\varepsilon[P, t]) p(F)}{p(\varepsilon[P, t]|F) p(F) + p(\varepsilon[P, t]|nF) p(nF)}. \quad (1.11)$$

As a result, a probabilistic flood map is obtained. In order to convert the probabilistic map into a binary (flooded/non-flooded) map the pixels are typically labelled with the more probable flooding state by applying a threshold  $p(F|\varepsilon) = 0.5$  (Duda et al., 2001).

### 1.5.3 Data and pre-processing

In Section 1.5.1, a harmonic model approach has been introduced for characterising periodic variations in SAR time series. However, a time series comprising at least one full annual cycle is needed for estimating the parameters in equation 1.7. For mapping non-periodic flood events, where the influence of floods on the harmonic model is to be minimised, even longer time series are required. As SAR sensors are typically capable of different acquisition modes and their application is often user-request driven, the number of SAR missions suitable for constructing such time series is limited. The two-satellite Sentinel-1 constellation, whose satellites were launched by ESA in 2014 and 2016, is a prime candidate for acquiring such time series. Its SAR sensor operates in C-band with a wavelength  $\lambda \approx 5.5$  cm and is acquiring mainly in its Interferometric Wide Swath (IWS) mode over land surfaces. The swath width of 250 km along with the short revisit cycles of the two satellites leads to a worst-case sampling interval of 6 days while maintaining a relatively high spatial resolution of ca. 20 m (Torres et al., 2012).

However, due to the very recent launch of the Sentinel-1 constellation, time series of sufficient length are not yet fully available. Moreover, historic SAR

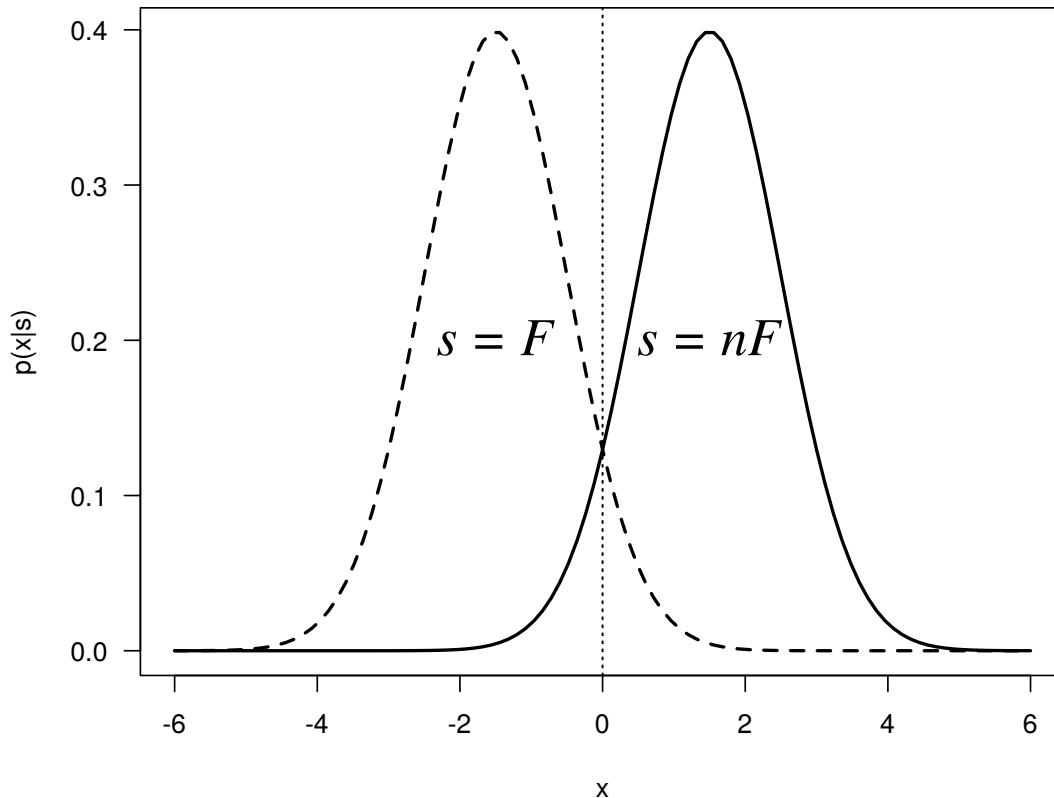


Figure 1.1: Conditional probability density functions of two normally distributed populations  $F$  and  $nF$  with means  $m_F = -1.5$ ,  $m_{nF} = 1.5$  and variances  $s_F^2 = s_{nF}^2 = 1$ . The vertical dotted line represents the optimal decision boundary.

data offer the possibility of testing new approaches for past flood events and validating the obtained results with high-resolution observations. The Advanced SAR (ASAR) sensor on-board ENVISAT was operated between 2002 and 2012 in C-band and is seen as the predecessor of Sentinel-1 with lower radiometric, temporal and spatial resolutions. Imagery acquired in Wide Swath (WS) mode has a spatial resolution of ca. 150 m and a large swath width of 400 km. In terms of radiometric resolution, the equivalent number of looks (ENL) is estimated to be  $> 15$  (ESA, 2012). Available polarisation configurations are predominantly VV and HH while Sentinel-1 mostly uses VV polarisation for land surfaces. Additional characteristics of ASAR WS data are shown in Table 1.1. Data for the period 2005 to 2012 was available for download from ESA's Grid Processing On Demand (GPOD) facility. For each of the study areas described in Chapters 2 to 4, the full time series of level 1b datasets was downloaded from GPOD.

Table 1.1: Characteristics of ENVISAT ASAR WS medium resolution imagery (after Desnos et al., 2000; ESA, 2012).

| Property               | Value                                 |
|------------------------|---------------------------------------|
| Frequency              | 5.331 GHz ( $\lambda \approx 5.6$ cm) |
| Polarisation           | VV or HH                              |
| Processing level       | Level 1b, ground-range detected       |
| Spatial resolution     | ca. 150 m                             |
| Pixel spacing          | 75 m                                  |
| Swath width            | 400 km                                |
| Temporal frequency     | irregular, ca. 7 days                 |
| ENL                    | > 15                                  |
| Radiometric resolution | < 1 dB                                |
| Incidence angle range  | 15°–45°                               |

Before the time series analysis described in Section 1.5.1 can be carried out, the downloaded scenes are pre-processed. A flowchart of the pre-processing chain used throughout this thesis is shown in Figure 1.2. Most of the pre-processing steps are carried out using the Next ESA SAR Toolbox (NEST). The level 1b datasets are first geocoded and terrain-corrected using the Range-Doppler method (Small and Schubert, 2008). As this approach requires precise knowledge about the position of the satellite at the time of image acquisition, verified DORIS orbit vectors (ESA, 2008) are used whenever available. After this step, the obtained terrain-corrected  $\sigma^0$  images are co-registered to a common grid with a spatial sampling interval of 2.3“ (Sabel et al., 2012), corresponding to approximately 75 m at the equator. The co-registration consists of two main steps, a cross-correlation and a image warping step. During the first step, the cross-correlation between each image and a master image is computed for windows of  $64 \times 64$  pixels around a number of ground control points (GCPs). The number of selected GCPs depends on the size of the area of interest. During the second step, a linear warping function is calibrated based on the displacement between the GCPs.

As ASAR WS scenes are characterised by a large swath width of 400 km scenes from different tracks are used to construct a time series of sufficiently dense sampling steps. Due to these different viewing geometries  $\sigma^0$  has been acquired from a range of local incidence angles  $\theta$  for each pixel in the co-

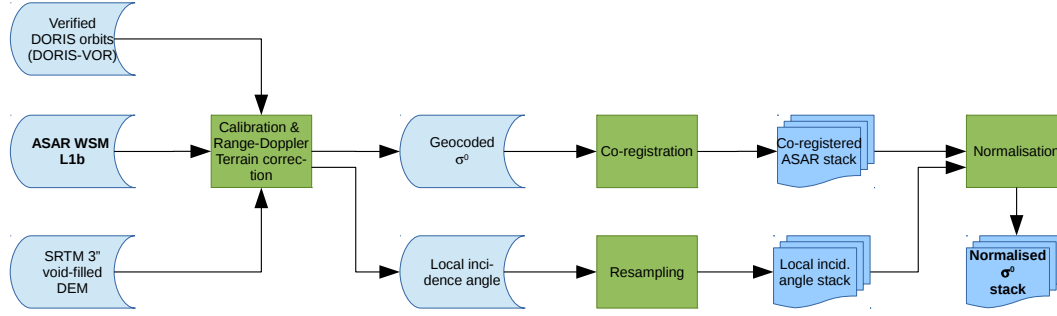


Figure 1.2: Pre-processing chain applied to ENVISAT ASAR WS Level 1b data.

registered stack. The effect of differences in  $\theta$  on  $\sigma^0$  has been described by different authors (Sabel et al., 2012; Van doninck et al., 2014; Wagner et al., 1999c) and is corrected for using the linear relationship

$$\sigma^0(\theta_{\text{ref}}) = \sigma^0 - \beta (\theta - \theta_{\text{ref}}), \quad (1.12)$$

where  $\theta_{\text{ref}}$  is a reference local incidence angle to which the backscatter coefficient is normalised, typically in the range  $30^\circ \leq \theta_{\text{ref}} \leq 40^\circ$ , and  $\beta = d\sigma^0 / d\theta$  (Pathe et al., 2009; Wagner et al., 1999c).  $\beta$  is calibrated separately for the time series of each pixel in the stack using linear regression over the  $\sigma^0$ - $\theta$  pairs. As a result of the pre-processing chain shown in Figure 1.2, a stack of  $\sigma^0$  images normalised to  $\theta_{\text{ref}}$  is obtained which is used as input dataset for the analysis described in Section 1.5.1.

## 1.6 Summary of the publications

This cumulative thesis is largely based on three publications that were produced while carrying out the work on this thesis. All of them have been published in peer-reviewed journals. The applied methods and key findings are summarised in the following.

### 1.6.1 Mapping wetlands in Zambia using seasonal backscatter signatures derived from ENVISAT ASAR time series

The first publication (Schlaffer et al., 2016, Chapter 2) establishes harmonic modelling as a means for characterising  $\sigma^0$  behaviour of different land-cover

types based on SAR image time series. As SAR time series have so far mainly been analysed in terms of average annual backscatter and temporal variability there is still a need for formalised methodologies for analysing  $\sigma^0$  time series and interpreting the derived parameters.

An archive consisting of  $> 100$  ENVISAT ASAR WS scenes acquired in HH polarisation over the course of ca. two years over a complex landscape in central Zambia was used as input data. The study area is characterised by semi-arid climate and comprises a wide range of ecosystems such as savannah, forests, agricultural areas and several seasonally and permanently flooded wetlands. The time series were analysed using the methodology describes in Section 1.5.1 and the derived harmonic model coefficients (amplitudes and phases) were discussed in the context of vegetation cover and hydrological processes. Vegetation cover was estimated based on dry-season MODIS NDVI while the runoff regime was characterised using water heights derived from radar altimetry time series. Furthermore, information on soil moisture seasonality was available from the ERA-Interim reanalysis dataset. As local incidence angle  $\theta$  has been reported to affect the sensitivity of  $\sigma^0$  towards variations in soil moisture (e.g. Van doninck et al., 2014) and flooding in the presence of vegetation (Lang et al., 2008; Pulvirenti et al., 2011a) as well as towards variations in water surface roughness (Töyrä et al., 2001), harmonic model estimates were derived for different  $\theta$  ranges. As the last step of the analysis, the separability of different wetland from non-wetland classes was tested using an unsupervised classification approach.

Distinct seasonal signatures were derived for permanent water bodies, seasonal open water, persistently flooded vegetation and seasonally flooded vegetation. Moreover, non-flooded forest and non-forest areas showed notable differences in their corresponding annual  $\sigma^0$  amplitudes. The results, on the one hand, confirmed previous studies that the use of multi-temporal indices derived from SAR imagery covering full seasonal cycles results in a high separability of different land-surface types based on their seasonal signatures. On the other hand, the harmonic model parameters derived for different  $\theta$  ranges showed that in most cases the influence of  $\theta$  was reduced to a linear offset in average annual backscatter whereas it had been hypothesised that the changes in the dominant scattering mechanism typically encountered in wetlands—e.g. between volume scattering, specular reflection and double-bounce scattering—would lead to non-linear relationships. Therefore, it is concluded that, in most cases, a linear correction such as defined in equation 1.12 would suffice for fusing imagery acquired with different viewing geometries. This holds important implications for the analysis carried out in the subsequent Chapters.

### 1.6.2 Flood detection from multi-temporal SAR data using harmonic analysis and change detection

In the second publication (Schlaffer et al., 2015, Chapter 3), a change detection framework for detecting and delineating floods as outliers from backscattering behaviour under non-flooded conditions is introduced. Backscatter signatures were estimated using a harmonic model which was fitted to a time series of 518 ASAR WS scenes acquired in VV polarisation over the lower River Severn catchment in the south-western United Kingdom. As the images were acquired from different viewing geometries backscatter values had been normalised with respect to the influence of  $\theta$  using equation 1.12. The study then focused on the analysis of the model residuals whose magnitudes were used as a proxy for the occurrence of floods. The image time series covered the time period between 2005 and 2012. During this period, the study area experienced several large-scale flood events which were recognisable in the time series of residuals as outliers with negative sign. Exclusion of the flood images identified using this method further showed that the impact of the outliers on the harmonic model fitting is negligible as long as only a small proportion of the images was acquired during flood events.

The delineation of flooded areas was carried out by first standardising the model residuals and then applying an automatic thresholding algorithm. As the performance of histogram-based thresholding methods strongly depends on the bimodality of the grey-value distribution (Martinis et al., 2009; Nakmuenwai et al., 2017), and, therefore, the size of the flood extent relative to the image size, a masking approach was applied. Areas which were assumed to be unlikely to be flooded due to their topographical location were masked based on the Height Above Nearest Drainage (HAND) index. Moreover, masking areas with high HAND values visibly increased the bimodality of the image and improved the estimation of the optimal threshold. In addition, change detection is carried out using a more traditional approach by computing the difference between a pre-flood and a flood image. The pre-flood image was identified using a semi-automatic approach (Hostache et al., 2012). The HAND-based masking of non-flood-prone areas had a similar effect on the threshold estimation as in the approach using the harmonic model. Nevertheless, the harmonic model-based change image showed higher contrast resulting in consistently higher producer's and user's accuracies. This is likely to be a result of the fact that the harmonic model estimate  $\hat{\sigma}^0(t)$  represents an non-speckled estimate of  $\sigma_{\text{per}}^0(t)$  due to the averaging of many backscatter measurements in the time series. The traditional change image produced by differencing between two

images, on the other hand, includes the speckle contributions of both images resulting in a higher overall noise.

The results highlight the applicability of harmonic model-based backscatter analysis for being used in change detection frameworks. Nevertheless, the final classification of flooded pixels was strongly affected by the number of non-flooded pixels that were masked based on HAND. Notably different results with lower accuracy may, therefore, be obtained in areas with less pronounced topography. This lesson is addressed in the subsequent Chapter of the thesis.

### 1.6.3 Probabilistic mapping of flood-induced backscatter changes in SAR time series

The third publication (Schlaffer et al., 2017, Chapter 4) generalises the change detection framework introduced in the previous chapter. Whereas in Chapter 3, flooded pixels were classified using an automatic thresholding algorithm applied to the residual image a pixel-wise probabilistic approach is used here. The advantages of a probabilistic approach include a classification based on the statistical properties of the classes and the characterisation of uncertainties with respect to the obtained flood extents. As input dataset, an extended version of the SAR dataset described in Chapter 3 was used. The PDFs of the flooded and non-flooded classes were parameterised separately for each pixel using the information contained in the corresponding  $\sigma^0$  time series. Seasonal backscatter behaviour in non-flooded pixels was accounted for using the previously introduced harmonic model approach. The PDF of  $\sigma^0$  for flooded areas was approximated using  $\sigma^0$  acquired over permanent water bodies as for a per-pixel estimation the number of flood events and flood pixels was too low.

The obtained performance measures indicate both high reliability and confidence although there was a slight underestimation of the flood extent, which may in part be attributed to topographically induced radar shadows along the edges of the floodplain. Furthermore, flood probability was underestimated along the shorelines of the flooded areas, most likely due to the occurrence of mixed pixels as well as topographically induced radar shadows along the edges of the inundated area. The results also highlight the importance of local incidence angle for the separability between flooded and non-flooded areas as specular reflection properties of open water surfaces increase with a more oblique viewing geometry. In this case, in contrast to the previous chapter, the decision boundary for deciding if a pixel was flooded or not has been determined separately for each pixel rather than for the whole study area. This means that the threshold optimisation is independent of the relative size of the

flooded area with respect to the image size. Furthermore, no topography-based masking had to be carried out in this case.

#### 1.6.4 Author contributions

The publications were written in collaboration with different co-authors. In detail, the contributions of the author of this thesis as lead author to the publications were as following:

- **Mapping wetlands in Zambia using seasonal backscatter signatures derived from ENVISAT ASAR time series.** Design of the study; collection and processing of SAR data; collection and processing of ancillary data (with the exception of radar altimetry data); analysis of SAR, ERA-Interim, water stage and NDVI time series; writing of the final article.
- **Flood detection from multi-temporal SAR data using harmonic analysis and change detection.** Design of the study; collection and processing of SAR data; time series analysis; flood mapping; validation; writing of the final article.
- **Probabilistic mapping of flood-induced backscatter changes in SAR time series.** Design of the study; collection and processing of SAR data; time series analysis; flood mapping; validation; writing of the final article.

## Chapter 2

# Mapping wetlands in Zambia using seasonal backscatter signatures derived from ENVISAT ASAR time series

*This chapter is an edited version of: Schlaffer, S., Chini, M., Dettmering, D., Wagner, W. (2016) Mapping Wetlands in Zambia Using Seasonal Backscatter Signatures Derived from ENVISAT ASAR Time Series. Remote Sensing, 8(5): 402. For the original see <http://dx.doi.org/10.3390/rs8050402>. The article is an open access article distributed under the terms and conditions of the Creative Commons Attribution (CC-BY) license<sup>1</sup>.*

### 2.1 Introduction

Wetlands are of significant importance for hydrological and ecological processes. They constitute vital habitats for specialised flora and fauna and contribute to the livelihoods of the local human population. Within the hydrological cycle, they behave as water storage, thereby alleviating extreme events like floods and droughts. They also play a vital role in biogeochemical cycles, acting both as sources and sinks of carbon and nitrogen emissions. However, wetlands are vulnerable to threats like climate change, land-use conversion—

---

<sup>1</sup><http://creativecommons.org/licenses/by/4.0/>

mainly to agricultural areas—and construction of reservoirs (Junk et al., 2012). Recent studies have reported a decrease of about 40% in the area covered by wetlands at the global level, albeit strongly varying between regions (Ramsar, 2015). In Sub-Saharan Africa, wetlands cover ca. 9% of the landmass. Since the second half of the 20th century, wetlands there have come under increasing pressure due to the construction of dams for the production of hydroelectricity. The function of the Zambezi River Delta as a natural ecosystem, for example, has been heavily altered after the construction of the Kariba and Cahora Bassa Dams (Mitchell, 2012). In other cases, efforts have been made to restore environmental flows by adapting dam operations. For example, the Kafue Flats in Zambia are now largely dependent on the operation of dams for annual flooding during the wet season (Schelle and Pittock, 2005). Due to the high vulnerability of wetlands to the aforementioned factors there is a strong need for monitoring their current state and projecting future trends (Ramsar, 2015).

In many regions of the world, wetlands can only be monitored using earth observation technology, either due to their remoteness or their vast size. In general, both optical and microwave sensors are suitable for this purpose, each with their own advantages and disadvantages (Ozesmi and Bauer, 2002). For global monitoring purposes, multi-sensor fusion techniques have yielded reliable results, like in the case of the Global Inundation Extent from Multi-Satellites (GIEMS) product providing monthly surface inundation extent at a spatial resolution of ca.  $25 \times 25 \text{ km}^2$  based on data from passive and active microwave as well as optical sensors (Prigent et al., 2007). For more detailed regional and local assessments, Synthetic Aperture Radars (SAR) are an appropriate source of information: they are largely unaffected by cloud cover, offer a moderate to high spatial resolution and are very sensitive to the presence of surface water and—under certain circumstances—even to water underneath vegetation (Klemas, 2013). Since wetlands are often formed as a complex mosaic of different vegetation types and hydraulic conditions a variety of scattering mechanisms can contribute to the signal measured by the sensor. In combination with different sensor configurations in terms of frequency, polarisation and observation geometry this often leads to very diverse backscatter signatures in wetlands. In the most straightforward case, calm open water surfaces act as specular reflectors, which cause water bodies to be represented as dark objects in SAR imagery. Wind and heavy rainfall, on the other hand, often roughen the water surface and complicate the retrieval (Bartsch et al., 2012). If flooding occurs below vegetation, the signal is reflected between the water surface and the trunks and stems of vegetation emerging from the water surface. This so-called “double-bounce” scattering usually results in very

high values of the backscatter coefficient  $\sigma^0$ . Nevertheless, depending on the density and structure of the vegetation, the energy can be attenuated by the canopy to a substantial degree, especially at higher incidence angles. Apart from vegetation structure and density, this attenuation mostly depends on polarisation, frequency and local incidence angle (Schumann and Moller, 2015). Compared to vertically polarised waves, horizontally polarised waves interact less with vertical vegetation structures and are therefore considered better suited for the purpose of mapping flooded vegetation (Henderson and Lewis, 2008). Moreover, the use of smaller local incidence angles reduces the distance incident radiation has to travel through the canopy, in general leading to a higher amount of energy received by the sensor (Lang et al., 2008). Attenuation by the vegetation also decreases with longer wavelengths like L-band (Schumann and Moller, 2015), which is why a considerable number of studies has been carried out using data acquired at that wavelength (e.g. Aires et al., 2013; Hess et al., 2003; Kim et al., 2014; Yuan et al., 2015; Zhang et al., 2016). It should be noted that we consider only techniques for single-polarised data here although, more recently, specialised algorithms for wetland detection from polarimetric SAR data have become available (e.g. Morandeira et al., 2016; Schmitt and Brisco, 2013; White et al., 2015).

A prominent example of the application of L-band SAR data for wetland mapping is the exercise undertaken by Hess et al. (2003) who discriminated different sparsely and densely vegetated wetland types in a large part of the central Amazon basin using mosaics of scenes acquired by the Japan Earth Resource Satellite (JERS-1) during low and high water stages. They concluded that 17% of the study area of 1.77 million km<sup>2</sup> were covered by one of the mapped wetland types. The study also highlighted the importance of seasonality in wetland water stage as it influences which of the aforementioned scattering mechanisms—specular reflection, volume scattering or double-bounce scattering—is dominant. At low water stages, stems may be protruding through the surface while they may be completely submerged during the flood peak. Yuan et al. (2015) used multi-temporal SAR acquisitions and water heights estimated from radar altimeter data to infer sensitivity of L-band backscatter towards changes in flood water level. The increase in  $\sigma^0$  with rising water level was significantly lower in areas which were characterised by a high amount of woody vegetation.

Despite the fact that L-band data are seen as the most suited wavelength for studies related to surface water and wetlands encouraging results have also been obtained using C-band data (Bartsch et al., 2009; Kasischke et al., 2003; Kuenzer et al., 2013a; Reschke et al., 2012) especially where herbaceous

vegetation is dominant (Henderson and Lewis, 2008), or even using X-band interferometric SAR (InSAR) in the case of flooded vineyards (Pulvirenti et al., 2016). For example, in a study on coastal wetlands, L-band, HH-polarised data was found to be best suited for monitoring water levels using InSAR techniques but good results could also be obtained using C-band depending on the growth stage of the vegetation (Zhang et al., 2016). Kasischke et al. (2003) reported an evident decrease of C-band backscatter with increasing water levels at sites with low to moderate vegetation cover such as prairie and woodland whereas in non-flooded areas there was a positive correlation with *in-situ* soil moisture.

Past studies have also suggested that information aggregated from multi-temporal data can help to compensate some of the shortcomings of C-band data for wetland mapping as observations are made at different stages of water level and vegetation growth. Indicators extracted from multi-temporal ENVISAT Advanced SAR (ASAR) data were used by Reschke et al. (2012) to map peatlands and maximum inundation extent over Northern Eurasia. In this case, statistical estimates of high and low backscatter for the spring and summer seasons were used as inputs to a decision tree classifier. Areas with high maximum backscatter were assumed to be associated with saturated soil. On the other hand, the maximum annual inundation extent, which is typically reached after snowmelt in spring, could be related to the lower quantiles of the per-pixel backscatter time series. For mapping permanent open water, Santoro and Wegmüller (2014) extracted statistics from ASAR time series and applied threshold classifiers to extract permanent water masks. High accuracy values could be achieved for pure pixels using minimum backscatter and variance over time as indicators. However, minimum backscatter was not robust to confounding factors such as temporary flooding and wet snow so that a low percentile of the time series histograms was used instead. When applying the approach at the global scale, a simple two-metric approach was found to be problematic, e.g. in regions where strong seasonal variations in surface water extent occurred (Santoro et al., 2015).

The approaches by Reschke et al. (2012) and Santoro and Wegmüller (2014) have in common that they rely on seasonal or global time series statistics to estimate the backscatter signatures for each pixel of a multi-temporal image stack without explicitly accounting for periodic cycles in  $\sigma^0$  induced by dynamic environmental variables like soil moisture, vegetation density and inundation extent. More objective methodologies to explicitly characterise seasonality in satellite-derived time series have been explored mainly in the field of optical remote sensing, typically in order to derive land surface phenology from parameters such as the Normalised Vegetation Difference Index

(NDVI) (e.g. Brooks et al., 2012; Eastman et al., 2009; Jonsson and Eklundh, 2002). Recently, Schlaffer et al. (2015) applied harmonic analysis to detect flood events in multi-temporal ASAR time series as deviations from backscattering behavior under non-flooded conditions. In this context, a 3rd-order harmonic model efficiently reproduced the seasonal patterns encountered in the backscatter time series from non-flooded land surfaces. Such an approach should also be suitable for modelling seasonal backscatter patterns caused by vegetation, soil moisture and inundation dynamics in a wetland, especially if a strong seasonality in the climatic forcing is present. One of the advantages of a harmonic model is that the majority of the annual variability in a time series can be explained by only a few terms (Brooks et al., 2012) and therefore it should be more suitable than using descriptive statistics for characterising seasonality.

The goal of the presented study is to assess the potential of harmonic analysis for reproducing ASAR backscatter seasonality in a tropical wetland. For this purpose, ASAR time series are compared to water heights derived from radar altimeter and soil moisture output from a land-surface model. Then, the suitability of the derived time series parameters for discriminating between different wetland types such as permanent water, seasonally flooded areas and inundated vegetation is investigated using cluster analysis. The paper is structured as follows: in Section 2.2, the study area, the available data and the methodology used for data analysis and wetland mapping are described. The suitability of the area of interest as a test bed for this assessment is justified. The obtained results are reported and discussed in Section 2.3. Finally, Section 2.4 concludes the study.

## 2.2 Material and Methods

### 2.2.1 Study Area

The Kafue River basin is located in Northern Zambia and covers an area of ca. 155,000 km<sup>2</sup> (Figure 2.1(a)). Three large wetlands are located within the basin: the Lukanga Swamps and the Kafue Flats in Zambia's Central Province and the Busanga Swamps in Northwestern Province (Figure 2.1(c)). All three of them are listed as wetlands of international importance by the Ramsar Organisation Ramsar (2017). Elevation of the study area ranges between ca. 1000 m and 1300 m whereas downstream of the Kafue Flats terrain height drops significantly (Figure 2.1(b)). Annual rainfall decreases from 1400 mm in the Northern part of the basin, where most of the runoff of the Kafue River

is produced, to ca. 800 mm in the south. The climate is characterised by a pronounced rainy season which lasts approximately from October to April (Figure 2.2). October is, therefore, regarded as the start of the hydrological year in the region (Ellenbroek, 1987).

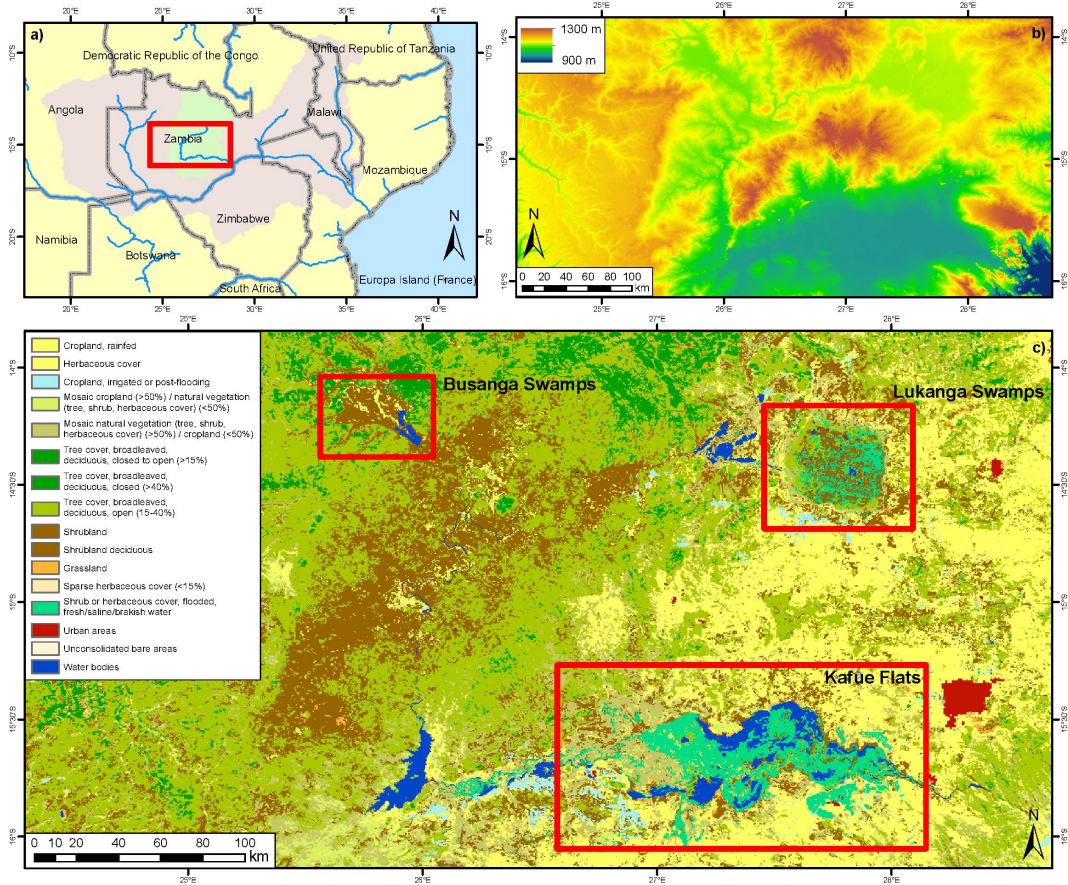


Figure 2.1: (a) Location of the study area within the Zambezi (violet) and the Kafue River (green) basins; (b) digital elevation model of the study area, source: Shuttle Radar Topography Mission (Jarvis et al., 2008); (c) land cover, © ESA Climate Change Initiative—Land Cover project 2014, version 1.4 (Bon-tempes et al., 2015).

The long, persistent flooding of the wetlands along with the diverse mosaic of vegetation and open water make the area an interesting test bed for this study. While sparsely vegetated wetland soil should have a strong radar return due to elevated soil moisture levels, denser vegetation can be expected to show intermediate backscatter coefficients due to attenuation by the canopy. During flooding, signatures should become more distinct as specular reflection from open water surfaces leads to low  $\sigma^0$  values while in flooded vegetation, double-bounce effects between the water surface and emerging vegetation parts lead

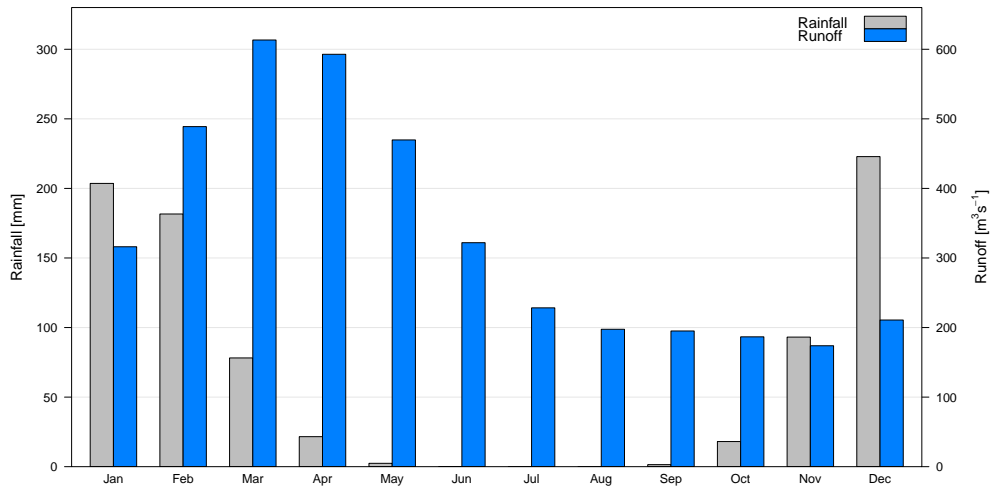


Figure 2.2: Mean monthly rainfall from WorldClim (Hijmans et al., 2005) for the Kafue River basin and mean monthly runoff at Itezhi-Tezhi for the period 1978–1991 (source: GRDC).

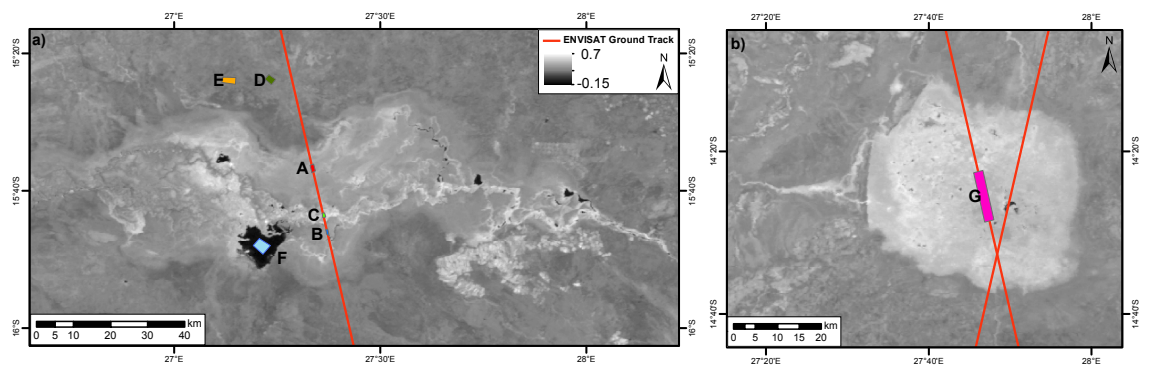


Figure 2.3: Mean Aqua MODIS NDVI with 250 m resolution (MYD13Q1) for September in the (a) Kafue Flats and (b) Lukanga Swamps along with location of AOIs. Red lines show ENVISAT altimeter tracks.

to bright areas in the resulting SAR images.

## 2.2.2 Datasets and Pre-Processing

### ENVISAT ASAR Wide Swath

Since seasonality in backscattering behaviour plays an important role in tropical wetlands, a suitable remote sensing dataset should provide sampling intervals dense enough in order to be able to capture these seasonal variations. 108 scenes acquired in C-band by the ASAR sensor on board ENVISAT were available for the Kafue Flats (Figure 2.1(c)) for the time between October 2005 to September 2007 corresponding to two hydrological years. The images were

acquired from a total number of 10 different swaths (see Figure A.1 in Supplementary Material). For the entire study region the number of scenes amounted to 227. ASAR’s Wide Swath (WS) mode offered a moderate spatial resolution of 150 m and a large swath width of 400 km leading to overlaps between adjacent swaths and therefore an overall revisit time that was lower than the satellite’s repeat cycle of 35 days. All the images that were used here were acquired in HH polarisation. Precise orbit state vectors were used to improve information about platform position (ESA, 2008). The scenes were radiometrically calibrated and terrain-corrected using the Range-Doppler algorithm (Small and Schubert, 2008) with the help of elevation data from the Shuttle Radar Topography Mission (SRTM) with a resolution of 3 arc-seconds (Jarvis et al., 2008). The images were then co-registered to a common grid definition with a pixel spacing of ca. 75 m at the Equator.

Due to the fact that the scenes were acquired using ScanSAR technology they cover a large swath width meaning that images of the same point on the ground have been acquired from different sensor positions leading to differences in viewing geometry. Local incidence angle  $\theta$  has an important influence on  $\sigma^0$  which is often corrected for using the linear relationship

$$\sigma^0(\theta_{\text{ref}}) = \sigma^0(\theta) - \beta(\theta - \theta_{\text{ref}}) \quad (2.1)$$

where  $\theta_{\text{ref}}$  is a reference local incidence angle (usually  $30^\circ$  to  $40^\circ$ ) and  $\beta = d\sigma^0/d\theta$  (e.g. Pathe et al., 2009; Wagner et al., 1999b). However, a central assumption to a time-invariant linear dependency is that the residual variance in  $\sigma^0$  is caused mainly by variations in soil moisture (Pathe et al., 2009). This implies that no major change in scattering mechanism should take place during the observation period as this would affect the sensitivity of  $\sigma^0$  towards changes in  $\theta$ . For example, it has been reported that  $\beta$  is substantially steeper over open water than over land surfaces (O’Grady et al., 2014). In a wetland, however, the assumption of  $\beta$  being time-invariant would not hold if a target area is flooded during substantial periods of the year so that the dominant scattering mechanism may change from bare-soil or volume scattering to specular reflection or double-bounce scattering and back. Seasonal variations in  $\beta$  caused by seasonality in vegetation coverage have been reported, e.g. for Southern Italy (Van doninck et al., 2014). For this reason, we chose to carry out the analysis separately for different ranges of  $\theta$ . Figure A.1 in Supplementary Material shows  $\theta$  averaged over the Kafue Flats (Figure 2.1(c)) for each scene. While it would have been preferable to analyse the data separately for each track the number of images available for each track would have

been rather low. Therefore, the images were separated into different classes based on  $\theta$  averaged over the Kafue Flats:  $15^\circ < \theta \leq 25^\circ$ ,  $25^\circ < \theta \leq 35^\circ$  and  $35^\circ < \theta \leq 45^\circ$ . The resulting average sampling interval in each of the  $\theta$  classes was between 10 and 17 days. The sampling should therefore be dense enough to represent the underlying seasonality in the backscatter time series induced by rainfall and runoff.

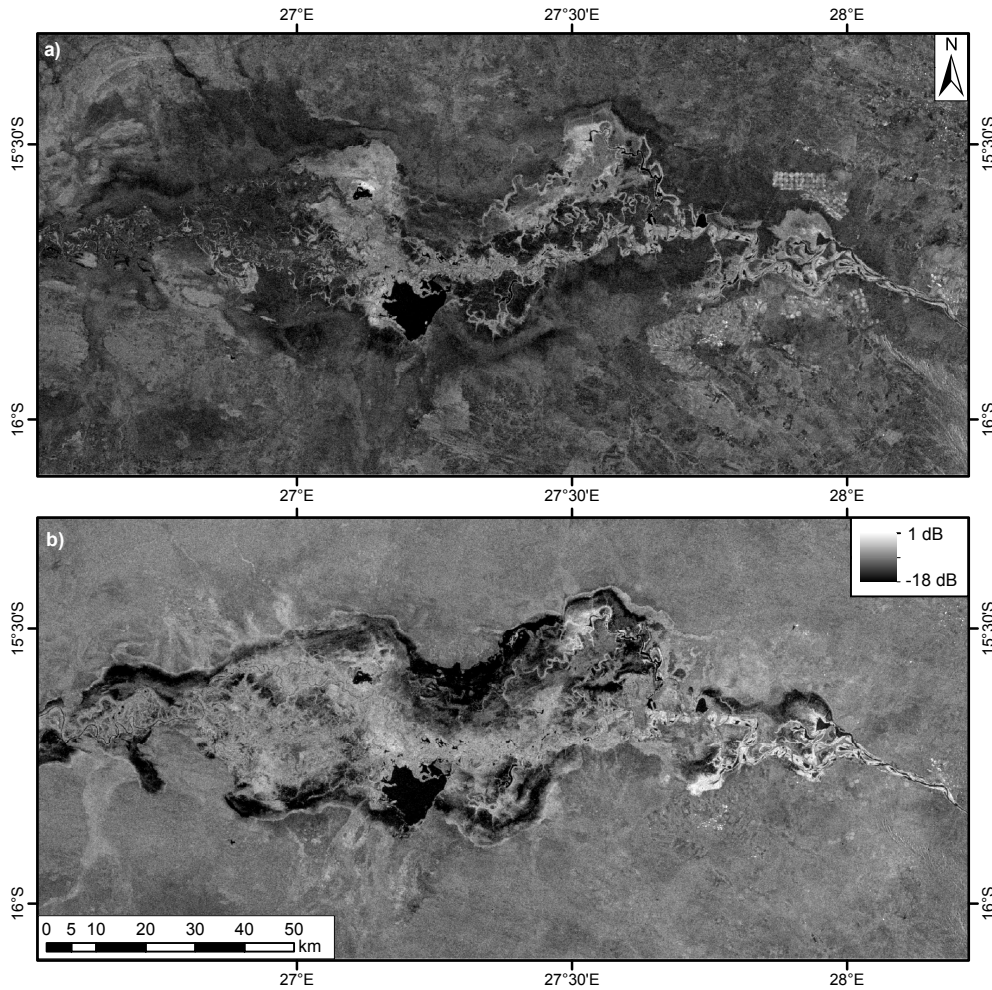


Figure 2.4: ENVISAT ASAR Wide Swath scenes acquired on (a) 10 November 2006 (dry season) and (b) 30 March 2007 (wet season).

Figure 2.4 shows examples of pre-processed scenes acquired over the Kafue Flats along the same track at the end of the dry season and approximately at the time of peak flood extent, respectively. During the dry season, a few water bodies can be seen while in general the contrast between water and land is low. In March, however, large parts of the wetland are clearly recognisable as being flooded based on the very low  $\sigma^0$  values encountered mainly along the borders of the Kafue Flats. Furthermore, the contrast between the wetland

and its surroundings is enhanced due to high soil moisture values.

### ENVISAT Radar Altimeter Water Heights

In order to investigate the relationship between SAR backscatter and water level as reported by e.g. Kasischke et al. (2003) information on water stage is necessary. In many cases, however, water level measurements from *in-situ* gauges are sparse, especially in remote areas. In the case of the Kafue Flats, runoff measured at the outlet of the Itezhi-Tezhi Dam is available from GRDC only until 1991 and was therefore not suitable for direct comparison with ASAR  $\sigma^0$ . Alternatively, satellite-based radar altimeters can provide high-accuracy water levels of inland water bodies such as lakes and rivers (e.g. Crétaux et al., 2011; Michailovsky et al., 2012). Altimeter data have also been used to infer wetland water heights and to relate their variations to changes in SAR backscatter intensity (e.g. Lee et al., 2015; Zhang et al., 2016). Although the altimeter footprint can measure up to several kilometers, the signal is highly sensitive to the occurrence of water within the footprint (Birkett, 2000). However, since satellite altimetry was designed for ocean applications, dedicated data processing for inland water is mandatory in order to extract reliable and highly accurate water levels from the observed radar returns.

The RA-2 radar altimeter on board ENVISAT provided accurate water level heights between 2002 and 2010. ENVISAT's pass 85 crossed the Kafue Flats every 35 days along the same ground track (Figure 2.3(a)). The sampling rate of the altimeter was 18 Hz leading to an along-track sampling distance of ca. 374 m. Radar echoes (so-called waveforms) were extracted from the Sensor Geophysical Data Records and processed according to the methodology described by Schwatke et al. (2015). The approach is based on retracked waveforms and rigorous outlier detection and applies Kalman filtering to produce consistent and highly accurate water heights from data acquired along different tracks. The approach provides normal heights with respect to the EIGEN-6c3stat geoid (Förste et al., 2012). Moreover, a time series for the Lukanga Swamps was computed based on data from ENVISAT tracks 543 and 156 (Figure 2.3(b)). The latter time series and its formal errors are freely available from the Database for Hydrological Time Series of Inland Waters (DAHITI) via <http://www.dahiti.tum.de> (Schwatke et al., 2015).

### ERA-Interim/Land Volumetric Soil Water

Information on soil moisture dynamics in the study area are necessary in order to characterise the climatically induced seasonality in the backscatter signal.

However, as there are no data from *in-situ* monitoring networks available and products from both passive and active microwave sensors are affected by the prolonged and extensive floods data from the ERA-Interim/Land reanalysis were used. The ERA-Interim/Land variables are produced at the European Centre for Medium-range Weather Forecasts (ECMWF) by forcing the HTESSEL land-surface model with ERA-Interim reanalysis fields (Balsamo et al., 2015). The resulting volumetric soil water fields share the native resolution of the HTESSEL model of ca.  $75 \times 75 \text{ km}^2$  but versions downscaled to up to  $0.125^\circ$  are available on the website of ECMWF. Due to the low resolution of this product it does not represent the true soil moisture dynamics in the Kafue Flats but in this context it is used to get information about the likely start and end of the wet season.

### 2.2.3 Data Analysis

The ASAR  $\sigma^0$  time series analysis was carried out in three steps: first, time series were extracted for a number of small areas of interest (AOIs). In the second step, a per-pixel analysis was carried out. Then, different wetland backscattering classes were derived from the time series based on their characteristic signatures using unsupervised classification.

#### Extraction of Time Series

Visual interpretation of  $\sigma^0$  time series is often made difficult by the occurrence of speckle which is a characteristic feature of SAR data. The influence of speckle can be decreased by averaging samples over homogeneous areas (Ulaby et al., 1986). Therefore, averaged time series were extracted from seven AOIs pertaining to different land-cover units located within and outside the Kafue Flats and Lukanga Swamps (Table 2.1). Their locations are shown in Figure 2.3. AOIs *A–C* and *G* are located below ENVISAT ground tracks so that the extracted  $\sigma^0$  time series could be compared to water height. In addition, one AOI was selected over the Chunga Lagoon (*F*) and two further AOIs in non-wetland areas north of the Kafue Flats (*D* and *E*). It can be seen that they differ considerably in terms of size and vegetation as estimated by NDVI. Due to the fact that there is much small-scale variability present within the Kafue Flats no larger AOIs with presumably homogeneous backscattering behaviour could be delineated in cases *A–C*. However, these AOIs are still large enough to minimise the speckle effect in the averaged time series. The land-cover information for AOIs *D* and *E* was extracted from the ESA Land Cover CCI

dataset (Figure 2.1(c)). AOIs *A* and *B* are located in areas which show low  $\sigma^0$  indicative of open water during the flood season and intermediate backscatter during the dry season (Figure 2.4(a)). AOI *C* is located in the vegetated floodplain close to the Kafue River where no negative change in  $\sigma^0$  due to flooding is visible (Figure 2.4(b)). AOI *G* is situated in the Lukanga Swamps (Figure 2.3(b)).

Table 2.1: Characteristics of selected AOIs.

| AOI | Land Cover           | Avg. Dry-Season NDVI (-) | Size (no. of Pixels) |
|-----|----------------------|--------------------------|----------------------|
| A   | Seasonally flooded   | 0.42                     | 371                  |
| B   | Seasonally flooded   | 0.40                     | 152                  |
| C   | Vegetated floodplain | 0.59                     | 170                  |
| D   | Tree cover, open     | 0.33                     | 755                  |
| E   | Rainfed cropland     | 0.27                     | 1098                 |
| F   | Permanent water      | -0.13                    | 1776                 |
| G   | Lukanga Swamps       | 0.50                     | 4537                 |

### Seasonality Analysis Using Harmonic Model

The Kafue Flats are subject to strongly seasonal rainfall and runoff (Figure 2.2). Radar backscatter dynamics are closely linked to hydrological processes occurring on the land surface due to the high sensitivity of microwave radiation to changes in dielectric constant. Moreover, in the case of flooding, processes such as specular reflection at open water surfaces exert a drastic influence on the energy amounts backscattered from affected surfaces. Therefore,  $\sigma^0$  time series of the region are likewise expected to display a strong seasonality. It can also be assumed that the series will not show a single annual cycle but a more complex pattern produced at multiple frequencies due to the overlaying effects of different scattering mechanisms.

The seasonal patterns of wetting, flooding and drying of the land surface within and around the Kafue Flats were analysed using harmonic modelling of the ASAR  $\sigma^0$  image time series obtained using the pre-processing workflow described in Section 2.2.2. Seasonality in remotely sensed time series has been analyzed before using similar approaches, mostly in order to derive land surface phenology based on NDVI (e.g. Brooks et al., 2012; Verbesselt et al., 2010) but rarely for SAR-derived time series. A requirement for the application of a harmonic model is that valid data points have to be present at key points of the curve (Brooks et al., 2012). This in turn requires a sufficiently dense

series which was generated as described earlier. The applied methodology is described in greater detail by Schlaffer et al. (2015). The  $\sigma^0$  time series were averaged over slices of ten days in order to regularise the sampling intervals.

A harmonic model represents a time series as a combination of  $k \in \mathbb{N}$  sinusoids, each with an amplitude  $A$  and a phase angle  $\phi$ .  $\phi$  can be interpreted as the time of the maximum of the respective sinusoid (Wilks, 2011). A backscatter time series can therefore be expressed as

$$\sigma^0(t) = \overline{\sigma^0} + \sum_{i=1}^k \left[ A_i \cos \left( \frac{2\pi i t}{n} - \phi_i \right) \right] + \varepsilon(t) \quad (2.2)$$

where  $\overline{\sigma^0}$  is the backscatter coefficient averaged over time  $t$ ,  $n$  is the number of measurements and  $\varepsilon$  a residual term. The  $k$  sinusoids represent cycles occurring with a frequency  $f_i = 1, 2, 3, \dots, k \text{ yr}^{-1}$ . The choice of an appropriate value for  $k$  was determined by the motive to reproduce the seasonality caused by the underlying climatic and flooding processes. According to our prior considerations that water level can have positive or negative effects on radar backscatter depending on the occurrence of flooded vegetation or open water, respectively, we expect that some of the affected time series will display strongly asymmetric shapes. Such deviations from a purely sinusoidal shape with a frequency  $f_i$  can be represented by overlaying a second sinusoid with a frequency  $f_{i+1} = 2f_i$  (Bloomfield, 2000). We therefore chose to represent the series by a number of  $k = 3$  sinusoids. The number of harmonic terms is limited by the Nyquist frequency which is half of the sampling rate of a signal. In the present case, the lowest number of samples is 25 over the two-year study period for  $\theta$  between  $15^\circ$  and  $25^\circ$  (see Figure A.1). The maximum possible value of  $k$  is therefore  $25/4 \approx 6$  which is twice as high as the selected value.

The parameters of the sinusoids were estimated using least-squares optimisation as missing values occurred in the time series due to the user-request-driven acquisition policy for ASAR WS data. Using the transformations

$$A_i = \sqrt{c_i^2 + s_i^2} \quad (2.3)$$

and

$$\phi_i = \tan^{-1} \left( \frac{s_i}{c_i} \right) \quad (2.4)$$

equation (2.2) can be rewritten as

$$\sigma^0(t) = \overline{\sigma^0} + \sum_{i=1}^k \left[ c_i \cos \left( \frac{2\pi i t}{n} \right) + s_i \sin \left( \frac{2\pi i t}{n} \right) \right] + \varepsilon(t) \quad (2.5)$$

which was treated like a multiple linear regression with predictors  $\cos(2\pi it/n)$  and  $\sin(2\pi it/n)$  (Schlaffer et al., 2015).

We first estimated the parameters  $\overline{\sigma^0}$ ,  $c_i$  and  $s_i$  for time series averaged from samples taken from the homogeneous areas selected as described in Section 2.2.3 to demonstrate the seasonality encountered in the area of interest. Then, the harmonic model was derived for each point  $X$  in space in the multi-temporal image stack created during pre-processing (*cf.* Section 2.2.2), which means that the harmonic model parameters can be visualised as raster maps with the same spatial dimensions as the input data.

### Regional Wetland Mapping

After the harmonic model parameters were estimated as described in Section 2.2.3 we tested whether the parameters contained enough information to classify different wetland classes such as permanent and seasonal open water. If the harmonic model is fitted to the  $\sigma^0$  time series of each pixel of a multi-temporal image stack the parameters of the model, namely mean backscatter,  $c_i$  and  $s_i$ , are available as spatially distributed variables. Therefore, using a harmonic model, a large portion of the variability in a time series can be expressed through a combination of  $2k + 1$  parameters. These variables can then be used to compare the seasonal behaviour of different pixels against each other. When no prior information about the seasonality of different wetland classes is available cluster analysis represents an efficient way to explore the relationships of the different parameters with respect to each other. Moreover, as the cosine and sine functions in equation 2.5 are approximately orthogonal to each other, Euclidean distance can be used as a measure of dissimilarity between the time series (Lhermitte et al., 2008). A  $K$ -medoids partitioning approach was applied here which is outlined below. Details are given by Kaufman and Rousseeuw (1990). Due to the size of the dataset ( $> 22 \cdot 10^6$  pixels) smaller sub-samples of 20,000 pixels were drawn at random. The sub-samples were grouped around  $K$  representative objects, the so-called medoids. Subsequently, the samples not included in the initial sub-samples were assigned to the closest representative object. The use of medoids instead of centroids assigns lower weights to outliers as the sum of absolute deviations is minimised instead of the sum of squared deviations as in the widely-used  $K$ -means method. This makes the approach more robust to the occurrence of outlying observations (Kaufman and Rousseeuw, 1990). The number of target clusters was estimated by the number of land-cover classes that the CCI Land-Cover dataset reported for the study region. All clusters related to non-water or non-wetland were com-

bined into a single “Land” class. The remaining clusters were labelled using the gathered information about hydrological and backscattering behavior from the analysis of the time series from selected AOIs (Table 2.1).

In the post-processing step, the resulting map showing the aggregated and labelled clusters was regularised using a majority filter with a square kernel of  $5 \times 5$  pixels. We further made the assumption that wetlands and periodic inundation only occur in areas which are not highly elevated above the river network. Similar assumptions have been made by e.g. Fluet-Chouinard et al. (2015). This assumption was implemented by using a mask based on the Height Above Nearest Drainage (HAND) index which essentially consists of the elevation difference between a pixel of a digital elevation model and the nearest pixel that is part of the drainage network. Details of the derivation are given by Rennó et al. (2008) and Schlaffer et al. (2015) for the masking. The digital elevation model (DEM) and the flow direction rasters available at a resolution of 3 arc-seconds from the HYDROSHEDS website (Lehner et al., 2008) were used as input for the HAND algorithm.

## 2.3 Results and Discussion

### 2.3.1 Wetland Backscatter Signatures

In this section, the results of the backscatter time series analysis are described. Since one goal of the study is to discuss the backscatter signatures in context with flood dynamics, we first focus on time series sampled from the AOIs described in Section 2.2.3. Then, the derived harmonic model parameters are discussed in a spatial context.

#### Analysis of Time Series from AOIs

ASAR  $\sigma^0$  time series were sampled from AOIs at different locations along ENVISAT ground track 85 in the Kafue Flats and track 543 in the Lukanga Swamps to compare backscatter and water level dynamics. Additional AOIs were selected in a permanent water body and non-wetland areas for comparison. Seasonality was estimated for different local incidence angle classes using the harmonic model approach (Figures 2.5 and 2.6).

Figure 2.5 shows the time series of six AOIs in and around the Kafue Flats. In the lower panel, altimeter-derived water height and soil moisture from the large-scale ERA-Interim/Land reanalysis are displayed. Although reanalysis soil moisture fields cannot realistically reproduce actual soil moisture dynamics

inside the wetland they can be used to gain information about its general seasonality based on atmospheric forcing (Albergel et al., 2013). Indeed, soil moisture shows distinct wet and dry seasons as could be expected from the monthly rainfall statistics (Figure 2.2). Water height follows the soil moisture dynamics with a time shift of some months. The annual amplitude in water height along track 85 is ca. 2 m which is similar to numbers based on *in-situ* gauges reported in the literature (Zurbrügg et al., 2012).

In the top panel of Figure 2.5, the time series of a moderately vegetated AOI (*A*) with a dry-season NDVI of ca. 0.42 is shown. For all three local incidence angle classes similar seasonal  $\sigma^0$  patterns can be observed. The maximum occurs around January which roughly coincides with the peak of the rainy season (*cf.* Figure 2.2) when soil moisture is high and vegetation should be fully developed. After this maximum,  $\sigma^0$  drops within three months to levels usually considered indicative of flooding ( $< -15$  dB). Water height reaches its annual maximum around the same time. Water level then decreases while at the same time there is a gradual increase of  $\sigma^0$  to about  $-10$  dB in September. This rather fast decrease in backscatter during the second half of the wet season and the subsequent slow increase can be attributed to flooding followed by comparatively slow flood recession due to the flat terrain. The strong negative relationship between  $\sigma^0$  and water height provides additional evidence for this hypothesis. Between October and November there is again a decrease in backscatter as the dry season progresses, most likely due to lower soil moisture levels. Approximately in December,  $\sigma^0$ , water height and soil moisture start increasing again. During this time of the year, there is a positive relationship between  $\sigma^0$  and water height.

A similar pattern can be observed for another moderately vegetated AOI (*B*) in the southern part of the Kafue Flats. The main difference here is that the flooding seems to be more persistent as indicated by the more stable low backscatter between March and July. The second maximum in September is also by a few dB lower than in AOI *A*. A possible explanation for these dynamics could be lower vegetation which remains submerged longer while in the first case gradually more and more vegetation emerges from the water surface when the flooding slowly recedes and contributes to higher backscatter. However, this cannot be fully answered given the available data as NDVI is very similar among the two AOIs and it is also does not provide an indication of vegetation height.

Very different dynamics are found for the third AOI (*C*) which is located closer to the river and more densely vegetated than the first two AOIs (NDVI = 0.59). Here, an overall positive relationship between  $\sigma^0$  and water height (irrespective

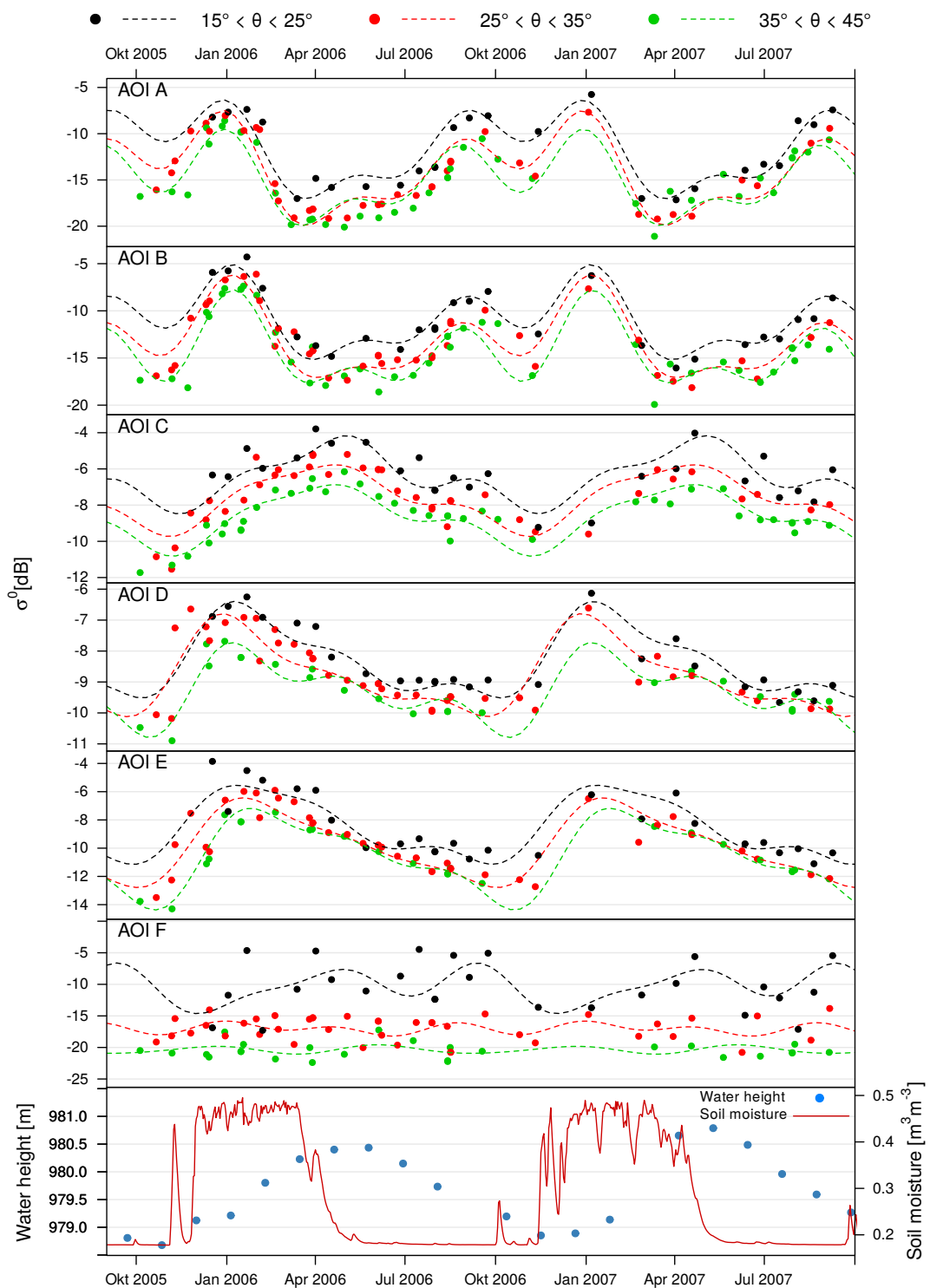


Figure 2.5: ASAR  $\sigma^0$  time series for different local incidence angle ranges in AOIs A–F as well as soil moisture from ERA-Interim/Land and altimeter water heights in the Kafue Flats (bottom). Dashed lines show fitted harmonic models.

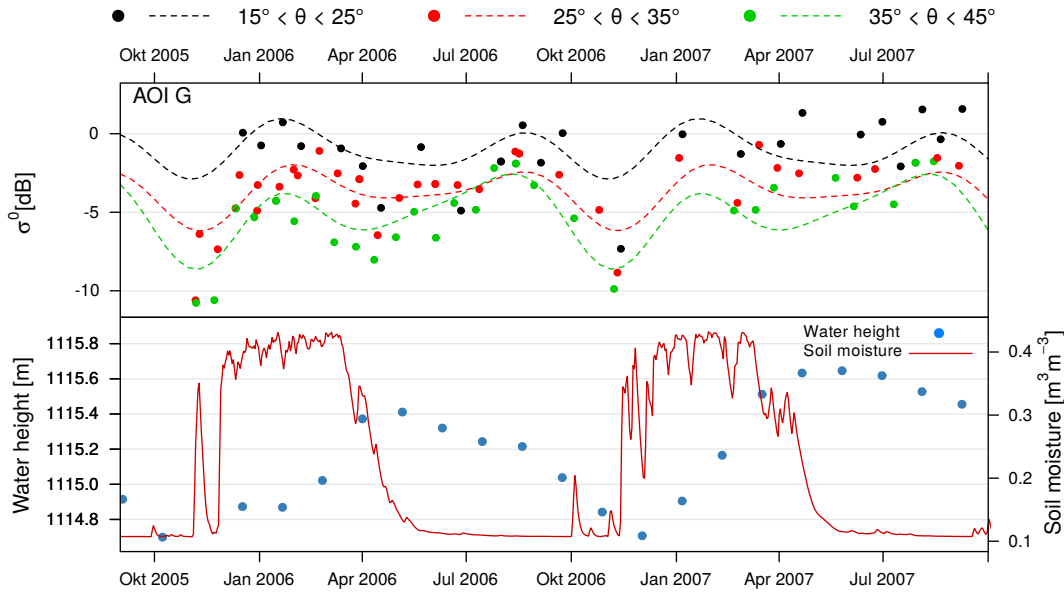


Figure 2.6: ASAR  $\sigma^0$  time series for different local incidence angle ranges in AOI G (top) as well as soil moisture from ERA-Interim/Land and altimeter water heights in the Lukanga Swamps (bottom). Dashed lines show fitted harmonic models.

of  $\theta$  class) can be noticed. Both variables increase between November and May and then decrease during the dry season. The high  $\sigma^0$  values that are reached during peak flood water height are indicative of double-bounce backscattering reaching values between  $-6$  dB and  $-4$  dB, depending on  $\theta$ . According to Ellenbroek (1987), the area along the river is characterised by tall grasses growing on levees along the river which may lead to only partial submersion during the flood season.

According to the reference land-cover dataset (Bontemps et al., 2015), the two non-wetland AOIs  $D$  and  $E$  are covered by trees and rainfed cropland, respectively. Both show similar seasonal patterns with a steep increase in  $\sigma^0$  at the onset of the rainy season and a slow gradual decline reaching a minimum around October. The main difference between the two AOIs is that AOI  $D$  has a higher annual minimum and a smaller annual variation than  $E$ , presumably due to the denser vegetation and therefore higher volume scattering during the dry season. The time series corresponding to AOI  $F$ , located over a permanent water body, shows high noise at low local incidence angles resulting in a relatively poor harmonic model fit with standard errors between 1.2 and 1.4 for the coefficients  $c_i$  and  $s_i$  while for higher  $\theta$  they lie typically around 0.5. This is most likely owed to the higher susceptibility of steep local incidence angles to water surface roughness. For the other  $\theta$  ranges, the fitted curve resembles

almost a straight line reflecting the stability of specular reflection throughout the year.

Backscatter, altimeter water height and surface soil moisture time series for the Lukanga Swamps (AOI *G*) are shown in Figure 2.6. The annual amplitude in water height was ca. 1 m, i.e. half the value found for the Kafue Flats. Backscatter throughout the year was high reflecting the high moisture content. For steep incidence angles,  $\sigma^0$  during the wet season is even  $> 0$  dB suggesting a strong double-bounce contribution from the partially submerged reed stands. It is worth mentioning that no further increase in  $\sigma^0$  is visible when water height increases above 1115 m. Rather, there seems to be a small decrease during the height of the flood season between April and June (Figure 2.6). This behaviour can possibly be explained by the decreasing length of the stems and leaves of reeds emerging above the water surface and therefore the smaller area available for the production of double-bounce scattering. Similar findings have been reported based on backscatter modelling Pulvirenti et al. (2011a). In comparison with AOI *C*, which is also characterised by seasonally flooded vegetation in the Kafue Flats, double-bounce scattering is more persistent here meaning that the vegetation is likely to be longer partially submerged in this case. According to Ellenbroek (1987), the Lukanga Swamps' main water loss is by evaporation whereas drainage towards the Kafue River is low. This offers an explanation for the sustained high backscatter values encountered in this area. In relation to the fitted harmonic models it can be noted that in the case of low incidence angles (black dashed line in Figure 2.6) the annual dynamics are probably underestimated because there is only one  $\sigma^0$  measurement available at the lowest point of the time series in November 2006.

Overall, very similar harmonic models were fitted for all three value ranges of  $\theta$ . Steep local incidence angles ( $15^\circ$ – $25^\circ$ ) are sampled with the lowest density but the strong similarity between the estimated models suggests that the sample size was high enough for the parameter optimisation. In general, time series taken at a high local incidence angle are consistently lower than those from low  $\theta$  ranges. A more detailed discussion of the differences between the estimated harmonic model parameters is given in the following paragraphs.

The differences between the harmonic models can also be illustrated in terms of the differences in the estimated coefficients  $c_i$  and  $s_i$ , corresponding to the amplitudes and phases estimated for the respective frequencies. A suitable way to visualise these differences is obtained by plotting the point pairs  $(c_i, s_i)$  for a single frequency  $f_i$  in Cartesian coordinates and to connect the points to the origin. As result, a radial plot is obtained as shown in Figure 2.7 for the seven AOIs. The length of the lines is equal to the amplitude

$A_i$  and the angle between the abscissa and the lines represents the phase angle  $\phi_i$  according to equations 2.3 and 2.4 (Lhermitte et al., 2008). For the first harmonic with an annual frequency, both AOIs with seasonal open water ( $A$  and  $B$ ) have phase angles placing their lines in the lower right quadrant of Figure 2.7(a)). Also, their lines are longer than the other AOIs reflecting the large annual amplitude of the corresponding backscatter time series (*cf.* Figure 2.5). Since no significant seasonal variations in the backscatter time series of the permanently water-covered AOI  $F$  could be identified for intermediate and high  $\theta$  (i.e.  $A_1 \approx 0$ ) only a line for steep  $\theta$  is visible which points in the almost opposite direction of the coefficients for seasonally inundated areas. This suggests a certain potential of the harmonic model parameters for being used to discriminate between permanent and seasonal water bodies even if the differences in average backscatter  $\overline{\sigma^0}$  are minor. The coefficients corresponding to AOI  $C$ , which is located close to the river, are displayed as lines in the upper left quadrant echoing the very different dynamics already shown in Figure 2.5. Moreover, the amplitude is much smaller than in the case of AOIs  $A$  and  $B$ . The coefficients related to AOIs  $D$  and  $E$ , which are not located inside the wetland areas, have similar phase angles  $\phi_1$ .  $A_1$  for the tree-covered area  $D$ , however, is smaller than for the cropland area  $E$ . AOI  $G$  which is located in the Lukanga Swamps is characterised by comparatively small  $A_1$  values for all three  $\theta$  ranges. In contrast to the other AOIs,  $\phi_1$  varies strongly between the  $\theta$  classes. This behaviour can be explained by the fact that, in Figure 2.6, two peaks can be recognised in the  $\sigma^0$  time series, the first one in January and the second one around August to September. For high local incidence angles (green dashed line in Figure 2.6), the second peak is higher than the first one which is likely to be the reason that the corresponding line is situated in the upper left quadrant of Figure 2.7(a).

In contrast, land and seasonal water bodies show a much higher similarity in terms of the parameters obtained for the second harmonic term as demonstrated by the corresponding point pairs located in the upper-right quadrant of Figure 2.7(b). Amplitudes  $A_2$  also tend to be lower than  $A_1$ .  $A_3$  estimates are of similar magnitude as  $A_2$ . Additionally, there is even less variation in  $\phi_3$  than in  $\phi_2$  between the AOIs (Figure 2.7(c)).

It is noteworthy that only minor differences in the estimated amplitudes between the different local incidence angle classes for the same AOIs can be found which is illustrated by the similarity of the solid, dashed and dotted lines in Figure 2.7. Viewing geometry expressed as  $\theta$ , however, seems to affect  $\overline{\sigma^0}$  estimates for the different AOIs (Table 2.2). In general,  $\overline{\sigma^0}$  is higher at steep  $\theta$  which is in line with our expectations. In dry-land AOIs ( $D$  and  $E$ ) as well

as in AOIs with seasonally flooded vegetation (*C* and *G*)  $\overline{\sigma^0}$  decreases in an almost linear manner with higher  $\theta$ . In case of permanent water (AOI *F*), the difference in  $\overline{\sigma^0}$  is very strong between steep to intermediate  $\theta$  values whereas between intermediate and high  $\theta$  the gradient flattens. The comparatively high  $\overline{\sigma^0}$  for low  $\theta$  is probably due to the higher sensitivity to water surface roughness at these incidence angles (Töyrä et al., 2001). In case of the AOIs with seasonal open water (*A* and *B*) the gradient seems to be marginally steeper at low  $\theta$ , however, not enough to assume a strong non-linearity. It can be concluded that, based on the data from the selected AOIs, the periodic changes between different scattering mechanisms like specular reflection and double-bounce scattering were not found to cause substantial deviations from a linear relationship between  $\sigma^0$  and  $\theta$  which is often reported in the literature (e.g. Pathe et al., 2009; Wagner et al., 1999b). Concerning the separability between wetland and dry-land classes differences between AOIs were more pronounced at higher angles.

### Spatial Analysis of Harmonic Model Coefficients

In the next step of the analysis, harmonic models were fitted separately to the time series of each pixel of the multi-temporal image stack. For each pixel, the harmonic model coefficients, mean backscatter  $\overline{\sigma^0}$ , amplitudes  $A_i$  and phases  $\phi_i$  were estimated and evaluated with respect to spatial patterns of backscatter seasonality. As it was demonstrated in Section 2.3.1 there should be a high potential to distinguish seasonal and permanent water bodies as well as regions with double-bounce backscattering using the coefficients corresponding to the first harmonic term in equation 2.2 corresponding to a frequency  $f_1 = 1 \text{ yr}^{-1}$ . The differences between AOIs were less pronounced in the coefficients corresponding to the 2nd and 3rd harmonic terms. RGB composites

Table 2.2: Estimated  $\overline{\sigma^0}$  in dB for each AOI and different ranges of  $\theta$ .

| AOI | 15° – 25° | 25° – 35° | 35° – 45° |
|-----|-----------|-----------|-----------|
| A   | −11.6     | −14.0     | −15.1     |
| B   | −10.9     | −13.1     | −14.3     |
| C   | −6.4      | −7.6      | −8.6      |
| D   | −8.3      | −8.8      | −9.3      |
| E   | −8.4      | −9.8      | −10.5     |
| F   | −10.5     | −17.0     | −20.4     |
| G   | −1.1      | −3.7      | −5.2      |

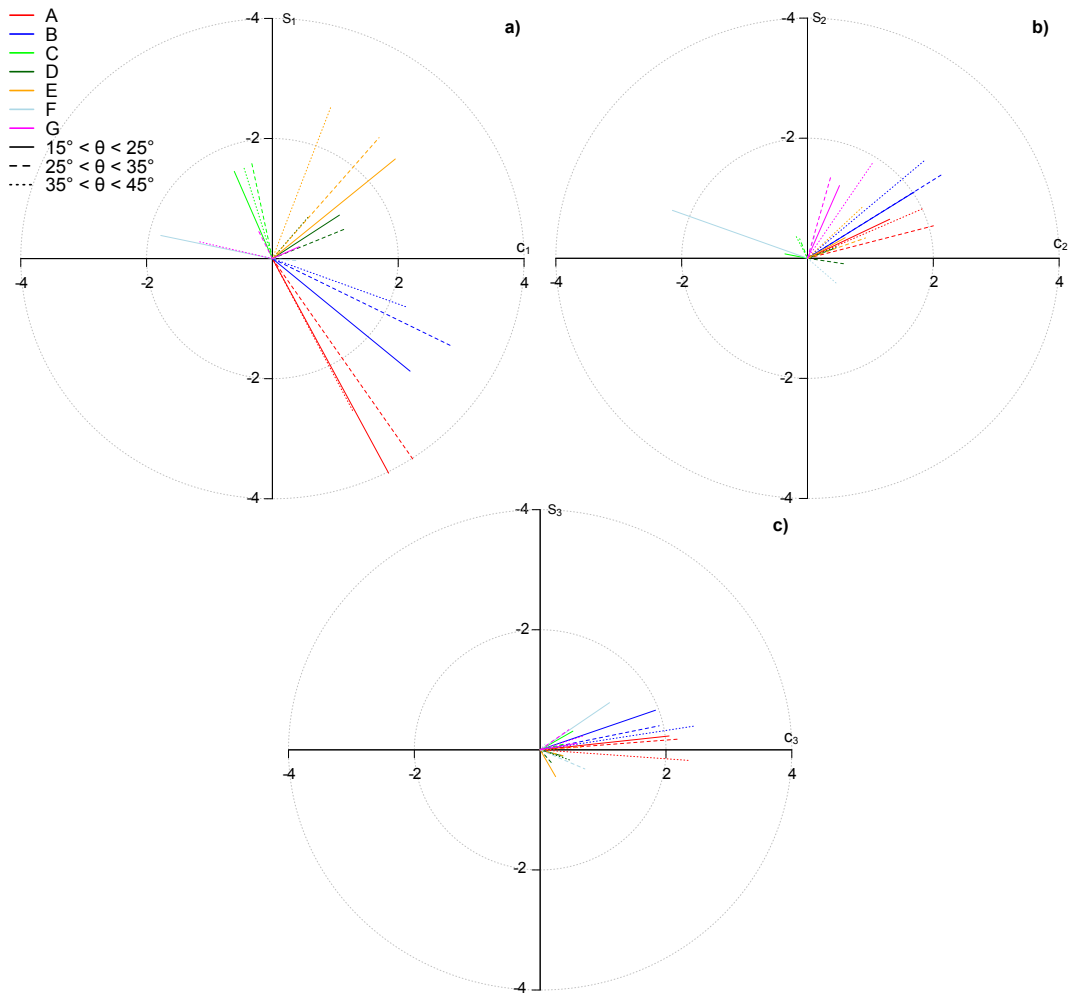


Figure 2.7: Fitted parameters  $c_i$ ,  $s_i$  of harmonic model terms (a)  $i = 1$ , (b)  $i = 2$  and (c)  $i = 3$  for the different AOIs  $A$ – $F$  and  $\theta$  ranges. Line lengths represent amplitudes (a)  $A_1$ , (b)  $A_2$  and (c)  $A_3$ ; angles between the x axis and the lines represent phase angles (a)  $\phi_1$ , (b)  $\phi_2$  and (c)  $\phi_3$ .

of  $\overline{\sigma^0}$ ,  $A_1$  and  $\phi_1$  are shown in Figure 2.8 for different  $\theta$  ranges. Phase angle  $\phi_1$  is given as Day of Year (DoY) and rescaled between 0 and 364. Visual inspection shows large differences between the wetland and surrounding areas but also within the Kafue Flats themselves. The area along the Kafue River appears as an orange-red ribbon in the centre of the maps. The time series derived from AOI  $C$  (Figure 2.5) corresponds to this backscattering class. The area is characterised by annual flooding during the wet season and high NDVI values. This leads to high average backscatter and therefore high values in the red band of Figure 2.8 while at the same time the intra-annual variability caused by flooding leads to intermediate values of  $A_1$  (green band) and low  $\phi_1$  (blue band). In stark contrast, the seasonally flooded areas north and south of

the river appear as bright blue-green bands stretching along the borders of the wetland. Comparison with the dynamics of AOI *A* and AOI *B* reveals that in these areas the maximum occurs before or during the peak of the rainy season, *i.e.*, late in the year (high DoY), after which  $\sigma^0$  is decreased due to specular reflection. This in turn leads to high values in the blue band of Figure 2.8 for seasonally flooded regions. Moreover, brighter shades of blue imply that there is also a strong green component due to a high yearly amplitude in backscatter. The high  $A_1$  and  $\phi_1$  values for seasonally flooded areas were also visible in Figure 2.7(a) for AOIs *A* and *B*. In conclusion, areas with seasonal open water are characterised by low  $\overline{\sigma^0}$  as well as high  $A_1$  and  $\phi_1$  while in seasonally flooded vegetation high  $\overline{\sigma^0}$ , low  $\phi_1$  and intermediate  $A_1$  can be found. AOIs *A* and *B* therefore correspond to areas appearing blue-green in Figure 2.8 while areas with a similar behaviour as AOI *C* appear orange to red.

In comparison, non-wetland areas are mainly shown in green and red shades. Areas shown in green should be characterised by low average  $\sigma^0$  and high  $A_1$  while for areas shown in red the opposite is true reflecting differences in vegetation density and biomass. Indeed, green areas typically have a dry-season NDVI of 0.25–0.30 while in red areas NDVI is much higher (*cf.* Figure 2.3). According to the reference land-cover dataset red areas mostly belong to tree-covered or even forested classes (*cf.* AOI *D*) while green areas fall inside cropland classes (*cf.* AOI *E*). This would partly explain the differences in  $\overline{\sigma^0}$  and  $A_1$  as in forests volume scattering can be expected to be comparatively high also during the dry season while in agricultural areas a higher sensitivity to soil moisture is usually observed. Visual inspection of the differences between Figure 2.8a–c reveals that in some areas the harmonic model coefficients are more sensitive to changes in  $\theta$  than in others. Areas that are labelled as covered by trees in the reference land-cover dataset (Figure 2.1c), for example, appear with a higher red value and therefore have higher average  $\sigma^0$  at higher local incidence angles (Figure 2.8(c) *vs.* Figure 2.8(a)). This is in line with our expectation that volume scattering is more dominant at a more oblique geometry due to the longer distance the incident radiation has to travel through the canopy.

Permanent water bodies like the Chunga Lagoon appear almost black at  $\theta > 25^\circ$  while at lower angles seasonal and permanent water is more difficult to differentiate visually based on the harmonic model components alone. Figure 2.5 shows more noise in the time series for AOI *F* acquired at  $\theta < 25^\circ$  which leads to a harmonic model which erroneously suggests a relatively high seasonality. This is likely due to the higher  $\sigma^0$  from roughened surfaces at steep incidence angles (Richards, 2009) and therefore a higher temporal variability

which can be mistaken for seasonality by the model (*cf.* Figure 2.5). At higher incidence angles, however, the harmonic model components seem to be well suited to distinguish permanent and seasonal water bodies.

The discussion here is mainly related to the parameters corresponding to the first harmonic. Additionally, gray-scale images of all the fitted coefficients are included in the Supplement to this article (Figures A.2–A.4). It can be seen that amplitudes  $A_2$  and  $A_3$  are, in general, lower than  $A_1$  and that there is much less contrast between wetland and non-wetland areas. This confirms the conclusion from section 2.3.1 that the AOIs can be distinguished mainly based on  $\overline{\sigma^0}$ ,  $A_1$  and  $\phi_1$ .

### 2.3.2 Regional Mapping of Wetland Backscattering Classes

Analysis of the harmonic model parameters in Section 2.3.1 showed that different backscattering classes in wetlands could be distinguished based on indicators of their annual dynamics and mean backscatter. We therefore chose the spatially distributed parameters  $\overline{\sigma^0}$ ,  $c_1$  and  $s_1$  as well as the standard deviation of the residual term  $s_\varepsilon$  as input parameters for the  $K$ -medoids approach described in Section 2.2.3. The cluster analysis was run over the entire region shown in Figure 2.1(c) to see if the approach was able to correctly detect the three major wetlands in the study region. Only  $\sigma^0$  measurements acquired at local incidence angles between  $25^\circ$  and  $35^\circ$  were used for the parameter estimation of the harmonic model. At these intermediate  $\theta$  values a higher contrast between permanent and seasonal water bodies as well as between forested and open areas was described in Section 2.3.1. The parameters  $\overline{\sigma^0}$ ,  $A_1$  and  $\phi_1$  are shown in form of a RGB composite in Figure A.5. The number of target clusters in the cluster analysis was 16 which is the number of land-cover classes that the ESA CCI Land-Cover dataset lists for the study region. The clusters were then combined and labelled according to a description of the seasonal behaviour of the corresponding AOIs in Table 2.3. Due to the differences in seasonal flooding that were observed between AOI *C* (Kafue Flats) and AOI *G* (Lukanga Swamps) two classes for flooded vegetation were created. “Persistently flooded vegetation” refers to persistent double-bounce scattering as observed in the Lukanga Swamps while the more dynamic behaviour along the Kafue River was regarded as typical for class “Seasonally flooded vegetation”. A suitable threshold value for masking areas in which wetlands are very unlikely to occur based on the HAND index was determined by visually assessing the distributions of HAND values for the aggregated and labelled classes using a Box-Whisker-Plot (Figure A.6 in Supplementary Mate-

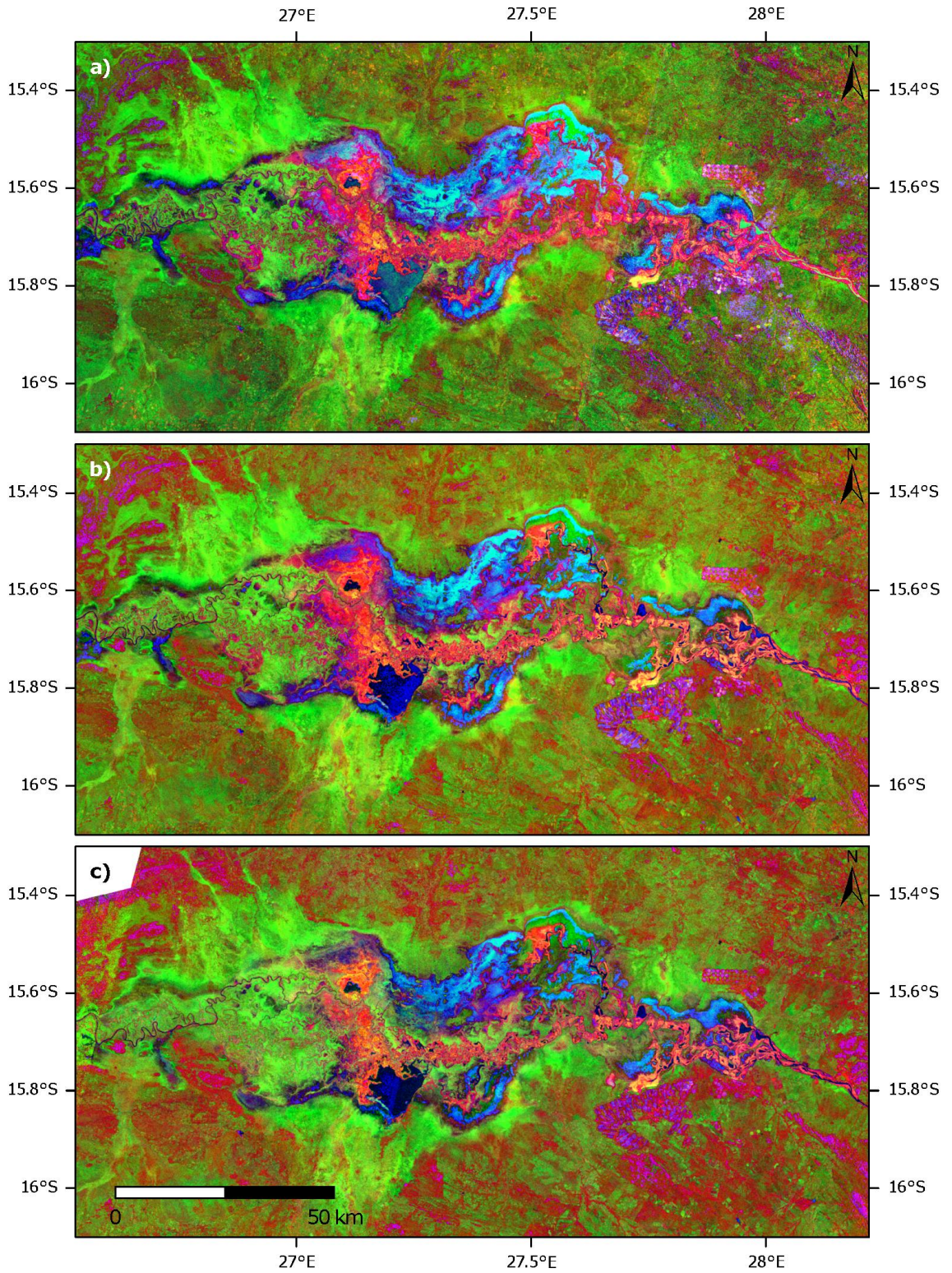


Figure 2.8: RGB composite of harmonic terms derived for (a)  $15^\circ < \theta \leq 25^\circ$ ; (b)  $25^\circ < \theta \leq 35^\circ$ ; (c)  $35^\circ < \theta \leq 45^\circ$ . Red: average backscatter; green: amplitude of first harmonic term  $A_1$ ; blue: phase of first harmonic term  $\phi_1$  given as DoY.

rial). A threshold value of 10 m effectively separated the HAND distributions of the wetland backscattering classes from the distribution conditioned on the “Land” class.

The result of the classification after applying the post-processing steps described in Section 2.2.3 is shown in Figure 2.9. A total area of almost 7800 km<sup>2</sup> was classified as one of the four wetland backscattering classes corresponding to 7.6% of the total study area. Of this area, 7% were permanent water bodies, 26% seasonal open water, 19% persistently flooded vegetation including most of the Lukanga Swamps and 22% were covered by seasonally flooded vegetation. In comparison, the CCI Land Cover dataset shows an area of 4800 km<sup>2</sup> as covered by either water bodies or flooded shrub and herbaceous vegetation. Discrepancies are mainly visible in the Lukanga and the Busanga Swamps where large portions are classified as shrubland in the CCI product. However, flooded vegetation seems to be more likely here as these areas, according to topography (*cf.* Figure 2.1(b)), are located within the aforementioned wetlands. All three major wetlands in the region, the Kafue Flats in the south, the Lukanga Swamp in the north-east and the Busanga Swamps in the north-west were detected by our approach. Also, the Itezhi-Tezhi reservoir, the Chunga Lagoon and a number of other permanent water bodies are well represented. In the Kafue Flats, the main wetland units of densely vegetated floodplain along the river and seasonal open water along their northern and southern edges are correctly identified. In contrast to the complex mosaic found in the Kafue Flats, the main part of the Lukanga Swamps is quite homogeneously covered by persistently flooded vegetation. This class is also found in the Kafue Flats in the proximity of large permanent water bodies like the Chunga Lagoon and in the flooded areas behind the Kafue Gorge Dam at the eastern end of the flats. The Busanga Swamp seems to be more vegetated in its northern part while the southern part exhibits seasonal open water bodies. The Kafue River is not continuously visible due to its rather narrow channel width of 150 m to

Table 2.3: Reclassification table.

| AOI                             | Class Labels | Clusters    |
|---------------------------------|--------------|-------------|
| Permanent water                 | 16           | <i>F</i>    |
| Seasonally flooded              | 14           | <i>A, B</i> |
| Persistently flooded vegetation | 15           | <i>G</i>    |
| Seasonally flooded vegetation   | 3            | <i>C</i>    |
| Land                            | 1, 2, 4–13   | <i>D, E</i> |

200 m (according to visual assessment using Google Earth imagery). This is below the size of the majority filter which may have reclassified pixels belonging to the river to the land class. However, since the focus of this study was the mapping of wetlands we chose not to alter the filter size of  $5 \times 5$  pixels.

The masking based on elevation difference to the nearest drainage mainly removed forested pixels in the topographically complex south-eastern part of the region which would otherwise have been falsely classified as open water or flooded vegetation due to radar shadow and layover, respectively. It should also be mentioned that larger urban areas were falsely classified as flooded vegetation due to high  $\overline{\sigma^0}$  and low annual variation. Nevertheless, the HAND-based mask successfully removed such areas as in the case of Lusaka.

## 2.4 Conclusions

In the presented study, moderate-resolution ENVISAT ASAR data acquired over a time period of ca. two years were compared to altimeter-derived water height estimates and surface soil moisture from a reanalysis dataset to assess characteristic seasonal patterns in C-band radar backscatter from tropical wetlands. It was hypothesised that different scattering mechanisms caused by soil moisture and inundation dynamics along with vegetation density affected the observed backscatter ( $\sigma^0$ ) time series. Indeed, a positive contribution of water height to the backscatter coefficient was found under dense vegetation whereas in more open areas, specular reflection dominated the signal as soon as most of the vegetation had been submerged. These differences lead to typical time series signatures, which were characterised using a harmonic model. Selected harmonic model parameters estimated for each pixel in a multi-temporal image stack were then used to classify wetland backscattering classes at the regional scale by applying an unsupervised classification approach. It was possible to clearly differentiate permanent water bodies, seasonal open water, seasonal flooded vegetation as well as persistently flooded vegetation from dry-land areas.

Furthermore, we addressed the question of whether periodic changes in scattering mechanism (volume scattering, double-bounce scattering, specular reflection) affected the seasonal signatures of the  $\sigma^0$  time series as expressed in terms of their amplitudes and phases. The effect of different local incidence angles was found to be sufficiently well described by a linear shift in average backscatter between the incidence angle bands. The only substantial exception to this finding were permanent water bodies where data acquired

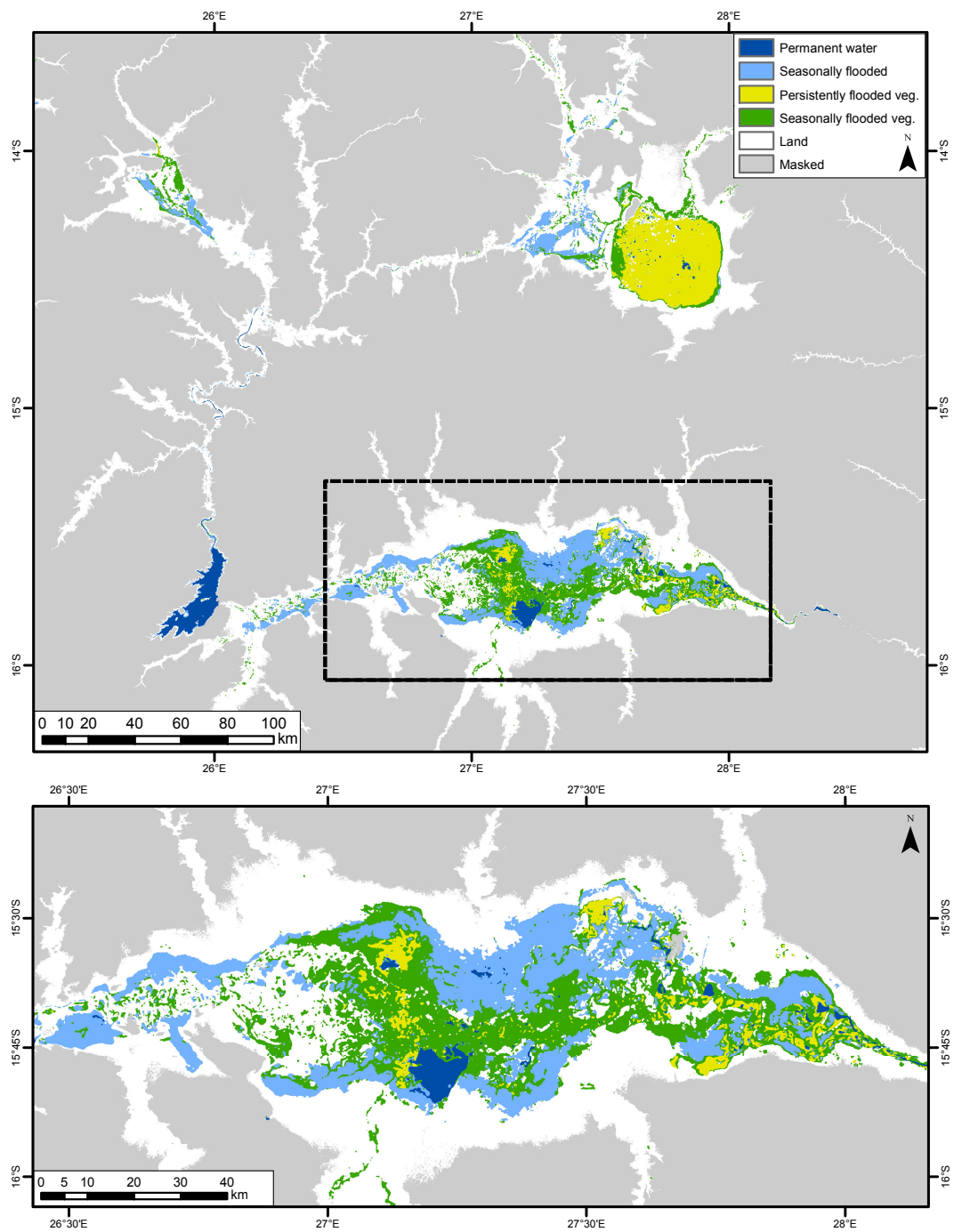


Figure 2.9: Result of wetlands classification for the entire study area (top) and the Kafue Flats (bottom).

at higher incidence angles seemed to be less affected by water surface roughness. The effect of local incidence angle  $\theta$  on  $\sigma^0$  could, therefore, be largely corrected for by using a linear normalisation approach as found in the literature on soil moisture retrieval from radar data. For the wetland classification, data acquired in a  $\theta$  range between  $25^\circ$  and  $35^\circ$  were selected as our analysis had shown that, at these intermediate incidence angles, a good trade-off was obtained between robustness to surface roughness for open water classification and canopy attenuation for the classification of vegetated wetlands.

Typically, SAR-based wetland classification methods, some of which were mentioned in Section 2.1, take into account imagery acquired during flood and dry seasons. Such approaches usually require a significant amount of intervention by the operator, especially for selecting suitable image acquisitions. In contrast, in the proposed approach, magnitude and timing of backscatter seasonality are explicitly modelled for each pixel while taking into account the full time series of ASAR images. We believe that our method makes an important contribution towards more automatic wetland classification approaches, especially as more systematic acquisitions are made possible by satellite missions such as Sentinel-1. As the application of a harmonic model requires a time series with a length of at least one seasonal cycle the proposed approach for wetlands mapping is generally suitable for detecting changes and trends in wetland extent and type from longer SAR time series. An important prerequisite is a dense enough temporal sampling. Since the conclusion of the ENVISAT mission Sentinel-1 is a prime candidate for continuing the existing time series of C-band SAR data. However, at the time this manuscript was finalised only a small number of scenes had been acquired by Sentinel-1 over the study region.



# Chapter 3

## Flood detection from multi-temporal SAR data using harmonic analysis and change detection

*This chapter is an edited version of: Schlaffer, S., Matgen, P., Hollaus, M., Wagner, W., 2015. Flood detection from multi-temporal SAR data using harmonic analysis and change detection. International Journal of Applied Earth Observation and Geoinformation, 38: 15–24. For the original see <http://dx.doi.org/10.1016/j.jag.2014.12.001>.*

### 3.1 Introduction

Floods are among the most frequent natural disasters caused by meteorological phenomena. Recent studies based on insurance data have shown that between 1980 and 2011 hydrological disasters accounted for 23% of all reported losses and 10% of fatalities that were caused by natural disasters (MunichRe, 2012). In addition to losses of lives and property, major flood events have led to internal displacement and resource shortages like in the case of the 2010 Pakistan floods where more than 14 million people were affected (World Food Programme, 2010). Flood monitoring and mapping using earth observation (EO) data can help authorities and non-governmental organisations in disaster management and coordination of humanitarian efforts. Users have described

maps showing inundation extent as being of key value in operational settings as well as for strategic planning of flood prevention and mitigation measures (Zlatanova, 2013).

Data from both optical and microwave sensors can be used for flood mapping. Synthetic Aperture Radar (SAR) systems offer the possibility to operate day and night and they are able to penetrate clouds and heavy rainfall, a feature which is of special importance considering the weather conditions under which flood events usually occur. In the past, data from moderate-resolution sensors like the Advanced SAR (ASAR) on-board ENVISAT have been extensively used while more recently, high-resolution imagery from platforms such as TerraSAR-X and Cosmo-SkyMed has become available. However, for global applications, due to the price of high-resolution imagery, free data continue to be important despite of their potentially lower resolution. After end-of-mission was declared for ENVISAT in April 2012, continuity is expected to be ensured by the Sentinel-1 constellation whose first satellite was launched in April 2014. The ASAR sensor was, like the SAR sensor on-board Sentinel-1, operated in C band with a wavelength of  $\lambda \approx 5.6$  cm. ASAR mapped European land surfaces every 3 – 6 days, depending on the acquisition mode.

Detection of water bodies from SAR data typically makes use of the unique characteristics that water exhibits in the microwave spectrum. Calm, open water surfaces act as specular reflectors and reflect incoming radiation away from the sensor, which in general results in low backscatter measurements. Different environmental factors like wind-induced waves, however, increase surface roughness while vegetation and infrastructure emerging from the water surface can produce double-bounce effects (Woodhouse, 2005). While these lead to an increase in the backscatter signal, other surface types like dry, bare sand can be confused with open water due to low backscatter. For example, O’Grady et al. (2011) report that alluvial sediment can be easily confused with flooded areas.

Due to the aforementioned advantages of SAR sensors for flood monitoring, it is not surprising that during the last decade considerable effort has been spent on developing algorithms for flood delineation from SAR imagery. In general, these algorithms can be divided into single-image analysis and change detection approaches. Some of the more traditional image-processing based approaches were compared by Schumann et al. (2009) and include visual interpretation, automatic thresholding, image texture analysis and active contouring. The authors conclude that a multi-algorithm approach is more promising than relying on a single algorithm and propose the use of ensembles yielding a “probability of inundation” map based on the ensemble classifica-

tions. However, most studies up to this day rely on a simple global threshold to be applied to the whole scene or parts of it. A suitable threshold value can either be found by visual inspection of the gray-scale histogram (Bartsch et al., 2008) or by using an automatic algorithm. One of the most widely used image thresholding techniques is Otsu's method which aims at minimising within-class variability while at the same time maximising between-class variability (Otsu, 1979). A commonly encountered problem in connection with this approach is that flooded areas usually only cover a minor portion of a SAR scene. Therefore, histograms often do not exhibit a characteristic bimodal distribution or a strong tailing indicative of an inundated area. Modifications have been proposed to make the approach more robust towards this underrepresentation of flood pixels, e.g. by splitting the scene into subsets or tiles before the histogram analysis (Martinis et al., 2009).

Most of these approaches have in common that they are mostly based on pure image analysis techniques. However, these methods have shortcomings as they largely do not take into account possible confusion between flooded and non-flooded areas in the SAR scene. Moreover, using a single SAR image, it is not possible to distinguish permanent and transient water bodies. Another category of classification algorithms involves the detection of changes in time and takes into account one or more scenes which were acquired before or after a flood event when the flooded area was dry. In its simplest form, a change image is produced by simply subtracting the grey values of a flood scene from those in a reference image and then applying a classification algorithm. Often, change detection is combined with image analysis such as automatic thresholding (Martinis et al., 2009) and region growing (Giustarini et al., 2013; Matgen et al., 2011). Change detection techniques for flood delineation from SAR data typically involve only one to very few scenes taken under non-flooded conditions.

However, a suitable reference image should fulfil a series of requirements: it should have the same viewing geometry and the same polarisation configuration as the flood image while at the same time characterising the backscatter signature of the area of interest. Furthermore, it should have been acquired during the same season as the flood image, especially in regions with a pronounced seasonality in moisture and vegetation growth, such as the humid and semi-arid tropics (Hostache et al., 2012). In combination with the often irregular coverage found with imagery from sources such as ENVISAT ASAR this can make the selection of an appropriate reference image a difficult and time-consuming task. Furthermore, an approach taking advantage of the full information from a time series containing tens or hundreds of images acquired

over an area may have additional benefits for characterising backscatter characteristics of a land surface. In an approach recently presented by Westerhoff et al. (2013), probability distributions of water and non-water backscatter are derived from multi-temporal ASAR imagery. Using these histograms, the probability of a new measurement belonging to either one or the other population can be derived. In another recent study, O'Grady et al. (2014) used the relationship between local incidence angle and backscatter coefficient  $\sigma^0$  to separate water and non-water pixels, addressing commonly encountered problems such as underdetection due to waves on water and overdetection due to low backscatter from dry surfaces. Regardless, multi-temporal image analysis of SAR data is still the exception and these techniques are mostly used for parameters derived from optical data. In optical image analysis, multi-temporal approaches are more commonly found. Verbesselt et al. (2012) proposed an algorithm applying harmonic analysis to Normalised Difference Vegetation Index (NDVI) time series to detect breakpoints caused by drought events. However, droughts are usually much longer than floods and hence easier to detect using this breakpoint method. Also, a similar approach has not yet been used for SAR-derived time series which are characterised by a higher degree of noise than NDVI products.

In this study, a novel flood delineation approach using change detection in multi-temporal SAR data is presented. For this purpose, a harmonic model is fitted to backscatter time series on a per-pixel basis and an analysis of the residuals is performed. As this study is meant to be seen as a precursor study for the upcoming Sentinel-1 mission, data from ENVISAT ASAR are used. In section 3.2, the theory and assumptions underlying the proposed method are presented along with the processing chain, the test area and the selected data. Special emphasis is given to the steps involved in data preprocessing because a specific requirement of a time-series based approach is that different scenes are registered to each other as precisely as possible. The harmonic model approach is tested for a flood event which took place in summer 2007 in the south-western United Kingdom (UK) and which has been the subject of a series of studies (Giustarini et al., 2013; Martinis et al., 2009; Mason et al., 2010; Matgen et al., 2011). In addition, we use a simple change detection involving a pre- and a post-flood SAR image to compare the proposed approach with a more traditional method. The results are described and discussed in Section 3.3. An outlook for the applicability of the proposed methodology in the context of future earth observation missions is given in Section 3.4. Finally, conclusions of the study are drawn in Section 3.5.

## 3.2 Material and Methods

In the first part of this section, the ideas underlying the proposed approach are outlined and the applied harmonic model is defined. Subsequently, there is a detailed explanation of the preprocessing and the flood delineation methodologies. Finally, the case study and the selected datasets for flood delineation and validation are described.

### 3.2.1 Harmonic analysis of SAR time series

#### Temporal patterns in SAR time series

Microwave signals interact with the earth's surface in many different ways. They can be absorbed, scattered or reflected away from a surface. Which of these mechanisms is predominant in the measurement of  $\sigma^0$  depends on imaging geometry (e.g. local incidence angle), reflectivity (e.g. dielectric properties of soil and vegetation) or surface roughness (Woodhouse, 2005). In addition, the response also varies with sensor parameters such as wavelength and incoming and outgoing polarisation (Kornelsen and Coulibaly, 2013). For a single pixel, the contributing variables can be separated into two types: factors which can be assumed to be constant in time—such as sensor-related parameters—and factors which are variable—like soil moisture and vegetation.

The  $\sigma^0$  value can therefore be expected to behave according to the surface state (dry, wet, vegetated, etc.) and to exhibit a distinct seasonality. For example, in (sub-)tropical semi-arid climates with a single rainy season the dielectric constant of the soil increases along with soil moisture from the start of the wet season onwards. Furthermore, increased soil moisture facilitates the development of a plant canopy which acts as a volume scatterer. As a result of these processes an increase in  $\sigma^0$  can be expected. During the dry season, on the other hand, soil moisture is often low and crops are harvested so less microwave energy is returned from the land surface.

In contrast to land surfaces which act more or less as scatterers, calm open water surfaces are nearly perfect specular reflectors from which only a very low amount of energy is returned to the sensor (Woodhouse, 2005). This means that  $\sigma^0$  will undergo a sudden drop when an otherwise dry land surface is flooded. The effect will only last as long as the area is submerged under water. In the following chapters, a change detection method is proposed in which the  $\sigma^0$  signature of dry land is estimated for each pixel using a commonly applied time series analysis technique. Here we use harmonic analysis whose fundamentals are outlined in the following section.

### Harmonic analysis

The aforementioned seasonality of  $\sigma^0$  can be mimicked in different ways. Given the availability of meteorological data and information about soil, land use, etc. soil moisture dynamics can be simulated using a soil water balance model.  $\sigma^0$  can then be modelled using a backscatter model such as the widely used semi-empirical model by Oh et al. (1992). However, critical parameters of these models like surface roughness are often hard to measure and meteorological and land-use information may not be readily available.

Inverse time series analysis techniques can instead be used when a large amount of multi-temporal backscatter images are available. In the presented approach, a harmonic model is fitted to time series of measurements spanning several seasonal cycles. Such a harmonic model can also include a trend component in addition to the seasonal term. The trend term usually consists of a linear or polynomial model while the seasonal component includes of a series of  $k$  sine and cosine components. In theory,  $k = n/2$  cycles are possible for a time series with a sampling frequency of  $1/n$ . However, in practice a value of  $k = 3$  has been found to be sufficient to represent processes which occur on a time scale of ca. four months (Verbesselt et al., 2012). By selecting this value of  $k$  it was ensured that individual flood events, which are usually only covered in 1–2 scenes, have minimal impact on the fit of the harmonic model.

The harmonic model formulation used in this study is similar to the one used by Verbesselt et al. (2012) for breakpoint detection in time series. However, as no overall change of  $\sigma^0$  in time was to be expected a trend term was not included. The harmonic model is defined as

$$\hat{\sigma}^0(t) = \bar{\sigma}^0 + \sum_{i=1}^k \left\{ c_i \cos\left(\frac{2\pi it}{n}\right) + s_i \sin\left(\frac{2\pi it}{n}\right) \right\}, \quad (3.1)$$

where  $\hat{\sigma}^0(t)$  is the estimated radar backscatter at time  $t$ ,  $\bar{\sigma}^0$  is the average radar backscatter, and  $c_i$  and  $s_i$  are the  $i$ -th sine and cosine coefficients, respectively. These coefficients can be approximated using standard linear regression techniques (Wilks, 2011). If the harmonic model is applied to each pixel time series in a co-registered image time series, each of the  $2k + 1$  coefficients will be available as a map.

### 3.2.2 Preprocessing

One of the key requirements of time-series-based remote sensing methods is that the scenes form an image stack in which the pixels are superposed as

accurately as possible. Any errors in collocation would introduce additional variance which would influence the subsequent calibration of the harmonic model. Furthermore, the large swath width offered by the ScanSAR technology applied in the selected ASAR acquisition mode makes it necessary to combine scenes acquired with different viewing geometries. A wide range of studies has reported on the effect of local incidence angle  $\theta$  on  $\sigma^0$  (Dellepiane and Angiati, 2012; O’Grady et al., 2013; Sabel et al., 2012). This effect has to be accounted for when using data acquired from different orbits. The data preprocessing scheme described in this section aims at producing such a co-registered time series.

After collecting the ASAR Level 1b scenes for the test case described in Section 3.2.4 the datasets were orthorectified and geocoded using the Range-Doppler approach (Cumming and Wong, 2004). The void-filled digital elevation model (DEM) from the Shuttle Radar Topography Mission (SRTM) with a resolution of ca. 90 m (Jarvis et al., 2008) was used for terrain correction. The location information of the sensor was refined using DORIS verified orbit information (ESA, 2008). After this step, the geocoded scenes had a pixel spacing of 2.3“, corresponding to ca. 75 m.

For coarse resolution data and applications for which the detection of features such as waterlines is not critical, simple bilinear resampling yields good results (Pathe et al., 2009; Sabel et al., 2012). However, for flood detection precise co-registration of images is of high importance. A two-step procedure was adopted consisting of image resampling and the actual co-registration. In the first step, the scenes were collocated to a common global grid definition using bilinear resampling. During co-registration, all images were registered to a common reference image. To produce such a reference image, the scenes were stacked and an average image was computed. Then, 200 ground control points (GCPs) were uniformly distributed across each image. For each GCP, the cross-correlation between the reference image and each ASAR scene was computed over a window with an extent of 64 pixels. Each scene was warped to the global grid using a linear warp function which was derived from the spatial shift between the GCPs and the reference pixel for which the cross-correlation was maximised. After two iterations the root mean squared spatial shift was less than 0.4 pixels for all scenes.

In order to account for the influence of  $\theta$  on the  $\sigma^0$  measurements they were normalised to a reference projected local incidence angle  $\theta_{\text{ref}} = 30^\circ$  using a linear relationship between the two variables:

$$\sigma^0(\theta_{\text{ref}}) = \sigma^0(\theta) - \beta \cdot [\theta - \theta_{\text{ref}}], \quad (3.2)$$

where  $\beta$  is the slope parameter of the linear regression between  $\sigma^0$  and  $\theta$ . This relationship was calibrated separately for each pixel. According to Pathe et al. (2009), problems using this approach may arise when using only a small number of measurements due to the fact that variations in soil moisture may affect the calibration of  $\beta$ . Hence, it was made sure that a sufficient number of ASAR scenes was available. Details of the normalisation approach are described by Pathe et al. (2009).

Another peculiarity of ASAR data is the strongly irregular sampling interval. Irregularly spaced time series are unsuitable for harmonic analysis (Wilks, 2011). Therefore, before fitting the coefficients of the harmonic model, composites were produced by averaging  $\sigma^0(30^\circ)$  over discrete 10-day slices.

### 3.2.3 Flood delineation

The harmonic model (equation 3.1) was fitted to the 10-daily time series of each pixel using the statistical software package *R* (R Core Team, 2014). This resulted in a number of  $N$  maps each of which contain  $P$  pixels showing the residuals

$$\varepsilon_{pj} = \sigma^0(\theta_{\text{ref}})_{pj} - \hat{\sigma}_{pj}^0, \quad (3.3)$$

with  $1 \leq p \leq P$  and  $1 \leq j \leq N$ .  $\hat{\sigma}_{pj}^0$  denotes the normalised backscatter estimated using the harmonic model in eq. 3.1 at point  $p$  and time step  $j$ .

For the purpose of flood delineation we are mostly interested in the size of  $\varepsilon$ . Our assumption is that if a  $\sigma^0$  measurement is significantly lower than the value that is predicted by the harmonic model it is likely that the measurement was acquired during a flood. Since  $\varepsilon$  denotes the absolute divergence from the harmonic model in units of dB for each backscatter measurement, a form of standardisation is necessary in order to facilitate comparisons between pixels and to create a map for a certain time step. The distances from the fitted line were therefore converted from an absolute to a relative measure. For each pixel, the standard deviation  $s_{\varepsilon,p}$  was computed from all  $\varepsilon_{pj}$  in the time series. The standardised residuals  $\varepsilon_{pj}^{\text{std}}$  were then derived as the ratio between  $\varepsilon_{pj}$  and  $s_{\varepsilon,p}$ .

For the final evaluation of the methodology, a binary map of flooded and dry areas has to be produced from the map of  $\varepsilon_{pj}^{\text{std}}$  for the time step of interest  $j$ . This is most commonly done by applying a threshold value. An optimal threshold value was derived using the widely used Otsu method (Otsu, 1979) which estimates a suitable threshold value from a bimodal image histogram. The Otsu method relies on the image having a bi-modal histogram for proper

separation which means that the contrast in grey values between flooded and non-flooded pixels should be as high as possible. Following the approach advocated here, the contrast is increased by masking out areas which are known *a-priori* to be very unlikely to be inundated.

For this purpose, the Height Above Nearest Drainage (HAND) index was used which is defined as the height difference between a DEM cell and the nearest cell which is part of the drainage network. The distance between the cells is measured by choosing a path determined by the flow direction in each DEM pixel (Rennó et al., 2008). The HAND index was derived from the HYDROSHEDS database which contains flow directions derived from SRTM at a resolution of 3" (Lehner et al., 2008). The stream network was derived by computing the accumulated flow for each pixel and classifying all cells as drainage cells which had a number of contributing pixels of 1000 and higher. The resulting drainage network was further thinned by only retaining segments with a Strahler stream order of at least 3. The height differences were computed from the void-filled DEM included in HYDROSHEDS. We chose a threshold height of 10 m above the drainage network to mask out areas which are not prone to flooding. While the actual flood-prone areas may lie lower this threshold value was chosen to be as conservative as possible while still increasing the contrast between flooded and dry areas in the image. In regions with a less pronounced topography a lower threshold can be chosen to attain a similar effect. A second effect of the masking is the removal of pixels that would be falsely classified as flooded due to radar shadows induced by steep topography. Such pixels usually have high HAND values and can therefore be easily masked using this approach.

In order to compare our method with a more traditional change detection approach, an image pair was created from the flood scene and a corresponding non-flood scene. A change image was computed by subtracting the non-flood and the flood image. As the resulting change image is in units of dB and the standardised residuals in units of  $s_\epsilon$  both results were scaled to fit the interval  $[0, 1]$  for better comparability. Again, the Otsu algorithm was applied to the change image to determine a threshold value after non-flood-prone areas were masked as described previously. In the following sections, the change detection approach is referred to as method *CD* and the harmonic model approach as method *HM*.

### 3.2.4 Study area and datasets

The south-western UK experienced a large-scale flood event in the second half of July 2007. Especially the area around Tewkesbury at the confluence of the Rivers Severn and Avon was affected. Between May and July of that year, England and Wales on average received 414 mm of rain while mean annual precipitation in the area is ca. 850 mm. The exceptionally high summer rainfalls of 2007 can be clearly seen in the monthly precipitation time series measured at Pershore College (Figure 3.1). Between 19 and 20 July, rainfall at this station was 157 mm, more than half of the total rainfall recorded during that month (Environment Agency, 2007). At Saxons Lode on the River Severn, a peak water level of 5.9 m was reached on 22 July (Marsh and Hannaford, 2007).

For the lower Severn and Avon Rivers, a dataset comprising  $N = 518$  scenes acquired by ENVISAT ASAR in Wide Swath (WS) mode between 2005 and 2012 is available. WWS mode offers a moderate spatial resolution of about 150 m. All imagery available for this case study is in vertical transmit-vertical receive (VV) polarisation. Although horizontal transmit–horizontal receive (HH) polarisation is generally preferable for flood mapping (Henry et al., 2003). VV-polarised data have been successfully used for flood mapping in previous studies (e.g. Matgen et al., 2011; Schumann et al., 2009). During the inundation event itself, a scene was acquired in the morning of 23 July 2007 (Figure 3.2(a)). For the *CD* method a reference image acquired during non-flood conditions is required. The reference scene (Figure 3.2(b)) was acquired on 22 August 2005 in vertical polarisation and along the same track as the flood image (track 94). The scene was selected according to the methodology proposed by Hostache et al. (2012). All scenes acquired in WS mode over the area along track 94 were considered as candidates for a non-flood scene. The selection methodology consists of deriving three indices describing the distribution of  $\sigma^0$  values. The chosen scene is characterised by relatively low spatial variability of backscatter which indicates non-flood conditions and a backscatter close to the median of all candidate acquisitions. Moreover, the image was—like the flood scene—acquired during summer and should therefore show backscattering characteristics that are similar in terms of vegetation influence. Intense rain is also known to be able to affect C-band backscatter. However, according to hourly rain gauge data from the region measured around the same time as the ASAR scenes this can be ruled out in this case. The location of the rain gauge at Pershore College is shown in Figure 3.2(b)).

The flood extent was derived using the *HM* and *CD* approaches as described

before. The HAND index derived from the HYDROSHEDS database was used for masking and is shown in Figure 3.2(c)).

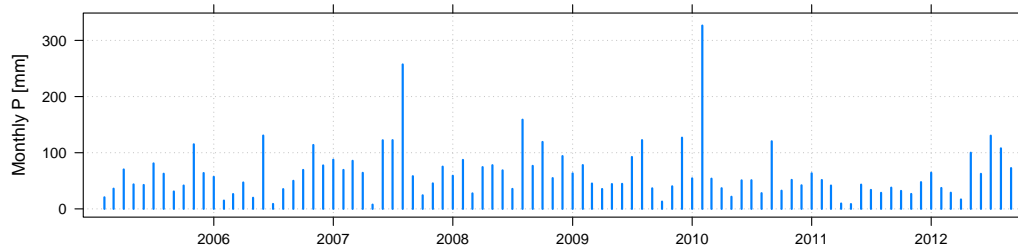


Figure 3.1: Monthly rainfall at Pershore College.

### 3.2.5 Validation approach

The produced flood maps were compared with a high-resolution flood map which was manually derived from airborne imagery. The aerial image acquisition was organised by the Environmental Systems Science Centre, University of Reading, in the morning of 24 July 2007. The images have a spatial resolution of 0.2 m (Mason et al., 2010). This reference dataset was also used for validation of a TerraSAR-X-derived flood map by Giustarini et al. (2013). The digitised flood extent is shown in Figure 3.2a). When aggregating this information to the ASAR grid, grid cells were considered as flooded if they were at least covered half by the high-resolution flood extent. Also, for the comparison, only the areas contained in the orthophotos was taken into account. Contingency matrices were built between the ASAR-derived flood maps and the reference flood extent. To further analyse the performance of the method for land-cover classes for which flood mapping has proven difficult in the past—such as urban areas—we additionally computed the accuracy measures for open and urban areas. These were derived from the CORINE land cover 2006 database (Büttner et al., 2010) The CORINE classes were aggregated into open and urban classes as shown in Table 3.1.

## 3.3 Results and Discussion

In this section, we first present the results of the time-series analysis. Then, the flood extents derived from the harmonic-model-based approach and the

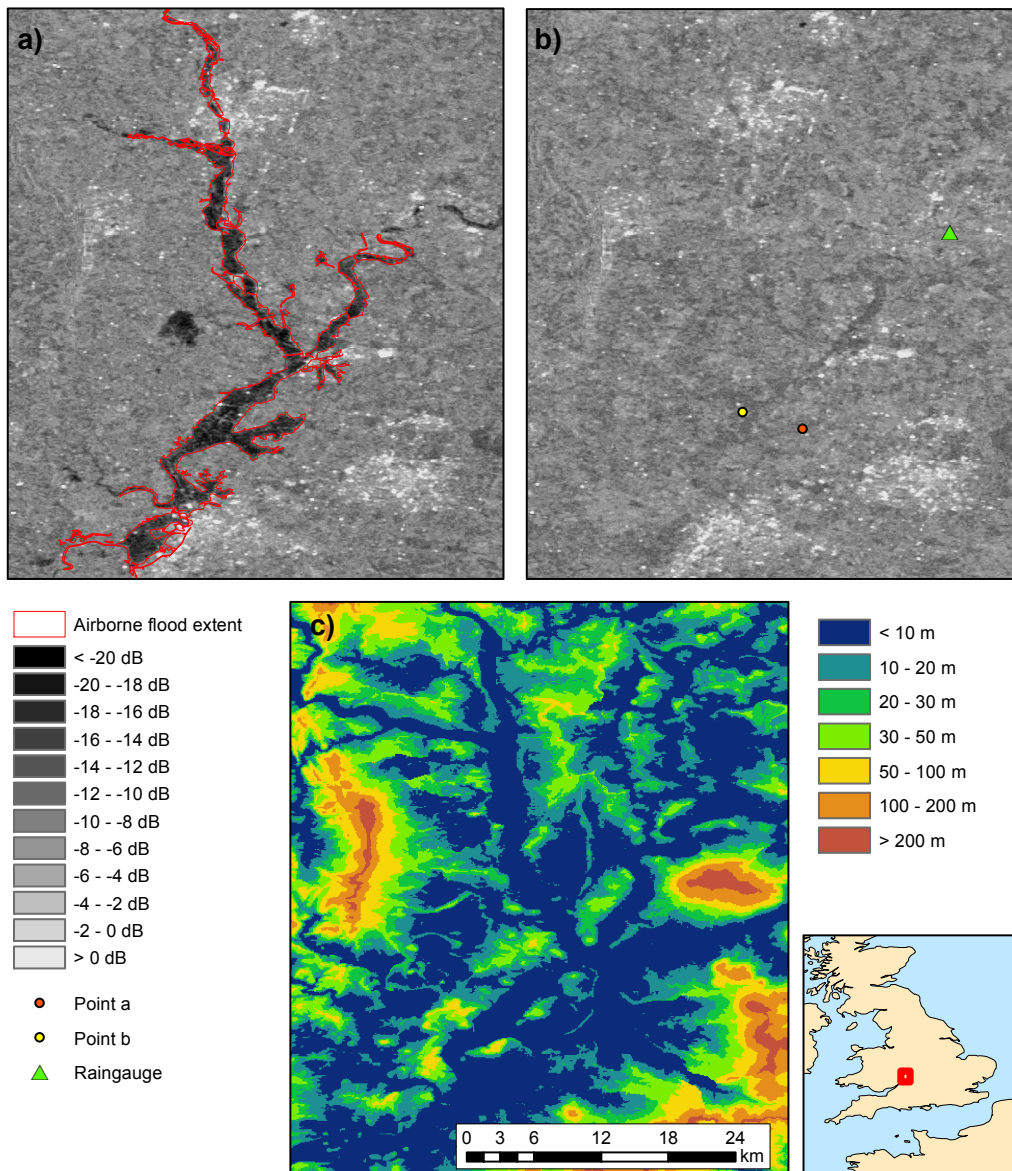


Figure 3.2: (a) ASAR scene acquired 23 July 2007 over the Severn River. The flood extent digitised from aerial imagery is shown in red. The map inset shows the position of the study area in the UK. (b) Non-flood ASAR scene acquired 22 August 2005. All backscatter units are in dB. Point (a) and (b) mark the locations for which time series are shown in Figure 3.3. The location of the rain gauge at Pershore College is given. (c) HAND index.

alternative change detection are compared with the reference dataset described in Section 3.2.5.

### 3.3.1 Time-series analysis

Figure 3.3 shows the  $\sigma^0(30^\circ)$  time series acquired between summer 2005 and spring 2012 over two sites in the study area which are used for agriculture according to the CORINE land cover 2006 database. The locations of the two sites are shown in Figure 3.2(b). Both sites were inundated during the floods of summer 2007. The two time series differ considerably from each other in terms of their backscatter dynamics: in the case of Figure 3.3(a), values range between ca.  $-13$  dB and  $0$  dB while the time series shown in Figure 3.3(b) is less dynamic with consistently lower values ranging between  $-13$  dB and  $-8$  dB. Both time series have their annual minima in late spring and early summer. A similar seasonality can be found in rainfall measured at Pershore College (Figure 3.1) suggesting that  $\sigma^0$  dynamics in this area are mainly governed by moisture supply.

Patterns similar to those in Figure 3.3(a) were found by Blaes et al. (2007) for winter cereals when comparing ASAR time series simulated from VV-polarised ERS measurements over Belgium although  $\sigma^0(30^\circ)$  encountered here is higher during winter. The lower dynamics of the second time series resemble

Table 3.1: Aggregation scheme of CORINE land-cover classes into urban and open terrain.

| CORINE Code | Description   | Aggregated class |
|-------------|---|------------------|
| 111         | Continuous urban fabric   | Urban            |
| 112         | Discontinuous urban fabric  |                  |
| 121         | Industrial or commercial units  |                  |
| 122         | Road and rail networks and associated land  |                  |
| 124         | Airports  |                  |
| 131         | Mineral extraction sites  |                  |
| 133         | Construction sites  |                  |
| 141         | Green urban areas   | Open             |
| 142         | Sport and leisure facilities  |                  |
| 211         | Non-irrigated arable land   |                  |
| 231         | Pastures  |                  |
| 243         | Land principally occupied by agriculture with significant areas of natural vegetation |                  |

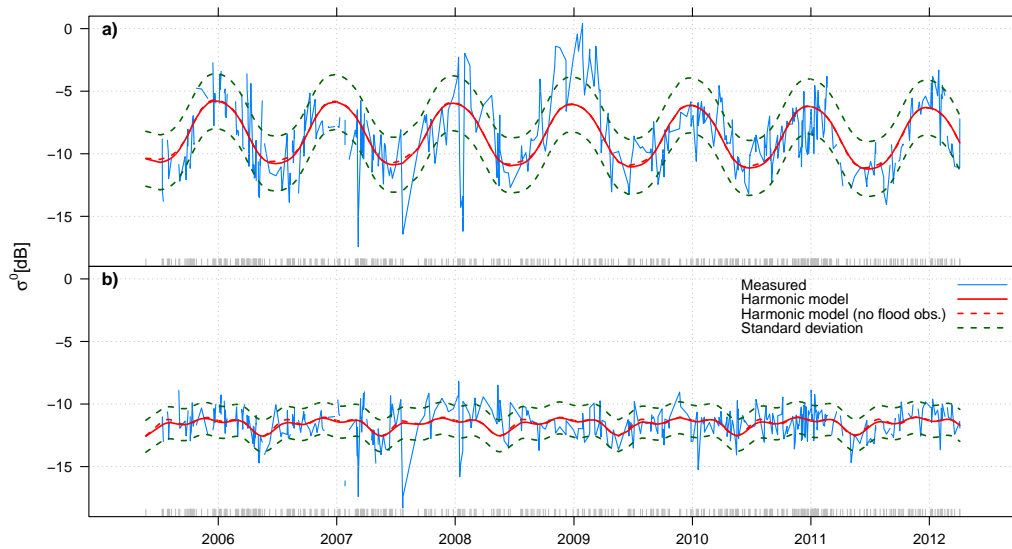


Figure 3.3: Time series of  $\sigma^0(30^\circ)$  (blue), harmonic model fitted to all observations (solid, red) and harmonic model after excluding flood observations (dashed, red) for two different points located in agricultural areas. The dashed green line marks the estimated model fit  $\pm 1$  standard deviation. Short grey ticks at the bottom of the figure represent the times of ASAR acquisitions. See Figure 3.2(b) for the locations of the two sampled points.

the seasonal pattern reported by the authors of that study for grassland. The large discrepancy between the two time series also shows that general information on land cover as it is contained in land cover databases such as CORINE, which is mainly based on optical EO data (Büttner et al., 2010), cannot be used to make assumptions about backscatter dynamics from agricultural areas.

A harmonic model was fitted to the time series to characterise backscatter behaviour under non-flooded conditions. Figure 3.3 shows that the harmonic models reproduce the overall dynamics well, especially the annual maxima in winter and minima in early summer. An important question is how single wet or dry years can influence the model fit. In Figure 3.3(a) it can be seen that higher  $\sigma^0(30^\circ)$  measurements were obtained during the winter of 2008/2009. With a total of 268 mm, precipitation in the preceding autumn season was higher than the 2005–2012 average of 197 mm. The year of 2011, on the other hand, had less rainfall than the average. This coincides with  $\sigma^0(30^\circ)$  measurements lying mostly below the fitted harmonic model. The overall impression is that the harmonic model represents the average seasonal behaviour of  $\sigma^0$  and that single wet or dry years exert a relatively low influence on the model fit.

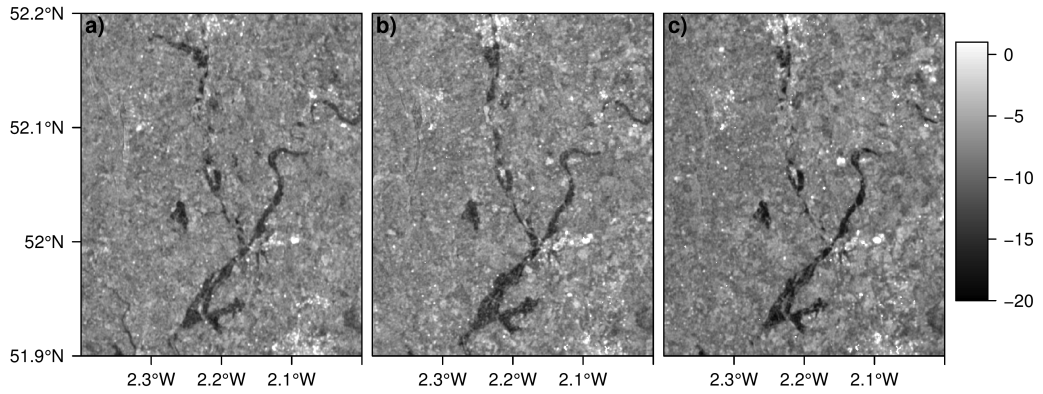


Figure 3.4:  $\sigma^0(30^\circ)$  in dB measured by ENVISAT ASAR on (a) 3 March 2007, (b) 17 January 2008 and (c) 18 January 2010 over the study area.

It can be observed that  $\sigma^0(30^\circ) < \hat{\sigma}^0 - 2 \cdot s_\epsilon$  during March 2007, July 2007 and January 2008. The second time series (Figure 3.3) also shows an incidence for which this condition is true in January 2010. Visual inspection of the respective ASAR scenes reveals that a large fraction of the study area was flooded on these dates (Figure 3.4). This result indicates that the proposed method also has the potential to be used for detecting flood events in large databases of image time series. This property could be helpful for building databases of historic floods, especially in poorly equipped regions where no *in-situ* runoff data are available.

However, if the dates of the flood events are not known *a-priori*, the low  $\sigma^0$  measurements taken during a flood may influence the harmonic model fit. To characterise the impact of the flood events, the scenes acquired during the previously mentioned dates were excluded before fitting the harmonic model. The result is shown as dashed red lines in Figure 3.3. It can be seen that the solid and dashed lines almost coincide. There are small deviations between the models mostly in summer when the model fitted to the whole dataset predicts marginally lower values than the adjusted version. Nevertheless, the deviations are small enough that it can be concluded that the flood observations do not influence the harmonic model calibration when the number of non-flood scenes greatly outweigh the flood scenes as it is the case here.

### 3.3.2 Flood extent classification

For any given date it is possible to create a map of the obtained residuals. Figure 3.5(a) shows the standardised *HM* residuals  $\epsilon^{\text{std}}$  for the flood event on

23 July 2007. The change in  $\sigma^0(30^\circ)$  between the flood and non-flood image from August 2005 is shown in Figure 3.5(b)). Both images were scaled between 0 and 1 to make them comparable to each other by accounting for the difference in units between the two maps (times  $s_\epsilon$  in case of *HM*, dB in case of *CD*). Visual inspection shows that the *HM* residuals have a higher contrast between water and dry areas than the *CD* image. This impression is supported by the histogram densities. In the *HM* histogram (Figure 3.5(c)), a second smaller peak is clearly visible with a maximum at a grey value of ca. 0.2. The *CD* distribution, on the other hand, only has a long left tail without pronounced bimodal characteristics (Figure 3.5(d)). Masking the residuals with the HAND index in both cases reinforced this overall impression by lowering the relative frequency of dry pixels and therefore increasing the water peak. The difference in contrast also has an effect on threshold optimisation. The obtained Otsu value for the *HM* residuals is almost at the location of the local minimum between the two modes of the histogram, which is where a human operator would typically set the threshold after visual inspection (e.g. Bartsch et al., 2008). Meanwhile, the automatic threshold for the *CD* image lies closer to the image median and is therefore set too high. Figure 3.5 also illustrates the impact of masking non-flood-prone areas on the optimisation of the threshold value. Without masking, the estimated value is again shifted towards the median of the distribution for both *HM* and *CD* approaches (dashed red lines in Figure 3.5(c) and (d)).

As a result of the increased contrast, the binary flood map derived using the *HM* approach seems less noisy than the corresponding *CD* map with less isolated pixels located far away from the main channel and a more contiguous flood extent along the main channel. Also the flood boundaries are smoother in the first case. The topography-derived mask covers about 61% of the area of interest (Figure 3.6).

The different consistencies of the derived flood extents are also represented in Table 3.2 which shows the results of the comparison between the classified inundated area with the flood extent that was manually digitised from high-resolution aerial imagery. For both techniques, producer's and user's accuracies for the class *flooded* were higher than 75% except in urban areas. It can be seen that the accuracies for method *HM* are consistently higher than for method *CD*. It is noteworthy that although result *CD* contains many falsely classified flood pixels far away from the reference extent user's accuracies are still relatively high. This is related to the fact that only a rather narrow strip along the floodplain was mapped in the orthophotos so that a large part of the area of interest was not included in the analysis. The relatively low producer's

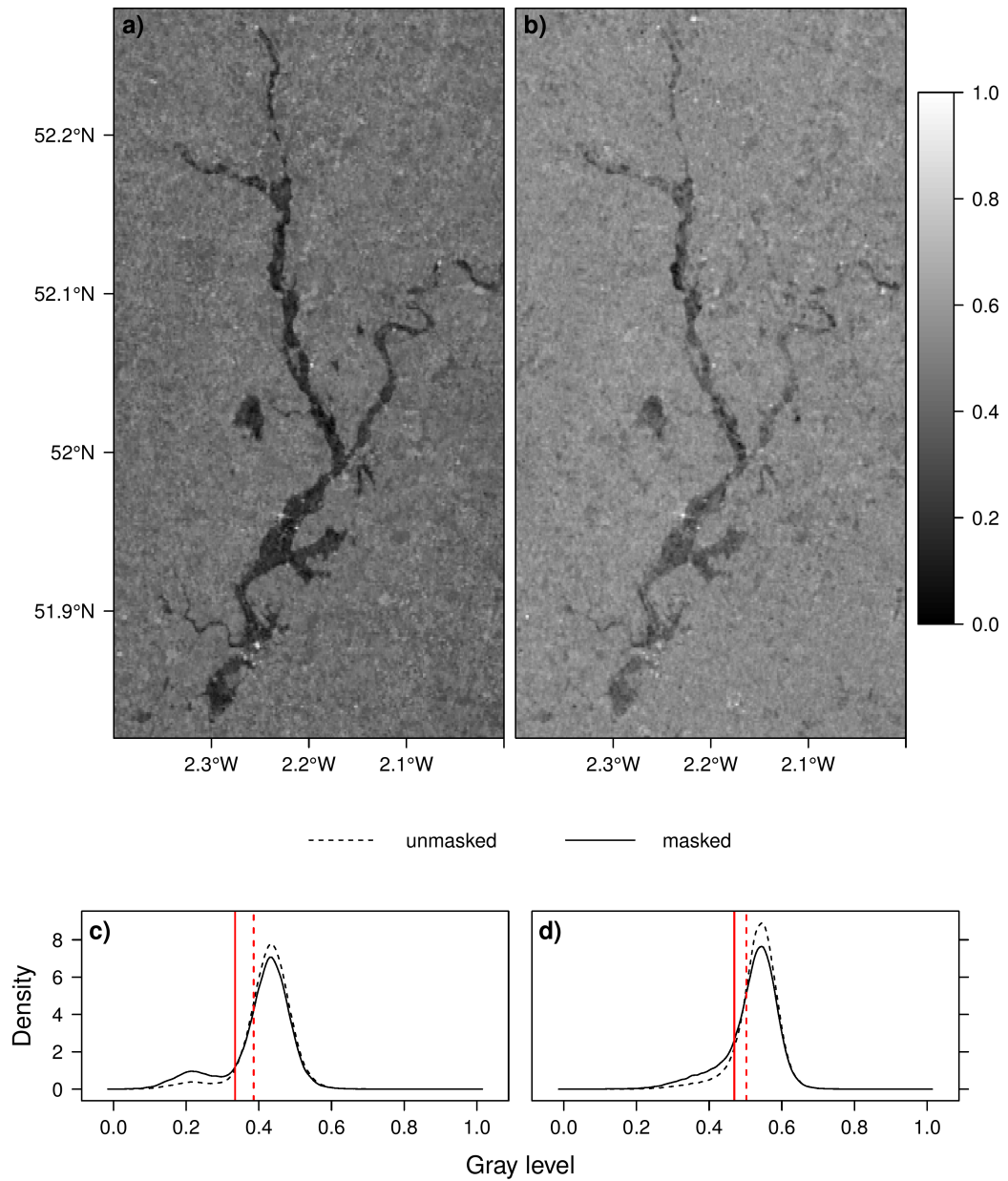


Figure 3.5: In the top panel, figure (a) shows standardised residuals of the harmonic model for the scene acquired over the Severn River on 23 July 2007. Plot (b) shows the change in backscatter between 22 August 2005 and 23 July 2007. At the bottom, figure (c) shows the kernel densities for figure (a) and figure (d) the densities of figure (b). The dashed line represents the distribution before and the solid line after masking. The vertical red lines mark the Otsu threshold value estimated before (dashed) and after masking (solid). The images were rescaled from change in dB/times  $s_\epsilon$  to  $[0, 1]$  for better visual comparability.

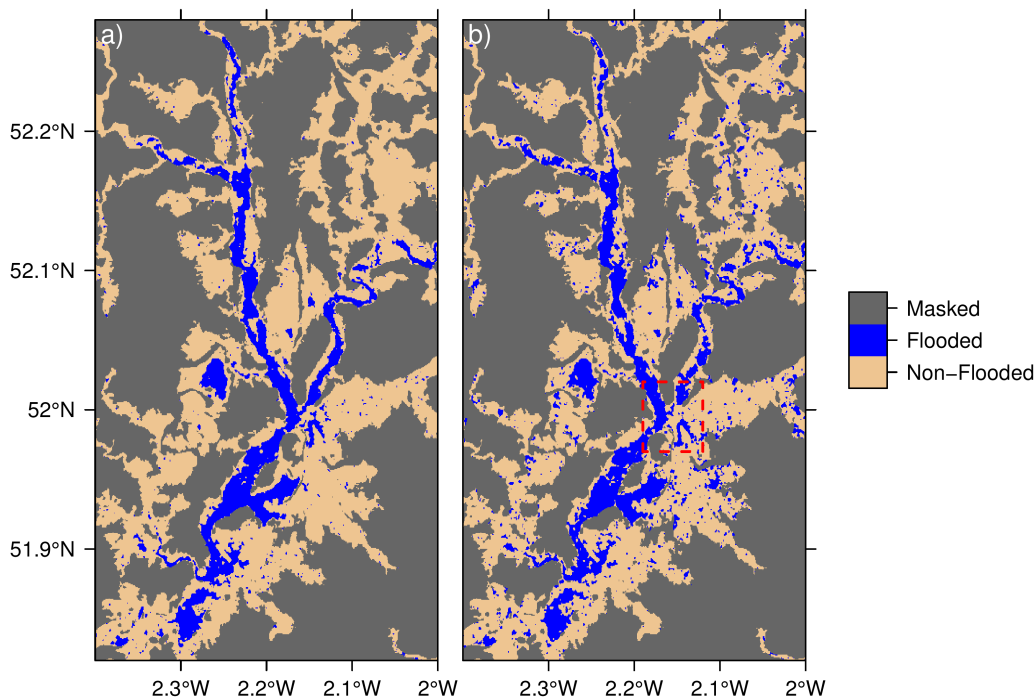


Figure 3.6: Extracted flood extents for 23 July 2007 using (a) the harmonic model approach and (b) change detection. The red rectangle shows the extent of the maps in figure 3.7.

accuracies found for both methods point towards an underestimation of the reference flood extent, most likely due to the much lower spatial resolution of the ASAR WS imagery with respect to the airborne data.

For urban areas all accuracies are below 50%. This large misclassification is consistent with the expectation that large portions of floods within urban areas remain unseen by coarse-resolution ASAR data due to layover and radar shadow. A previous study comparing water levels derived from the same ASAR scene for the area of Tewkesbury with simulated water levels from a hydraulic model reports an underestimation of almost 1 m on average (Schumann et al., 2011). It is furthermore noteworthy that in urban areas the difference in accuracies between the two methods is higher than in open areas. However, considering the comparatively small number of aggregated reference flood pixels that were found within urban areas (ca. 500) it is not possible to make any conclusive statements about whether the *HM* consistently outperforms the alternative method in this respect. Nevertheless, it can be seen that in the vicinity of urban areas the proposed approach shows a more consistent waterline which borders directly the urban areas (Figure 3.7(a)) while for method

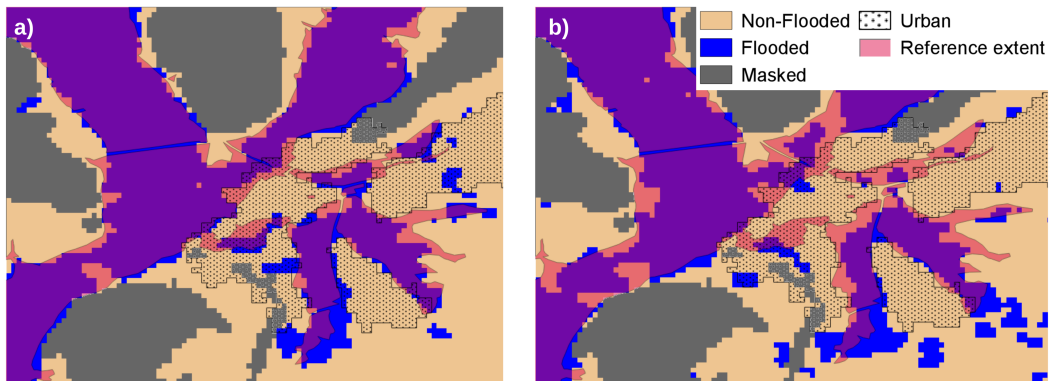


Figure 3.7: Detail of extracted flood extents around Tewkesbury for 23 July 2007 using the (a) harmonic model approach (b) and change detection. Additionally, the reference flood extent from airborne photos and urban areas are shown.

*CD* there exists usually a gap (Figure 3.7(b)). This is most probably a result of the use of multi-temporal and multi-angular data within the *HM* approach leading to lower noise levels in the residual image.

The approach only classifies pixels as flooded if they are not usually covered by water. This means that permanent water bodies would not be correctly identified using the proposed approach. However, in the presented case study this was not relevant due to the fact that no larger permanent water bodies are present in the study area according to the CORINE land cover database. For water bodies to be reliably classified from ASAR WS data they should cover an area of at least 2 ha (Bartsch et al., 2008). In other cases, where permanent water is detectable it could be classified by using a similar approach as proposed by O’Grady et al. (2013) who used the angular dependency of  $\sigma^0$ ,  $\beta$ , which was defined in equation 3.2.

Table 3.2: Producer’s and user’s accuracies for the water class across all land-cover classes and for urban and open areas separately.  $N$  is the number of pixels used for each comparison. All values are expressed in %.

|                  | Overall |            |        | Urban |            |        | Open  |            |        |
|------------------|---------|------------|--------|-------|------------|--------|-------|------------|--------|
|                  | $N$     | Producer’s | User’s | $N$   | Producer’s | User’s | $N$   | Producer’s | User’s |
| Harmonic model   | 88626   | 82.5       | 86.9   | 8792  | 36.3       | 47.8   | 79089 | 83.6       | 87.7   |
| Change detection |         | 76.8       | 81.3   |       | 24.2       | 39.3   |       | 78.1       | 82.0   |

When interpreting the results of the validation it should be kept in mind that the airborne imagery was acquired about 23 h after the ASAR scene and that the flood extent could have changed in the meantime. Both the ASAR and airborne images were acquired after the flood peak had been reached on 22 July which means that the water level was declining at the time. According to Zwenzner and Voigt (2009), the difference in water height between 23 and 24 July measured at Mythe Bridge in Tewkesbury was ca. 0.5 m. A high-resolution LiDAR digital terrain model is available from the Environment Agency of England and Wales for the floodplain of the Severn which shows steep slopes around most of the floodplain. Around Mythe Bridge, the difference in water level corresponds to a recession of the water line by ca. 10 m which is well below the pixel size of ASAR and can therefore be neglected in this study using medium-resolution data.

### 3.4 Perspectives

While in the presented study the method was applied to a well-researched single flood event the obtained results suggest that harmonic analysis can also be used to detect flood events in historic multi-temporal image datasets. This could open interesting perspectives for the application of the algorithm in ungauged basins where flood records are missing and to complement existing runoff records which have been deteriorating since the early 1990s (Vörösmarty, 2002).

On the other hand, the algorithm is relevant in the light of more recent missions which provide SAR data with denser temporal sampling than that achieved with ENVISAT ASAR. The two-satellite Sentinel-1 constellation is planned to cover land masses globally every six days, with almost daily coverage over Europe and Canada once both satellites are operational (Torres et al., 2012). Shorter sampling intervals offer unique advantages for multi-temporal approaches which should lead to a better characterisation of backscatter characteristics of land surfaces and to higher accuracies for flood mapping. Moreover, according to the orbit specifications of the Sentinel-1 mission, every point on earth will only be acquired from up to three different orbits and most regions only from a single orbit (Hornacek et al., 2012). This means that the range of different local incidence angles would be very limited and a change detection using multi-temporal data such as the one proposed here would not require a correction as the one that was applied in this case.

On the other hand, the higher spatial resolution would possibly introduce

a further source of uncertainty due to imperfect image co-registration and speckle or noise in the images. For operational purposes, the harmonic model could be calibrated after averaging  $\sigma^0$  over several pixels. This would minimise the effect of noise on the quality of the harmonic model.

One of the main disadvantages of the approach is the increased computational cost created by the need to preprocess a SAR time series consisting of  $> 200$  scenes and to calibrate the harmonic model. In an operational setting, however, the computational load can be decreased by separating the harmonic model calibration from the actual flood delineation. A database of harmonic model coefficients can be created during a reprocessing step in which the available scenes are processed. New flood maps can then be produced by estimating a reference to be expected from the coefficients and comparing it to the near-real-time measurement. The underlying assumption that the parameters are stable in time could be violated e.g. in case changes in land use have taken place. For example, the backscatter characteristics would change if buildings are constructed in a former agricultural area. Therefore, the derived parameters should be updated by adding further scenes to the historical backscatter data in regular intervals. The assumption of stationarity could also be verified by using official land-cover-change maps to make sure that no change has occurred.

It should also be noted that the main reason for choosing the Otsu method for the classification of flooded and non-flooded endmembers was the fact that it is a simple, well-known thresholding method. As already mentioned in Section 3.2.3, the presented combination of Otsu thresholding and HAND masking could be problematic in cases where topography is less pronounced and only a small area above the HAND threshold will be masked out. In an operational setting, other classification approaches may be used which do not suffer from the same shortcomings. Object-based approaches often outperform pixel-based approaches for high-resolution data such as Sentinel-1 or TerraSAR-X (e.g. Martinis et al., 2011; Mason et al., 2012). A number of different pixel- and object-based approaches was outlined in Section 3.1.

## 3.5 Conclusions

A change detection approach for flood mapping from multi-temporal SAR data was introduced. The procedure was evaluated for a large-scale flood event that took place in summer 2007 in the south-western UK. Harmonic analysis was used to characterise normal backscatter behaviour in a multi-temporal ASAR

image time series. Flood maps were derived from the harmonic model residuals and validated using a reference dataset that had been manually digitised from high-resolution airborne photographs. Furthermore, a masking approach was presented based on the HAND index to increase the efficiency of a well-known histogram-based optimised thresholding algorithm. The comparison with reference data yielded very low error margins in terms of the detected flood waterlines.

The findings suggest that the approach offers considerable advantages in comparison to simple change detection. Noise is greatly reduced by using multi-temporal data. Furthermore, the need for an operator to manually select a pre-flood reference scene is eliminated by assembling the reference from available historic data. The presented approach is therefore especially suitable for automatic flood extent retrieval since no interaction by the user is required.

It should be noted that the potential for application of the proposed approach is not limited to flood mapping. By adapting the different parameters of the processing chain it would also be possible to detect and map other disturbances which temporarily alter the backscattering behaviour of a land surface such as snow cover.

# Chapter 4

## Probabilistic mapping of flood-induced backscatter changes in SAR time series

*This chapter is an edited version of: Schlaffer, S., Chini, M., Giustarini, L., Matgen, P., 2017. Probabilistic mapping of flood-induced backscatter changes in SAR time series. International Journal of Applied Earth Observation and Geoinformation, 56: 77–87. For the original see <http://dx.doi.org/10.1016/j.jag.2016.12.003>.*

### 4.1 Introduction

Floods are among the most frequent natural disasters. Recent exposure estimates place a number of almost 1 billion people in areas that are subject to high degrees of river or coastal flood hazard with the highest numbers located in Asia (Jongman et al., 2012). Losses are expected to increase substantially due to climate change and economic growth in flood-prone areas, especially in emerging economies and developing countries (Winsemius et al., 2015). Flood maps based on space-borne remote sensing data can provide timely, cost-efficient synoptic overviews for disaster response (Pierdicca et al., 2013b; Schumann et al., 2016). Moreover, these maps can help to improve the quality of flood forecasts (Grimaldi et al., 2016), either as reference maps for calibration and validation of hydrological and hydraulic models (Di Baldassarre et al., 2009; Tarpanelli et al., 2013; Wood et al., 2016) or through

data assimilation into hydraulic models, typically after transformation to water levels with the help of a digital elevation model (Giustarini et al., 2011; Matgen et al., 2010). Synthetic aperture radar (SAR) is of special importance for flood extent mapping. In contrast to optical sensors, they can operate at day and night times and are mostly able to penetrate cloud cover and rainfall (Danklmayer et al., 2009; Richards, 2009), both of which are often present in flood situations. Moreover, SAR imagery from recent missions can provide data at low latency times of typically less than 48 hours and 12 hours in the case of Sentinel-1 (Torres et al., 2012) and COSMO-SkyMed (Covello et al., 2010), respectively, facilitating near-real-time operations for disaster management (Pulvirenti et al., 2011b; Twele et al., 2016). Calm water surfaces act as specular reflectors from which a low amount of energy is reflected back to the sensor, usually resulting in a high contrast between water and land surfaces in SAR images. Not surprisingly, this principle is used by a number of approaches for flood detection from SAR data that have been published in recent years (Schumann and Moller, 2015). Only a few examples can be given here, such as manual (Bartsch et al., 2012; Chini et al., 2013) and automatic radiometric thresholding (Martinis et al., 2015), change detection (Giustarini et al., 2013; Long et al., 2014), image grey-value distribution modelling and region growing (Giustarini et al., 2013; Matgen et al., 2011; Pulvirenti et al., 2016), or modelling using active contours (Horritt, 1999). However, despite the high sensitivity of SAR sensors to the presence of surface water, uncertainties in flood delineation can arise from different sources: ambiguous radar backscatter signatures may arise due to the roughening of water surfaces by wind or heavy rain (Pierdicca et al., 2013a) or due to partly submerged vegetation (Kasischke et al., 2009; Schlaffer et al., 2016). As a result of these factors, the backscatter coefficient  $\sigma^0$  can increase by several dB depending on incidence angle, polarisation and wavelength (Santoro and Wegmüller, 2014). Dry, bare areas, on the other hand, may exhibit backscatter characteristics similar to those of open water surfaces (O’Grady et al., 2011). These factors can lead to a substantial over- or under-estimation of the true area covered by flood water. In addition, speckle is a phenomenon inherent to SAR imagery that can affect the quality of the retrieved flood extent maps through random variations in backscatter intensity within homogeneous target areas (Giustarini et al., 2015). Users of flood maps, not only within the scientific community but also disaster risk managers, have expressed strong interest in estimates of the uncertainty resulting from these and other factors (Schumann et al., 2016). Only recently, methodologies have been proposed to produce uncertain flood maps based on fuzzy set theory (Martinis and Twele, 2010; Pierdicca

et al., 2008) and Bayesian statistics (D’Addabbo et al., 2016; Giustarini et al., 2016; Refice et al., 2014; Westerhoff et al., 2013). These approaches have in common that they yield maps showing values in the interval  $[0, 1]$ , where the extremes mark certainly flooded and non-flooded pixels and intermediate values quantify different degrees of uncertainty. If flood probability values  $p_F$  are obtained binarisation of the probabilistic maps is a straightforward task as, in a Bayesian framework, each observation is assigned the class label which has the highest posterior probability of all possible candidate classes (Duda et al., 2001).

Nevertheless, a critical step in the computation of uncertain flood maps is the estimation of the necessary function parameters, i.e. of the class membership functions or the class-conditional probability density functions (PDFs). For example, fuzzy membership functions have been estimated using the output of electromagnetic scattering models by Pulvirenti et al. (2011a). However, information about soil, vegetation and land cover is typically needed for parameterising such models and additional parameters may require calibration. Parameters of conditional PDFs can be estimated from the grey-value histogram of a flood scene under the assumption that flooded areas cause a multimodal distribution. The bimodality of a flood scene and, therefore, the separability between flooded and non-flooded classes, strongly depend on the portion of the image covered by flooded areas (Chini et al., 2016; Martinis et al., 2009). In order to account for this problem, Giustarini et al. (2016) have used a split-based approach and maximum likelihood estimation to model the PDFs of  $\sigma^0$  values of flooded and non-flooded areas and then applied Bayes’ theorem to compute flood probabilities. Additionally, the study has introduced the reliability diagram (Wilks, 2011) as a tool for evaluating satellite-based probabilistic flood maps. Alternatively,  $\sigma^0$  PDFs of flooded and non-flooded areas can be estimated based on historic SAR data. Westerhoff et al. (2013) trained a probabilistic flood classifier using full time series of ENVISAT Advanced SAR (ASAR) acquisitions and an ancillary permanent water mask. Based on the estimated PDFs, the probability of a backscatter value belonging to the water class was calculated for each pixel. However, the influence of different land-cover classes was not accounted for when building the backscatter histograms for land areas based on  $1^\circ \times 1^\circ$  tiles. This may have contributed to the observed misclassifications in dry regions where water and land PDFs overlap (Westerhoff et al., 2013).

Change detection is a tool which is commonly used to account for some of the effects introduced by the occurrence of different land-cover types within a scene. By quantifying the change between a flood image and a reference image

acquired before or after the flood it is possible to distinguish permanent water bodies from areas that are affected by the flood event (Serpico et al., 2012). However, finding a suitable reference image is not always a straightforward task. For example, it is recommended to use a scene that was acquired during the same season as the flood image to account for the effects of seasonally varying soil moisture and vegetation state (Hostache et al., 2012). Finding a scene acquired during the same season as the flood image is often further complicated by the unequal sampling intervals that are common for many sources of remote sensing data (Mercier et al., 2009). A harmonic model fitted separately to each pixel of an ASAR image time series spanning several years was used by Schlaffer et al. (2015) to estimate spatially and seasonally varying backscatter and the corresponding residuals for an actual flood image. However, the threshold value for deciding whether a pixel of the residual image was flooded or not was derived using an automatic thresholding approach (Otsu, 1979) suffering again from the aforementioned limitations in terms of class separability due to a potential lack of a bimodal grey-value histogram.

Open questions, therefore, still exist with respect to the estimation of PDFs conditioned on land cover and season from historic SAR data and the appropriate use of change detection methods in probabilistic flood mapping approaches. In this study, we combine the multi-temporal change detection approach of Schlaffer et al. (2015) to estimate seasonally and spatially dependent  $\sigma^0$  for non-flooded areas with the approach by Westerhoff et al. (2013) who retrieved water backscatter PDFs from historic SAR imagery and a permanent water layer. The objective is to compute probabilistic flood maps while taking into account seasonal and land-cover effects which is equivalent to estimating a seasonally and spatially dependent threshold value for deciding whether a SAR image pixel is flooded or not. The results are validated using a reference flood map obtained from high-resolution airborne imagery. The remainder of the article is structured as follows: in Section 4.2, the study area, the datasets and the methods for computing flood probability maps are described. The results for the case study are reported and discussed in Section 4.3. Finally, Section 4.4 summarises the study.

## 4.2 Methods

In the first part of this section, the principle behind probabilistic flood mapping is introduced. Then, the methods used for processing the SAR time series and estimating backscatter PDFs from flooded and non-flooded areas are presented.

Finally, the section includes a description of the test case and the validation approach.

### 4.2.1 Flood probability estimation and classification

The probability of a pixel being flooded has been calculated using Bayes' theorem by several authors (e.g. Giustarini et al., 2016; Refice et al., 2014; Westerhoff et al., 2013). Under the assumption that a pixel at a certain point in time can have either state  $F$  (flooded) or  $nF$  (non-flooded) the posterior probability of the pixel belonging to class  $F$  given an observation  $x$  is defined as

$$p(F|x) = \frac{p(x|F)p(F)}{p(x)}, \quad (4.1)$$

where

$$p(x) = p(x|F)p(F) + p(x|nF)p(nF), \quad (4.2)$$

and  $p(x|F), p(x|nF)$  are the conditional PDFs of  $x$  being observed when the pixel is flooded and non-flooded, respectively.  $p(x)$  is the probability density of  $x$  when the pixel is either flooded or non-flooded and  $p(F)$  represents our prior knowledge about the probability of the pixel being flooded. If no prior information is available a so-called non-informative prior can be used, i.e.  $p(F) = p(nF) = 0.5$ . Giustarini et al. (2016) evaluated the sensitivity of the flood mapping result towards different priors and found that the use of a non-informative prior led to acceptable results.

If both classes  $F$  and  $nF$  are characterised by normally distributed features with means  $m_F, m_{nF}$  and variances  $s_F^2, s_{nF}^2$ , respectively, the separability between the classes can be quantified using the metric  $M = |m_F - m_{nF}| / (s_F + s_{nF})$  (Kaufman and Remer, 1994). Any increase in the differences between the population means or any reduction of their variances should, therefore, lead to a better separation between flooded and non-flooded areas. This was a major aim driving the design of the data processing chain described in the following sections.

### 4.2.2 Data processing and parameter estimation

#### SAR image processing

The conditional PDFs for  $\sigma^0$  from flooded and non-flooded areas were parameterised based on a time series acquired by the ASAR sensor on board of ENVISAT, which was operated by the European Space Agency (ESA) between

2002 and 2012. The area of interest (AOI) used for parameterisation is located in the south-west of the United Kingdom (UK), roughly covering the River Severn catchment (Figure 4.1). A total number of 677 ASAR scenes for the years 2005-2012 was available on ESA’s Grid Processing On Demand (GPOD) facility for this study. All scenes were acquired in Wide Swath (WS) mode and VV polarisation at a spatial resolution of 150 m. The equivalent number of looks of ASAR WS medium resolution images is estimated to be  $> 15$  (ESA, 2012). 375 images were available in descending (around 10 *a.m.*) and 302 in ascending orbit (around 10 *p.m.*). The processing chain is described in more detail by Schlaffer et al. (2015) and is, therefore, only outlined in the following, highlighting the main differences. The Level 1b images were geocoded and terrain-corrected using the Range-Doppler approach (Cumming and Wong, 2004). The scenes were then co-registered to a common grid definition with a pixel spacing of  $2.3''$ , corresponding to ca. 75 m at the equator. Since the ASAR scenes were acquired from different tracks the influence of local incidence angle  $\theta$  had to be corrected using the linear relationship

$$\sigma^0(\theta_{\text{ref}}) = \sigma^0 - \beta(\theta - \theta_{\text{ref}}), \quad (4.3)$$

where  $\theta_{\text{ref}}$  is the reference local incidence angle to which the scenes are normalised, typically in the range  $30^\circ$ – $40^\circ$  (Pathe et al., 2009; Wagner et al., 1999c). The slope parameter  $\beta = d\sigma^0/d\theta$  was estimated for each pixel using linear regression over the co-registered pairs of  $\sigma^0$ - $\theta$  observations. Furthermore,  $\beta$  was derived separately for ascending and descending passes to partly account for the effects of azimuthal anisotropy that have been reported for e.g. urban areas and topographically complex terrain (Bartalis et al., 2006), both of which occur in the study area. As  $\beta$  (equation 4.3) has been shown to be steeper for water bodies than for most land surfaces (O’Grady et al., 2014) it is hypothesised that the difference between  $m_F$  and  $m_{nF}$  and, hence, the separability metric  $M$  should increase when higher values of  $\theta_{\text{ref}}$  are used. Therefore,  $\sigma^0$  was normalised to  $30^\circ$  and  $40^\circ$  to test for the impact on the quality of the flood mapping. In the following, for the sake of legibility, normalised backscatter  $\sigma^0(\theta_{\text{ref}})$  is written simply as  $\sigma^0$ .

### Parameterisation of land and water PDFs

The parameters of the PDFs for backscatter from classes  $F$  and  $nF$  were estimated by analysing time series of historic ENVISAT ASAR WS data. The PDF corresponding to non-flooded pixels was estimated for each pixel

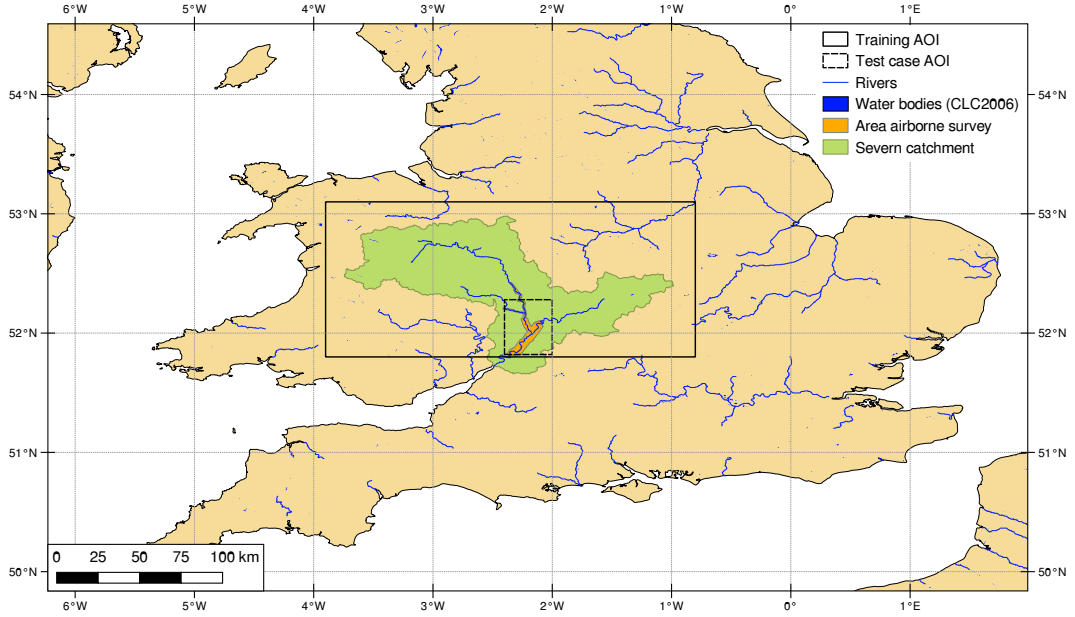


Figure 4.1: Location of the study area. The solid rectangle shows the AOI used for estimating the  $\sigma^0$  PDF for water. The dashed rectangle shows the area used for testing the approach.

separately in order to take into account the backscatter signature that the corresponding land surface would exhibit under "normal", i.e. non-flooded, conditions. In contrast, Westerhoff et al. (2013) have used all land pixels in a tile covering an area of  $1^\circ \times 1^\circ$  to estimate the parameters for computing  $p(\sigma^0|nF)$  leading to a higher backscatter variance  $s_{nF}^2$  due to the pooling of observations from different land-cover types into a single sample. Here,  $s_{nF}^2$  was further reduced by assuming a seasonal dependency in the backscattering behaviour as  $\sigma_{nF}^0$  is partly governed by soil moisture and vegetation which underlie a seasonal cycle (Schlaffer et al., 2016; Van doninck et al., 2012). Seasonal backscatter was estimated using a harmonic model as proposed by Schlaffer et al. (2015):

$$\hat{\sigma}_{nF}^0(t) = \overline{\sigma_{nF}^0} + \sum_{i=1}^k \left[ c_i \cos\left(\frac{2\pi it}{n}\right) + s_i \sin\left(\frac{2\pi it}{n}\right) \right], \quad (4.4)$$

where  $\overline{\sigma_{nF}^0}$  is  $\sigma_{nF}^0$  averaged over time,  $k$  is the number of harmonic terms and  $n$  is the number of time steps per year. A number of  $k = 3$  harmonic terms was used here to reproduce processing taking place on a temporal scale of ca. four months. Further information about the rationale behind this choice are given by Schlaffer et al. (2016). The parameters  $c_i$  and  $s_i$  were estimated using

least-squares optimisation. In order to account for unequal temporal sampling, equation 4.4 was fit to 10-day  $\sigma^0$  composites. As a result, the harmonic model residuals  $\varepsilon_{nF}$ , which are assumed to be independent and normally distributed, were computed for each time step:

$$\varepsilon_{nF}(t) = \sigma_{nF}^0(t) - \hat{\sigma}_{nF}^0(t) N(m_{\varepsilon,nF} = 0, s_{nF}). \quad (4.5)$$

The assumption of normal distribution around zero holds for backscatter observations during normal, non-flooded conditions. These normal conditions are expressed in terms of equation 4.4, which is fit to a time series spanning several years. The residual variance  $s_{nF}^2$  was estimated as

$$s_{nF}^2 = \frac{1}{N - 2k - 1} \sum_{j=1}^N \varepsilon_{nF,j}^2, \quad (4.6)$$

where  $N$  is the number of observations. During a flood event, it has been observed that  $\sigma^0(t) \ll \hat{\sigma}_{nF}^0(t)$  due to specular reflection, i.e.  $\varepsilon$  becomes strongly negative, with typically  $\varepsilon(t) < -2s_{nF}$  (Schlaffer et al., 2015). Note that, instead of backscatter  $\sigma^0$ ,  $\varepsilon$  is used to estimate flood probability  $p(F|\varepsilon)$  according to equation 4.1. The benefit of using  $\varepsilon$  rather than  $\sigma^0$  for computing flood probability is that  $\text{Var}[\varepsilon] \leq \text{Var}[\sigma^0]$  as the portion of the total variance in the  $\sigma^0$  time series caused by periodic variations is explained by equation 4.4. As described earlier for  $\beta$ , the parameters in equation 4.4 were estimated separately for ascending and descending orbital nodes to limit the effects of azimuthal anisotropy.

Backscatter from open water surfaces was also assumed to be normally distributed as the Gaussian PDF represents a suitable approximation of the distribution of logarithmically transformed  $\sigma^0$  from uniform targets with a sufficiently high number of looks (Xie et al., 2002). Its mean and variance were estimated based on observations over permanent open water bodies, similar to the approach proposed by Westerhoff et al. (2013). For this purpose, reference land-cover information from the CORINE land-cover 2006 (CLC 2006) dataset (Büttner et al., 2010) was taken into account. In order to limit the impact of mixed pixels on the PDF parameter estimation all pixels located along the edges of water bodies were not taken into account. Backscatter time series for all water bodies were extracted from the multi-temporal database and normalised to a local incidence angle  $\theta_{\text{ref}}$  using equation 4.3. The backscatter coefficient over open water,  $\sigma_F^0$ , is mainly dependant on water surface roughness which is difficult to determine. As no further information was available on

seasonal variations in wind speed and direction, we assumed the moments of the distribution,  $E[\sigma^0|F]$  and  $\text{Var}[\sigma^0|F]$ , to be time-invariant:

$$E[\sigma^0|F, t_1] = E[\sigma^0|F, t_2] = \dots = E[\sigma^0|F, t_n] = m_F \approx \overline{\sigma_F^0}, \quad (4.7)$$

$$\text{Var}[\sigma^0|F, t_1] = \text{Var}[\sigma^0|F, t_2] = \dots = \text{Var}[\sigma^0|F, t_n] \approx s_F^2. \quad (4.8)$$

In order to make the PDF of  $\sigma_F^0$  comparable to the PDF of harmonic model residuals  $\varepsilon_{nF}$ , its mean value  $\overline{\sigma_F^0}$  had to be transformed by offsetting it with the mean backscatter for the respective pixel  $\overline{\sigma_{nF}^0}$ :

$$E[\varepsilon|F] = E(\sigma^0|F) - E(\sigma^0|nF) \approx \overline{\sigma_F^0} - \overline{\sigma_{nF}^0} = \overline{\varepsilon_F}, \quad (4.9)$$

whereas

$$\text{Var}[\varepsilon|F] = \text{Var}[\sigma^0|F] \approx s_F^2. \quad (4.10)$$

After having estimated the parameters for the flooded and non-flooded PDFs, equations 4.1 and 4.2 can be rewritten as

$$p(F|\varepsilon) = \frac{p(\varepsilon|F)p(F)}{p(\varepsilon)} = \frac{p(\varepsilon|F)p(F)}{p(\varepsilon|F)p(F) + p(\varepsilon|nF)p(nF)}. \quad (4.11)$$

In the following, we will write  $p_F$  instead of  $p(F|\varepsilon)$  for simplicity.

In the asymmetric case, i.e. when  $s_F^2 \neq s_{nF}^2$ ,  $p_F$  will again increase for large positive  $\varepsilon$  (Duda et al., 2001) so that high flood probability values may be obtained for positive outliers. However, backscatter values typical for calm, open water are usually caused by specular reflection and, therefore, can be expected to be lower than backscatter from land. In consequence, the second decision boundary for high  $\varepsilon$  was not considered. This was implemented by constraining  $p_F$  to decrease monotonically with increasing  $\varepsilon$ , an approach also used by Giustarini et al. (2016).

It should be noted that calibration of a pixel-wise harmonic model (equation 4.4) and the subsequent modelling of a conditional flood probability (equation 4.11) corresponds to calibrating a seasonally and spatially dependant threshold classifier separately for each pixel.

### 4.2.3 Test case and validation approach

The approach was tested for a one-in-150-year flood event that took place in summer 2007 along the lower Rivers Severn and Avon and led to large-scale flooding in Worcestershire and Gloucestershire. On 22 July 2007, the River

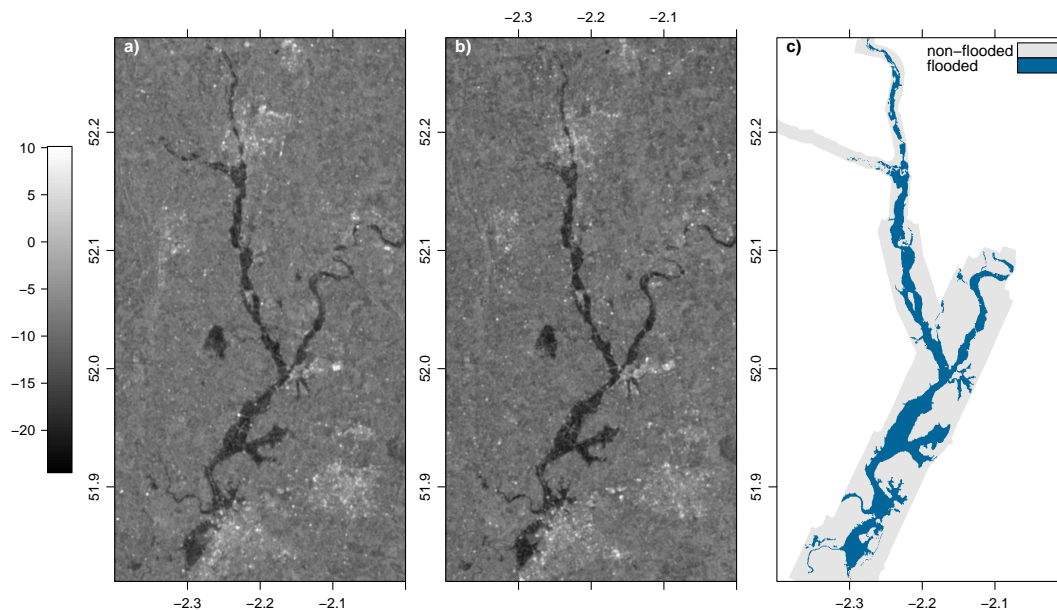


Figure 4.2: Calibrated ENVISAT ASAR WS scenes acquired over the River Severn on 23 July 2007 at (a) 10:27 and (b) 21:53. Units are dB. (c) Reference map derived from airborne imagery acquired on 24 July 2007 at 11:30.

Severn at Saxons Lode reached a peak water level of 5.9 m, exceeding the previous record level of 1947 (Marsh and Hannaford, 2007). Bankfull water levels were not reached again before 31 July (Mason et al., 2010). Several people in the region died during the floods, more than 100,000 homes were affected and, by December 2007, insurance claims amounted to around 3 billion pounds (Environment Agency, 2007). During the flood event, two ASAR scenes were acquired on 23 July 2007, at 10:27 and 21:53, which are shown in Figure 4.2(a) and Figure 4.2(b), respectively. In both images, large flooded areas are visible as dark objects along the rivers Severn and Avon.

A reference dataset that was manually delineated from airborne imagery acquired at a resolution of 0.2 m by the University of Reading (Mason et al., 2010) showing the flood extent in the morning of 24 July 2007 (at ca. 11:30) was available for validating the retrieved flood probability maps (Figure 4.2(c)). Details of the delineation procedure are given by Giustarini et al. (2013). This reference dataset has been used in a number of other studies (e.g. Giustarini et al., 2013, 2016; Mason et al., 2014) and, therefore, can be regarded as being well suited as a benchmark for validating SAR-based flood mapping approaches. The area surveyed by the airplane is located within the dashed rectangle in Figure 4.1.

Different methodologies exist for comparing probabilistic maps with bi-

nary reference datasets. One obvious approach is to convert the probabilistic map to a binary one as described before and then compute accuracy metrics based on the obtained contingency table. However, the total variability of uncertainty information would not be reflected by the result. Giustarini et al. (2016) adopted the reliability diagram (Wilks, 2011) for validating probabilistic flood extent retrievals from satellite data against binary reference observations. This technique had previously been used for, e.g. assessing the reliability of uncertain inundation models (Horritt, 2006). A reliability diagram consists of two plots, one showing the calibration function and the other one describing the distribution of  $p_F$  values. As a first step in deriving a reliability diagram, the flood probability values were binned into  $L = 10$  bins  $B_l \in \{0 \leq p_F < 0.1, 0.1 \leq p_F < 0.2, \dots, 0.9 \leq p_F \leq 1\}$ , with centres  $b_l = 0.05, 0.15, \dots, 0.95, l = 1, \dots, L$ . The calibration function consists of the probability of making a flood observation,  $o$ , within a given bin,  $B_l$ . This conditional probability,  $p(o|b_l)$ , was estimated by counting the number of reference flood pixels,  $n_{R,l}$ , located in each bin  $B_l$  divided by the total number of pixels in the reference map,  $n_R$ . The values derived for  $p(o|b_l)$  were then plotted against  $b_l$ . In a perfectly reliable flood probability map, the calibration function should coincide with the identity line. Shifts in the calibration function with respect to the identity line, on the other hand, point towards a biased probability map. Furthermore, reliability as a scalar measure for the quality of the calibration function is computed as the root mean squared vertical distances of the  $b_l$ - $p(o|b_l)$  point pairs to the identity line, weighted by  $n_{R,l}$  (Giustarini et al., 2016):

$$Rel = \sqrt{\frac{1}{n_R} \sum_{l=1}^L n_{R,l} [b_l - p(o|b_l)]^2}. \quad (4.12)$$

In a reliable map,  $Rel$  should be close to zero (Wilks, 2011). For the second part of the reliability diagram, the distribution of  $p_F$  values was derived by counting the relative frequencies of  $p_F$  values in each of the  $L$  bins and visualising them in form of a histogram. A flood probability map is called "confident" if a high percentage of pixels falls either in the very low or very high ranges of  $p_F$  and only a relatively small number in the intermediate bins (Wilks, 2011).

Since the reference map has a much higher resolution than the SAR WS images it is also possible to derive the fraction of each 75 m pixel that was covered by water according to the high-resolution imagery. As a result, it is feasible to visualise the spatial distribution of errors by mapping the differences between  $p_F$  and the flooded fraction  $f_F$  of a pixel. In most areas,  $p_F$  should be

comparable to  $f_F$ . In vegetated areas, on the other hand, where the microwave energy of the SAR antenna does not reach the water surface, or in urban areas,  $p_F$  can be expected to be smaller than the flooded fraction. Smaller  $p_F$  close to the centre of the inundated extent, on the other hand, may indicate that the water surface in the area has been roughened by waves.

## 4.3 Results and Discussion

In this section, first the retrieved parameters for classes  $F$  and  $nF$  are reported. Then, the retrieved flood probability maps are presented and the results of the validation are discussed.

### 4.3.1 Backscatter PDF for permanent water bodies and impact of $\theta_{\text{ref}}$

In order to parameterise the distribution function  $p(\varepsilon|F)$  backscatter values were extracted from the image stack for pixels that were known to be covered by water according to a reference permanent water layer (CLC 2006). The extracted  $\sigma^0$  values were then normalised with respect to the influence of local incidence angle  $\theta$  using equation 4.3. It was hypothesised that the choice of reference angle  $\theta_{\text{ref}}$  would impact the separability between land and water due to the higher values of  $|\beta|$  over permanent water reported in the literature (O’Grady et al., 2014). Indeed, steeper  $\beta$  gradients were found over permanent water than over land pixels. Two examples for a land and a water pixel are shown in Figure 4.3(a) and Figure 4.3(b), respectively. In general,  $\sigma^0$  decreases with higher local incidence angles. However, while for the land pixel, a change of  $\Delta\theta = 10^\circ$  corresponds to a change of  $\Delta\sigma^0 = -1.4$  dB, the difference amounts to  $\Delta\sigma^0 = -4.1$  dB for permanent water in this example. Similar findings have been reported by O’Grady et al. (2014) and Santoro et al. (2015). Therefore, normalisation to a higher  $\theta_{\text{ref}}$  is most likely to increase the separability between flooded and non-flooded pixels.

The histograms of  $\sigma^0$  from all permanent water pixels in the image stack after normalisation to  $30^\circ$  and  $40^\circ$  are shown in Figure 4.4(a) and Figure 4.4(b), respectively. Both histograms can be approximated by a normal distribution function due to the relatively high number of looks for ASAR WS data (Xie et al., 2002). As expected, the two PDFs differ mainly in their mean value, which is ca. 4 dB lower in the case of  $\sigma^0(40^\circ)$ . In both cases, variance is high as backscatter values measured under different wind conditions were included

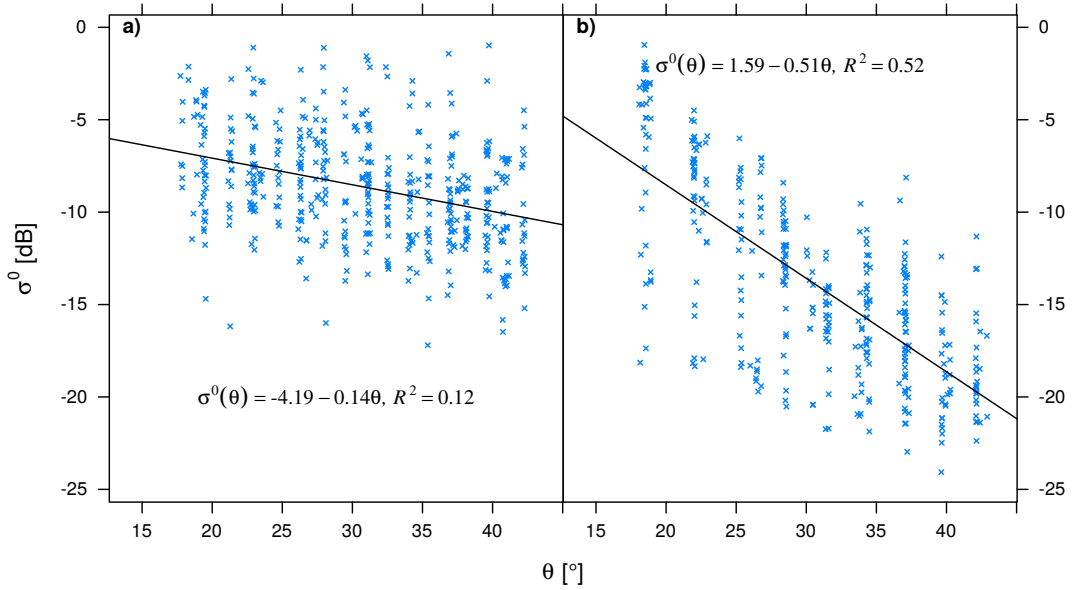


Figure 4.3: Relationship between  $\sigma^0$  and  $\theta$  for a pixel sampled over (a) land and (b) permanent water.

in the histograms. Wind-induced water surface roughness changes can significantly affect C-band  $\sigma^0$  from water bodies, especially in VV polarisation (Henry et al., 2006). Indeed, larger water bodies showed higher variance in  $\sigma^0$ , most likely due to their greater fetch. Nevertheless, the largest permanent water bodies were still smaller than the flooded area along the River Severn in July 2007 (*cf.* Figure 4.1). It should be noted that the PDFs were estimated based on an AOI that was larger than the one used for testing our approach. This was necessary due to the fact that no significant permanent water bodies were present in the test AOI. The PDF parameters, however, should be relatively stable for larger or smaller AOIs as they mainly depend on  $\theta_{\text{ref}}$ . Caution should be used if water bodies of much larger size are present where larger waves may occur but this was not the case here.

### 4.3.2 Backscatter PDF for land

For each pixel in the image stack, residuals  $\varepsilon_{nF}$  were computed from the harmonic model as described in Section 4.2.2. These residuals form a time series in which large outliers caused by flood events can be visually identified. An example of a residual time series for one pixel after normalisation to  $\theta_{\text{ref}} = 40^\circ$  is shown in Figure 4.5(a).  $\varepsilon_F$  values computed from the  $\sigma_F^0$  PDFs using equation 4.9 are shown in blue. The  $\varepsilon_{nF}$  time series shows no evident seasonality

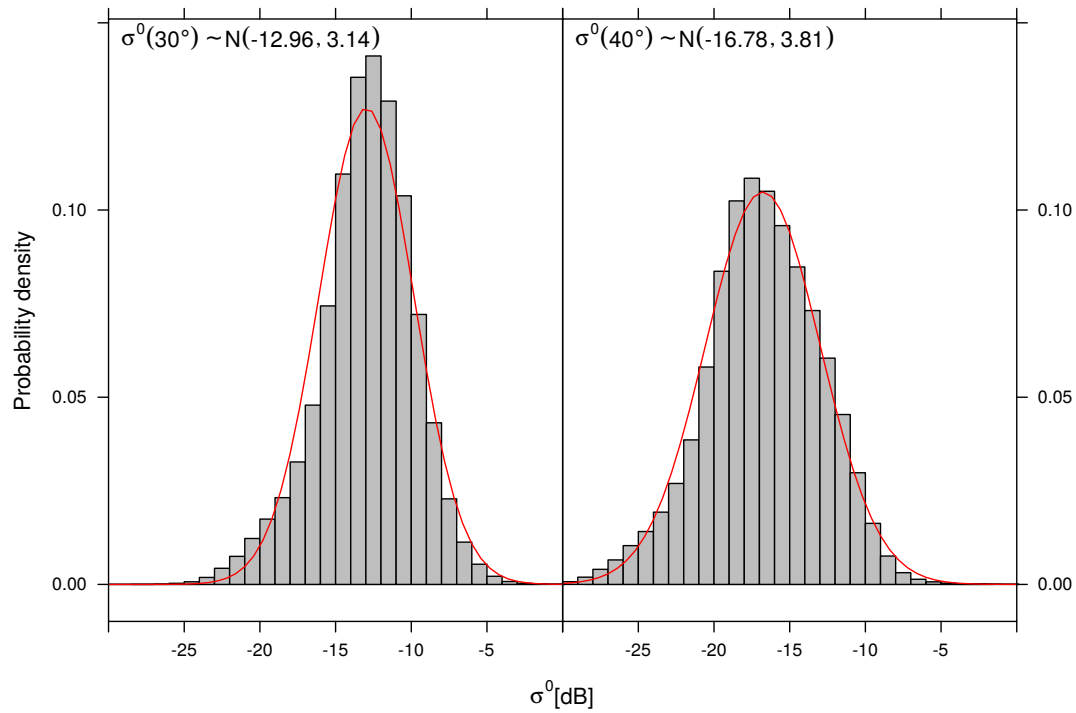


Figure 4.4: Histograms and estimated Gaussian probability density functions (given in terms of parameters  $m_F$ ,  $s_F$ ) of  $\sigma^0$  from permanent water bodies after normalisation to (a)  $30^\circ$  and (b)  $40^\circ$ . A total number of 5,089,307  $\sigma^0$  values was used for constructing the histograms.

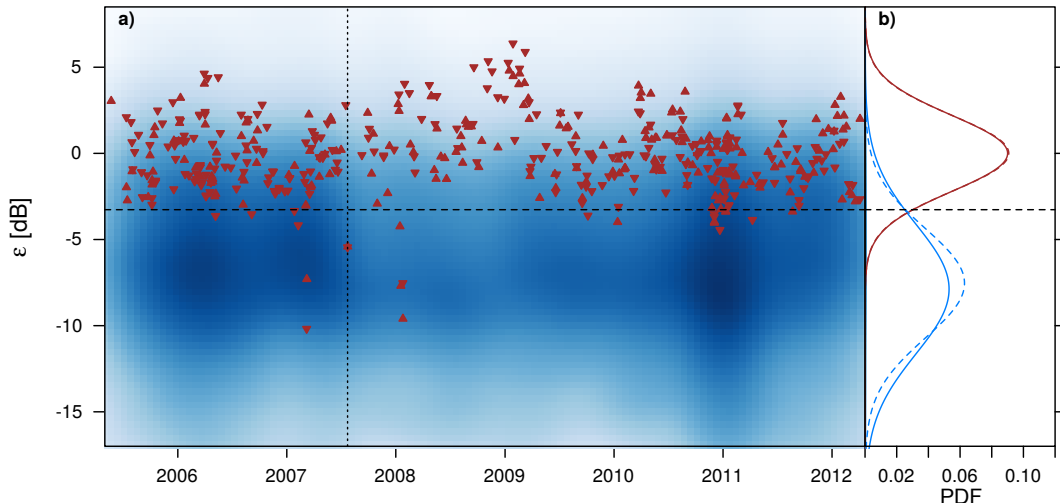


Figure 4.5: (a) Harmonic model residuals  $\varepsilon$  (brown) from ascending ( $\blacktriangle$ ) and descending ( $\blacktriangledown$ ) acquisitions for a single land pixel and centred samples from permanent water (blue); (b) corresponding density functions for ascending (solid) and descending (dashed) acquisitions. Bayes decision boundary ( $p_F = 0.5$ ) is given as black dashed horizontal line, the dotted vertical line marks 23 July 2007.  $\sigma^0$  was normalised to  $\theta_{\text{ref}} = 40^\circ$  before computation of  $\varepsilon$ .

after application of the harmonic model. In three occasions, March 2007, July 2007 and January 2008, large negative outliers with  $\varepsilon < -5$  dB are visible, which were already verified as having been caused by flood events by Schlaffer et al. (2015). The residuals are approximately normally distributed (Figure 4.5(b)) and usually lie above the Bayes decision boundary marking a flood probability  $p_F = 0.5$ . For the two flood images on 23 July 2007,  $\varepsilon$  is closer to  $m_{\varepsilon,F}$  than  $m_{\varepsilon,nF}$  (the latter equals zero) and, hence, high flood probabilities  $p_F$  can be expected. In this specific pixel, posterior probabilities  $p_F(t_1) = 0.93$  and  $p_F(t_2) = 0.91$  are obtained, where  $t_1$  denotes the time of acquisition in the morning and  $t_2$  in the evening.

It should be noted that the harmonic model parameters (equation 4.4) were estimated based on the entire time series, i.e. without excluding the flood observations as these are usually unknown *a priori*. For the Severn, it was, however, shown by Schlaffer et al. (2015) that removal of the flood images prior to model fitting only had a negligible effect on the parameter estimation. Nevertheless, in other areas where flood events occur more frequently, removing the flooded images could have a beneficial effect.

### 4.3.3 Flood probability maps

Flood probability maps computed using two different values of  $\theta_{\text{ref}}$  from two ASAR scenes acquired on 23 July 2007 (at 10:27 and 21:53) are shown in Figure 4.6. The flood probability maps were masked with the area that was surveyed by the overflight from which the reference flood map has been derived (*cf.* Figure 4.2(c)). In all cases, high probability values ( $p_F > 0.9$ ) can be observed in the centre of flooded areas where backscatter was already low in the original imagery (*cf.* Figure 4.2(a) and (b)). Around the borders of the flooded areas, intermediate values (in green colours) are visible indicating a higher uncertainty of the flood extent retrieval. Visual differences between flood extent in the morning and in the evening is rather small when looking at the entire test AOI.

There is, however, a notable difference between the flood probability maps computed using different values of  $\theta_{\text{ref}}$  for normalisation. For  $\theta_{\text{ref}} = 30^\circ$ , large non-flooded portions of both maps—morning and evening—show intermediate  $p_F$  values between 0.1 and 0.4 (Figure 4.6(c) and (d)). Exceptions to this behaviour can be found in urban areas. For  $\theta_{\text{ref}} = 40^\circ$ , however, this effect is much smaller and the flood probabilities of non-flooded pixels are mostly in the range 0.1–0.2 (Figure 4.6(a) and (b)). This supports our hypothesis that using a higher value of  $\theta_{\text{ref}}$  for normalisation increases the contrast between flooded and non-flooded areas and, therefore, also the separability between the two classes. This will be further explored by comparison with the high-resolution reference dataset in the following.

The reliability diagrams computed using the high-resolution reference map are shown in Figure 4.7. The diagrams indicate a high degree of agreement between the flood probability maps and the reference dataset in all four cases. For the morning image, the diagram (Figure 4.7(a)) shows a very high reliability of the obtained result as suggested by the calibration function following very closely the identity line. Use of  $\theta_{\text{ref}} = 40^\circ$  for normalisation led to a slight under-estimation for intermediate flood probability values as suggested by the point located above the identity line. When normalising to  $\theta_{\text{ref}} = 30^\circ$ , on the other hand, flood extent is overestimated, especially for values of  $p_F < 0.5$ , whereas the difference between  $\theta_{\text{ref}}$  is small at higher flood probabilities. This is also reflected in the higher *Rel* value that is obtained for  $\theta_{\text{ref}} = 30^\circ$  (Table 4.1). Figure 4.7(b) shows consistently higher errors in the flood probability map based on the ASAR scene acquired in the evening. The location of the  $b_l$ - $p(o|b_l)$  pairs suggests a high bias at low flood probabilities and a low bias at  $p_F > 0.3$ . As a consequence, higher *Rel* values of ca. 0.09, regardless of  $\theta_{\text{ref}}$ ,

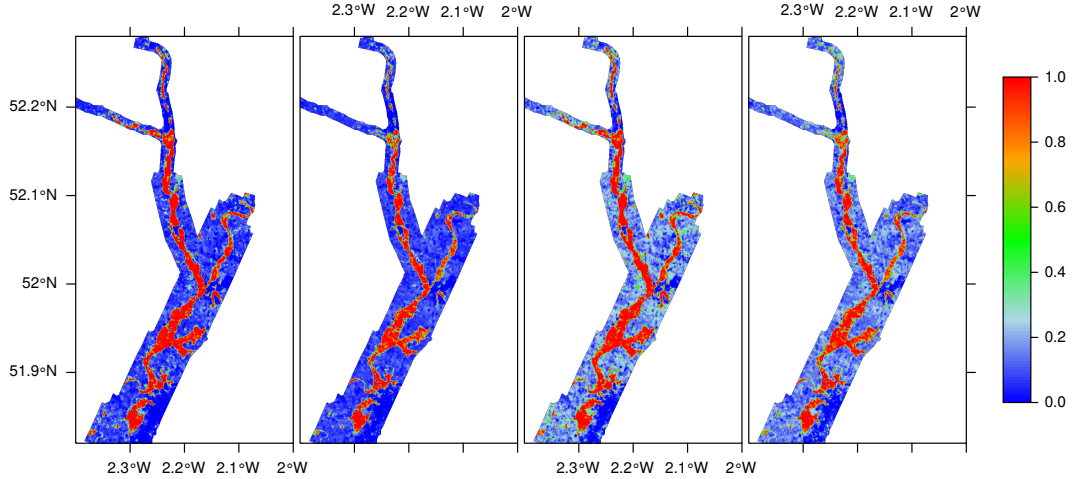


Figure 4.6: Flood probability maps for 23 July 2007 after normalisation to  $\theta_{\text{ref}} = 40^\circ$  at (a) 10:27 and (b) 21:53 and after normalisation to  $\theta_{\text{ref}} = 30^\circ$  at (c) 10:27 and (d) 21:53.

Table 4.1: *Rel* values obtained for the two ASAR scenes and different values of  $\theta_{\text{ref}}$ .

| $\theta_{\text{ref}}$ | Morning | Evening |
|-----------------------|---------|---------|
| $30^\circ$            | 0.107   | 0.095   |
| $40^\circ$            | 0.035   | 0.092   |

were obtained for the evening image (Table 4.1).

For both scenes, the histograms of  $p_F$  values further show relatively high confidence of the flood probability maps expressed by the fact that most pixels assume either very low ( $p_F < 0.2$ ) or very high ( $p_F > 0.9$ ) flood probability values whereas intermediate flood probabilities only contribute to a small proportion of the entire image. When normalising to  $\theta_{\text{ref}} = 30^\circ$ , more pixels are located in bin  $B_2$  (centred at  $b_2 = 0.15$ ) than in  $B_1$  (centred at  $b_1 = 0.05$ ) which is the reason for the fuzzy appearance of Figure 4.6(c) and (d). For  $\theta_{\text{ref}} = 40^\circ$ , a higher confidence of the flood probability maps is found as most  $p_F$  values are located in the first and last bins adding further support to the hypothesis that higher  $\theta_{\text{ref}}$  values lead to a better separability of flooded and non-flooded areas.

In addition to quantifying the performance of the flood probability maps using reliability diagrams, it can also be of benefit to visualise the spatial dis-

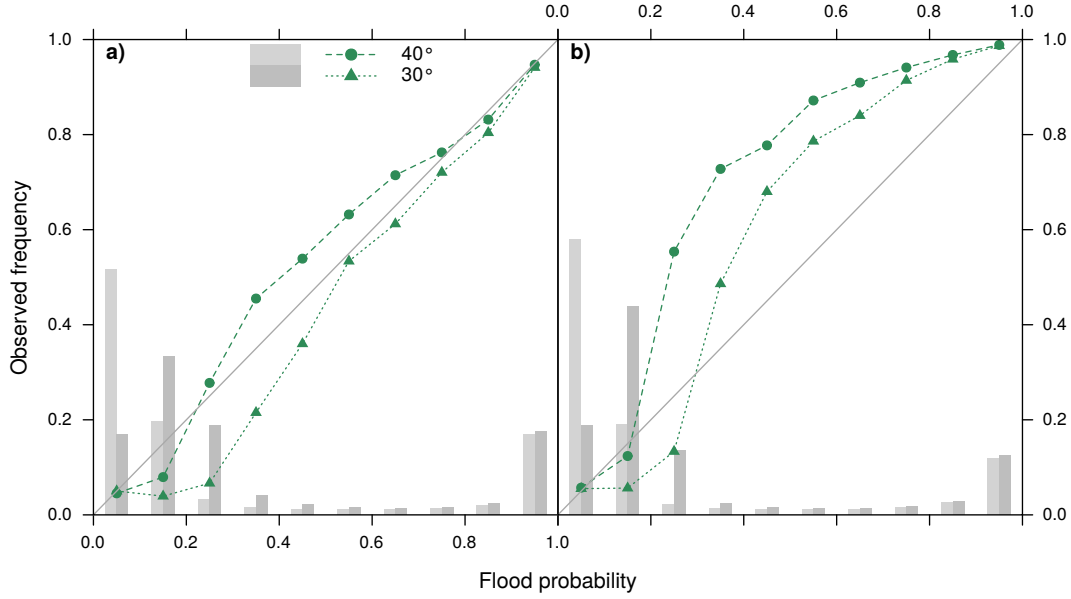


Figure 4.7: Reliability diagrams referring to flood probability maps for 23 July 2007 (a) morning and (b) evening.

tribution of errors in order to characterise areas in which a low performance of the flood maps is to be expected. Therefore, the bias computed as the differences between the retrieved  $p_F$  maps and the fraction of each 75-m pixel covered by the reference flood extent,  $f_F$ , is shown in Figure 4.8. Blue (red) indicates that the value of the probabilistic flood map is higher (lower) than the fraction of flooding derived from the polygons of the validation dataset. Most areas located in the centre of the flood extent show differences close to zero which may indicate that water surface roughness likely had a negligible effect on the quality of the SAR-derived maps. As expected, flooding is under-estimated (blue) close to urban areas such as Worcester, Tewkesbury and Gloucester and also along the edges of the flooded areas, most likely due to mixed pixels. Especially around Gloucester (labelled A in Figure 4.8), visual inspection of Google Earth imagery reveals buildings and woody vegetation leading to elevated  $\sigma^0$  values due to double-bounce and volume scattering and, therefore, low flood probabilities according to the proposed approach. For the image acquired in the evening along an ascending orbit, it can be seen that under-estimation especially occurs along the western shoreline, particularly after normalisation to  $\theta_{\text{ref}} = 40^\circ$  (Figure 4.8(b)). This may indicate a systematic error due to radar shadow induced by the rather steep slopes along the edges of the River Severn floodplain. Since radar shadow is recorded at all time steps within the ASAR time series it leads to lower  $\hat{\sigma}_{nF}^0$  and, therefore,

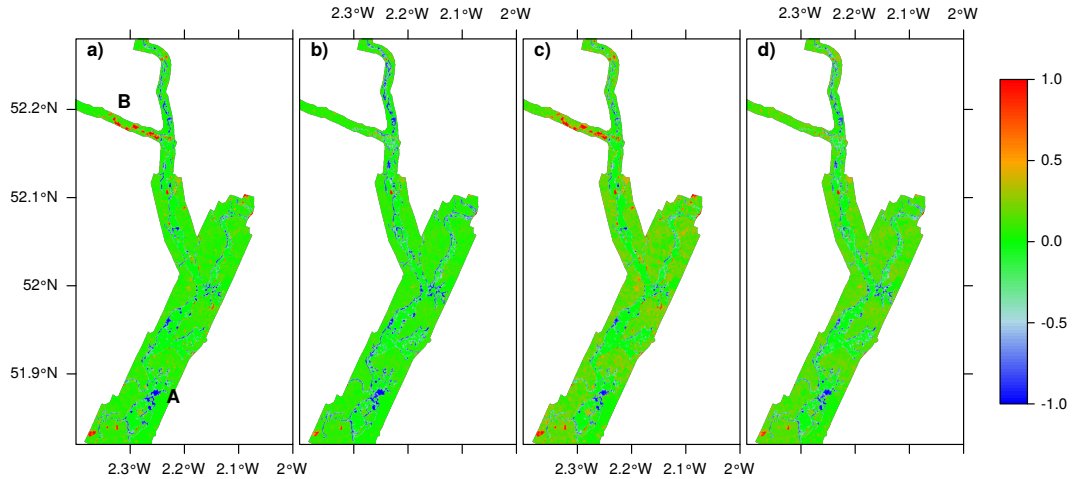


Figure 4.8: Differences between  $p_F$  and  $f_F$  in the reference map after normalisation to  $\theta_{\text{ref}} = 40^\circ$  at (a) 10:27 and (b) 21:53 and after normalisation to  $\theta_{\text{ref}} = 30^\circ$  at (c) 10:27 and (d) 21:53. Labels A and B label areas described in the text.

to lower  $\varepsilon$  and  $p_F$  values when a pixel is actually flooded. For the morning image, overestimation (red) is mainly visible along the River Teme (labelled B in Figure 4.8), a tributary of the Severn, in the northern part of the AOI (Figure 4.8(a) and (c)). This could be due to an actual recession of the flood in that area over the course of 23 July. The reference imagery was acquired roughly 24 hours after the first ASAR scene while the peak water level on the River Severn was already reached on 22 July (Zwenzner and Voigt, 2009).

## 4.4 Conclusions

A probabilistic change detection approach for flood mapping based on ENVISAT ASAR WS time series was proposed. The methodology consisted of a parameter estimation of conditional backscatter probability density functions for flooded and non-flooded classes and the subsequent computation of posterior probabilities. Seasonal variations in  $\sigma^0$  over land were accounted for using a harmonic model. Validation against a high-resolution reference dataset showed a high reliability of the retrieved flood probability maps. Deviations were mostly found along the edges of the floodplain due to mixed pixels, partially submerged buildings and vegetation and possibly radar shadows.

As ASAR WS imagery is characterised by a large swath width with large overlaps between tracks, scenes acquired from different viewing geometries were used when building the time series. Therefore,  $\sigma^0$  was normalised to a

common local incidence angle  $\theta_{\text{ref}}$ . Testing different choices for  $\theta_{\text{ref}}$  highlighted the importance of the choice of  $\theta_{\text{ref}}$  for the separability between flooded and non-flooded areas. In cases where flood probability was overestimated in non-flooded areas, this led to higher reliabilities of the derived flood probability maps.

As the time series are analysed separately for each pixel the mapping result does not depend on the relative size of the flood extent in comparison to the size of the scene which has been a problem for approaches which are based on single images. The proposed method, therefore, holds considerable potential for its inclusion in fully automatic processing chains targeted towards change detection in SAR time series, especially in connection with recent SAR missions such as Sentinel-1 which systematically acquire imagery at a high temporal sampling rate.

# Chapter 5

## Synthesis

### 5.1 Scientific impact

In the previous chapters, this thesis has addressed several open research questions in automatic flood mapping by introducing a novel change detection framework. The objectives of this thesis (*cf.* section 1.3) include the characterisation of backscatter signatures of different land-surface types using a harmonic model approach, the application of harmonic model estimates as pre-flood reference data in a change detection framework and, finally, the derivation of probabilistic flood maps.

In the following paragraphs, the main scientific contributions and key findings reported in this thesis are summarised. The major contribution of the thesis beyond the current state-of-the-art with respect to flood delineation from SAR data is the introduction of a framework for detecting changes in SAR image time series caused by flood events. For this purpose, the thesis has introduced a methodology for the estimation of land-surface backscatter signatures to be used as pre-flood reference based on harmonic analysis of SAR image time series. The main significance of the pixel-wise harmonic model estimate in this context is its role as a noise-free estimate of seasonal average  $\sigma^0$  at the respective location. In detail, the following advances are made:

**SAR time series analysis.** While in previous studies, time series analysis of SAR images mainly encompassed the extraction of descriptive statistics such as average backscatter or temporal variability, the presented approach explicitly addresses seasonality caused by hydrological and biophysical processes. This results in a better characterisation of backscatter behaviour in terms of its average amplitude and seasonality, that can be expected for a particular land-surface type. Furthermore, the information content of the harmonic

model coefficients is discussed in terms of hydrological processes occurring at the land surface. The potential of the model parameters for classifying a set of wetland types is explored. The effect of differences in local incidence angle on the derived parameters and its implications for the subsequent application in change detection are discussed. This holds additional relevance for the use of the approach for analysis of Sentinel-1 time series as imagery of most locations will be acquired at a single local incidence angle.

**Change detection.** A major difference of the change detection approach proposed in this thesis with respect to earlier work is that the need for selecting a reference image is eliminated as backscatter signatures of non-flooded land surfaces are estimated using a harmonic model. Furthermore, the impact of speckle in the produced change image is decreased as the harmonic model estimate of the pre-flood image represents an average of multiple SAR acquisitions and, therefore, does not contain a speckle contribution. As a result, comparison of the proposed approach with a traditional change detection between a pre- and a post-flood image have resulted in consistently higher user's and producer's accuracies, both in rural and urban areas. Finally, it is shown that, by analysing the full time series of model residuals, it is possible to identify flood images in an archive of historical SAR data.

**Probabilistic flood mapping.** The proposed approach makes three major contributions beyond the current state-of-the-art. First, probabilistic flood mapping approaches, with the exception of Westerhoff et al. (2013), typically estimate the necessary parameters based on the empirical histograms of one or few pre- and post-flood images. In the presented case, the PDFs are parameterised based on historical acquisitions and combined with a change detection approach. Second, the combination of pixel-wise harmonic model fitting with a probabilistic approach can be seen as equivalent to the estimation of an optimal, seasonally and spatially dependent threshold value for classifying flooded areas. Therefore, the threshold determination does not depend on the size of the flooded area with respect to the total area covered by the image. Finally, the thesis makes a contribution to the characterisation of uncertainties that arise in connection with SAR-based flood mapping by providing uncertain flood extent maps and discussing the differences compared to a high-resolution validation dataset.

## 5.2 Limitations

While the design of the presented study has permitted insight into the seasonality in backscattering behaviour found over land surfaces and the potential of such information for change detection, the proposed approach has a number of limitations which are explored in the following. Some of them have already been pointed out in the previous chapters and are summarised here. Three of the most important limitations are highlighted.

First, as already acknowledged in Chapter 3, the ASAR WS dataset used for estimating the harmonic model parameters included several images acquired during flood events. While it has been shown that, in the presented test case, the flood images exerted only a negligible influence on the estimated harmonic model parameters, this may not be true in areas which are flooded more frequently, especially in cases where seasonal flooding occurs. As demonstrated in Chapter 2, the harmonic model parameters can be used for mapping seasonally flooded areas due to the high sensitivity of ASAR backscatter to the occurrence of surface water. This implicates that the change detection approach presented in Chapters 3 and 4 would result in an under-estimation of the flood extent in seasonally flooded areas as the observed backscatter will be close to the harmonic model estimates. Instead, the approach, as it is presented here, would return the change in flood extent with respect to the period used for training the model parameters. While this may seem problematic at the first glance, it is not necessarily a shortcoming of the proposed approach since unexpected, non-periodic flood events hold much higher impact than seasonally recurring inundations. Moreover, the described characteristic holds interesting possibilities for application in wetland change detection which are explored in section 5.3.

Second, in Chapter 2, a technique for classifying seasonal open water and seasonally inundated vegetation has been presented. It has, however, not been examined whether the probabilistic change detection approach presented in Chapter 4 can be used, not only for mapping open flood water, but also flooding beneath vegetation which typically leads to double-bounce scattering. The proposed probabilistic method relies on backscatter PDFs for known water and non-water areas trained using ASAR time series. For double-bounce scattering, however, these areas are usually not known *a priori*, but could—potentially—be derived using the proposed approach. Nevertheless, the occurrence and contribution of double-bounce scattering to the total backscatter coefficient depends on a multitude of other factors such as water level, vegetation structure and density. These factors are very difficult to incorporate into a statistical

model such as the one presented in Chapter 4. An electromagnetic scattering model such as the one proposed by Pulvirenti et al. (2011a) could be applied but the required parameters are difficult to estimate at larger scales. Therefore, the presented change detection method is currently limited to the delineation of open flood water.

Finally, the pixel-wise estimation of a harmonic model leads to a higher computational cost in comparison to more traditional change detection methods in which the ratio or difference between a pre- and a post-flood image are computed. For near-real-time applications, however, it should be noted that optimising the harmonic model parameters from the full time series is usually not necessary. Instead, the model parameters could be estimated and stored in a parameter database which should be updated regularly, typically after completion of a full seasonal cycle. Flood imagery made available in near-real time could then be processed using the stored parameters with a much higher computational efficiency.

### 5.3 Perspectives

This thesis has focused on the analysis of data acquired by the ENVISAT mission, which ended in 2012. Nevertheless, the proposed methodology holds high relevance for other SAR missions, especially for the Sentinel-1 constellation whose two satellites were launched in 2014 and 2016 and which provides high-resolution imagery at a short revisit time of six days when combining data from both satellites (Torres et al., 2012). The proposed approach can be expected to greatly profit from the availability of high-resolution imagery with a consistent observation scenario and a high temporal revisit frequency. However, some modifications to the presented methodology are likely to be necessary. Due to the acquisition strategy of the Sentinel-1 mission every location on earth is imaged from a maximum number of three different orbits. In lower latitudes, imagery is acquired at only a single local incidence angle (Hornacek et al., 2012). This means that the normalisation with respect to local incidence angle applied to ASAR WS data in this study will not be necessary—or possible—in most cases for Sentinel-1. Nevertheless, further adaptations are likely to be required to the proposed approach in order to account for spatially varying local incidence angles. Moreover, the use of high-resolution data will pose new challenges. It is likely that speckle filtering will be required as the equivalent number of looks (ENL) of Sentinel-1 IW data at a resolution of  $20\text{ m} \times 22\text{ m}$  is estimated to be 4.4 while the ASAR WS medium-resolution

data are characterised by an  $ENL > 15$ . Alternatively, the moderate-resolution IW product (resolution  $88\text{ m} \times 87\text{ m}$ ) could be used due to its higher ENL of 81.8. This would also lower the computational cost of estimating harmonic model coefficients for each pixel in a multi-temporal image stack.

As has already been pointed out in the previous section, further open perspectives exist for the proposed approach in terms of harmonic model behaviour in seasonally flooded areas. Changes in this behaviour hold potential for detecting alterations in wetland extent with respect to a baseline period. For example, in Chapter 2, wetland types have been mapped based on data acquired between 2007 and 2008. If additional harmonic models can be trained using data from subsequent years, changes in the extent of different wetland types can be mapped. It must, however, be made sure that SAR acquisitions are available at approximately the same points along the seasonal cycle and that only full seasonal cycles are used for estimating the harmonic model parameters. This aim will also be easier achieved using Sentinel-1 data due to the higher consistency in acquisition planning.

Further open questions exist with respect to the estimation of other parameters of the presented framework, e.g. the prior probability of a pixel being flooded,  $p(F)$ . While in this and other studies (Giustarini et al., 2016; Westerhoff et al., 2013) a non-informative prior has been used, other authors have pointed out the possibility of estimating the prior based on topographical information (e.g. Refice et al., 2014). The HAND index applied here for masking is a candidate for deriving such probabilities. However, the estimation of prior probabilities in an objective manner without parameterising them based on hydraulic model results is not a straightforward task.

Finally, approaches such as the one presented in this thesis may help to represent information contained in image time series using only a small number of parameters. Such novel representation methods have recently been called for by Amitrano et al. (2016) and could help to condense the information in image repositories which will be increasingly available in the future.



# Bibliography

- Aires, F., Papa, F., and Prigent, C., 2013. A Long-Term, High-Resolution Wetland Dataset over the Amazon Basin, Downscaled from a Multiwavelength Retrieval Using SAR Data. *Journal of Hydrometeorology*, 14(2):594–607. doi:10.1175/JHM-D-12-093.1.
- Albergel, C., Dorigo, W., Reichle, R. H., Balsamo, G., de Rosnay, P., Muñoz-Sabater, J., Isaksen, L., de Jeu, R., and Wagner, W., 2013. Skill and Global Trend Analysis of Soil Moisture from Reanalyses and Microwave Remote Sensing. *Journal of Hydrometeorology*, 14(4):1259–1277. doi:10.1175/JHM-D-12-0161.1.
- Amitrano, D., Cecinati, F., Martino, G. D., Iodice, A., Mathieu, P.-P., Riccio, D., and Ruello, G., 2016. Multitemporal Level-1b Products: Definitions, Interpretation, and Applications. *IEEE Transactions on Geoscience and Remote Sensing*, 54(11):6545–6562. doi:10.1109/TGRS.2016.2586189.
- Antonova, S., Kääb, A., Heim, B., Langer, M., and Boike, J., 2016. Spatio-temporal variability of X-band radar backscatter and coherence over the Lena River Delta, Siberia. *Remote Sensing of Environment*, 182:169–191. doi:10.1016/j.rse.2016.05.003.
- Attema, E. P. W. and Ulaby, F. T., 1978. Vegetation modeled as a water cloud. *Radio Science*, 13(2):357–364. doi:10.1029/RS013i002p00357.
- Balsamo, G., Albergel, C., Beljaars, A., Boussetta, S., Brun, E., Cloke, H., Dee, D., Dutra, E., Muñoz-Sabater, J., Pappenberger, F., de Rosnay, P., Stockdale, T., and Vitart, F., 2015. ERA-Interim/Land: a global land surface reanalysis data set. *Hydrology and Earth System Sciences*, 19(1): 389–407. doi:10.5194/hess-19-389-2015.
- Bartalis, Z., Scipal, K., and Wagner, W., 2006. Azimuthal anisotropy of scatterometer measurements over land. *IEEE Transactions on Geoscience and Remote Sensing*, 44(8):2083–2092. doi:10.1109/TGRS.2006.872084.

- Bartsch, A., Pathe, C., Wagner, W., and Scipal, K., 2008. Detection of permanent open water surfaces in central Siberia with ENVISAT ASAR wide swath data with special emphasis on the estimation of methane fluxes from tundra wetlands. *Hydrology Research*, 39(2):89–100. doi:10.2166/nh.2008.041.
- Bartsch, A., Balzter, H., and George, C., 2009. The influence of regional surface soil moisture anomalies on forest fires in Siberia observed from satellites. *Environmental Research Letters*, 4(4):45021. doi:10.1088/1748-9326/4/4/045021.
- Bartsch, A., Trofaier, A. M., Hayman, G., Sabel, D., Schlaffer, S., Clark, D. B., and Blyth, E., 2012. Detection of open water dynamics with ENVISAT ASAR in support of land surface modelling at high latitudes. *Biogeosciences*, 9(2):703–714. doi:10.5194/bg-9-703-2012.
- Birkett, C. M., 2000. Synergistic Remote Sensing of Lake Chad Variability of Basin Inundation. *Remote Sensing of Environment*, 72(2):218–236. doi:10.1016/S0034-4257(99)00105-4.
- Blaes, X., Holecz, F., van Leeuwen, H. J. C., and Defourny, P., 2007. Regional crop monitoring and discrimination based on simulated ENVISAT ASAR wide swath mode images. *International Journal of Remote Sensing*, 28(2):371–393. doi:10.1080/01431160600735608.
- Bloomfield, P., 2000. *Fourier Analysis of Time Series - An Introduction*. John Wiley & Sons Inc., New York, 2nd edition. ISBN 0-471-88948-2.
- Bontemps, S., Boettcher, M., Brockmann, C., Kirches, G., Lamarche, C., Radoux, J., Santoro, M., Vanbogaert, E., Wegmüller, U., Herold, M., Achard, F., Ramoino, F., Arino, O., and Defourny, P., 2015. Multi-year global land cover mapping at 300 m and characterization for climate modelling: achievements of the Land Cover component of the ESA Climate Change Initiative. In *ISPRS - International Archives of the Photogrammetry, Remote Sensing and Spatial Information Sciences*, volume XL-7/W3, pages 323–328. International Society for Photogrammetry and Remote Sensing. doi:10.5194/isprsarchives-XL-7-W3-323-2015.
- Brooks, E. B., Thomas, V. A., Wynne, R. H., and Coulston, J. W., 2012. Fitting the multitemporal curve: A fourier series approach to the missing data problem in remote sensing analysis. *IEEE Transactions on Geoscience and Remote Sensing*, 50(9):3340–3353. doi:10.1109/TGRS.2012.2183137.

- Bruzzone, L. and Fernández-Prieto, D., 2000. Automatic analysis of the difference image for unsupervised change detection. *IEEE Transactions on Geoscience and Remote Sensing*, 38(3):1171–1182. doi:10.1109/36.843009.
- Bruzzone, L., Marconcini, M., Wegmüller, U., and Wiesmann, A., 2004. An advanced system for the automatic classification of multitemporal SAR images. *IEEE Transactions on Geoscience and Remote Sensing*, 42(6):1321–1334. doi:10.1109/TGRS.2004.826821.
- Büttner, G., Kosztra, B., Maucha, G., and Pataki, R., 2010. Implementation and achievements of CLC 2006. Technical report, European Environment Agency. URL <http://www.eea.europa.eu/data-and-maps/data/corine-land-cover-2006-raster-2>.
- Chini, M., Piscini, A., Cinti, F. R., Amici, S., Nappi, R., and DeMartini, P. M., 2013. The 2011 Tohoku (Japan) Tsunami Inundation and Liquefaction Investigated Through Optical, Thermal, and SAR Data. *IEEE Geoscience and Remote Sensing Letters*, 10(2):347–351. doi:10.1109/LGRS.2012.2205661.
- Chini, M., Giustarini, L., Hostache, R., and Matgen, P., 2016. An automatic SAR-based flood mapping algorithm combining hierarchical tiling and change detection. In *ESA Living Planet, 6-13 May 2016*, Prague, Czech Republic.
- Cihlar, J., Pultz, T. J., and Gray, A. L., 1992. Change detection with synthetic aperture radar. *International Journal of Remote Sensing*, 13(3):401–414. doi:10.1080/01431169208904045.
- Cohen, J., Riihimäki, H., Pulliainen, J., Lemmetyinen, J., and Heilimo, J., 2016. Implications of boreal forest stand characteristics for X-band SAR flood mapping accuracy. *Remote Sensing of Environment*, 186:47–63. doi:10.1016/j.rse.2016.08.016.
- Covello, F., Battazza, F., Coletta, A., Lopinto, E., Fiorentino, C., Pietranera, L., Valentini, G., and Zoffoli, S., 2010. COSMO-SkyMed an existing opportunity for observing the Earth. *Journal of Geodynamics*, 49(3-4):171–180. doi:10.1016/j.jog.2010.01.001.
- Crétaux, J.-F., Jelinski, W., Calmant, S., Kouraev, A., Vuglinski, V., Bergé-Nguyen, M., Gennero, M.-C., Nino, F., Abarca Del Rio, R., Cazenave, A., and Maisongrande, P., 2011. SOLS: A lake database to monitor in the Near Real Time water level and storage variations from remote sensing data. *Advances in Space Research*, 47(9):1497–1507. doi:10.1016/j.asr.2011.01.004.

- Cumming, I. G. and Wong, F. H., 2004. *Digital Processing of Synthetic Aperture Radar Data: Algorithms and Implementation*. Artech House.
- D'Addabbo, A., Refice, A., Pasquariello, G., Lovergine, F. P., Capolongo, D., and Manfreda, S., 2016. A Bayesian Network for Flood Detection Combining SAR Imagery and Ancillary Data. *IEEE Transactions on Geoscience and Remote Sensing*, 54(6):3612–3625. doi:10.1109/TGRS.2016.2520487.
- Danklmayer, A., Doring, B., Schwerdt, M., and Chandra, M., 2009. Assessment of Atmospheric Propagation Effects in SAR Images. *IEEE Transactions on Geoscience and Remote Sensing*, 47(10):3507–3518. doi:10.1109/TGRS.2009.2022271.
- Dekker, R. J., 1998. Speckle filtering in satellite SAR change detection imagery. *International Journal of Remote Sensing*, 19(6):1133–1146. doi:10.1080/014311698215649.
- Dellepiane, S. G. and Angiati, E., 2012. A New Method for Cross-Normalization and Multitemporal Visualization of SAR Images for the Detection of Flooded Areas. *IEEE Transactions on Geoscience and Remote Sensing*, 50(7):2765–2779. doi:10.1109/TGRS.2011.2174999.
- Desnos, Y.-L., Buck, C., Guijarro, J., Levrini, G., Suchail, J.-L., Torres, R., Laur, H., Closa, J., and Rosich, B., 2000. The ENVISAT Advanced Synthetic Aperture Radar System. *IEEE International Geoscience and Remote Sensing Symposium*, 3(39):1171–1173. doi:10.1109/IGARSS.2000.858057.
- Di Baldassarre, G., Schumann, G., and Bates, P. D., 2009. A technique for the calibration of hydraulic models using uncertain satellite observations of flood extent. *Journal of Hydrology*, 367(3-4):276–282. doi:10.1016/j.jhydrol.2009.01.020.
- Di Baldassarre, G., Schumann, G., Brandimarte, L., and Bates, P., 2011. Timely Low Resolution SAR Imagery To Support Floodplain Modelling: a Case Study Review. *Surveys in Geophysics*, 32(3):255–269. doi:10.1007/s10712-011-9111-9.
- Dostálová, A., Doubková, M., Sabel, D., Bauer-Marschallinger, B., and Wagner, W., 2014. Seven Years of Advanced Synthetic Aperture Radar (ASAR) Global Monitoring (GM) of Surface Soil Moisture over Africa. *Remote Sensing*, 6(8):7683–7707. doi:10.3390/rs6087683.

- Duda, R. O., Hart, P. E., and Stork, D. G., 2001. *Pattern Classification*. John Wiley & Sons, Inc., New York, NY, 2nd edition. ISBN 978-0471056690.
- Eastman, J. R., Sangermano, F., Ghimire, B., Zhu, H., Chen, H., Neeti, N., Cai, Y., Machado, E. A., and Crema, S. C., 2009. Seasonal trend analysis of image time series. *International Journal of Remote Sensing*, 30(February 2015):2721–2726. doi:10.1080/01431160902755338.
- Ellenbroek, G. A., 1987. *Ecology and productivity of an African wetland system*. Springer Netherlands, Dordrecht. ISBN 978-94-010-8298-3. doi:10.1007/978-94-009-4051-2.
- Environment Agency, 2007. Review of 2007 summer floods. Technical report, Environment Agency. URL [https://www.gov.uk/government/uploads/system/uploads/attachment\\_data/file/292924/geho1107bnmi-e-e.pdf](https://www.gov.uk/government/uploads/system/uploads/attachment_data/file/292924/geho1107bnmi-e-e.pdf).
- ESA, 2008. ENVISAT-1 Products Specifications Volume 9: DORIS Product Specifications. Technical Report Rev. B, ESA, Document reference: PO-RS-MDA-GS-2009. URL [https://earth.esa.int/c/document\\_library/get\\_file?folderId=13020&name=DLFE-632.pdf](https://earth.esa.int/c/document_library/get_file?folderId=13020&name=DLFE-632.pdf).
- ESA, 2012. ENVISAT-1 Products Specifications Volume 8: ASAR Products Specifications. Technical Report Rev. C, ESA, Document reference: PO-RS-MDA-GS-2009. URL [https://earth.esa.int/c/document\\_library/get\\_file?folderId=231342&name=DLFE-2136.pdf](https://earth.esa.int/c/document_library/get_file?folderId=231342&name=DLFE-2136.pdf).
- Evans, J. P. and Geerken, R., 2006. Classifying rangeland vegetation type and coverage using a Fourier component based similarity measure. *Remote Sensing of Environment*, 105:1–8. doi:10.1016/j.rse.2006.05.017.
- Fluet-Chouinard, E., Lehner, B., Rebelo, L.-M., Papa, F., and Hamilton, S. K., 2015. Development of a global inundation map at high spatial resolution from topographic downscaling of coarse-scale remote sensing data. *Remote Sensing of Environment*, 158:348–361. doi:10.1016/j.rse.2014.10.015.
- Förste, C., Bruinsma, S., Flechtner, F., Marty, J., Lemoine, J., Dahle, C., Abrikosov, O., Neumayer, H., Biancale, R., Barthelmes, F., and Balmino, G., 2012. A new release of EIGEN-6C. In *AGU Fall Meeting 2012*, San Francisco, USA.
- Frey, D., Butenuth, M., and Straub, D., 2012. Probabilistic graphical models for flood state detection of roads combining imagery and

- DEM. *IEEE Geoscience and Remote Sensing Letters*, 9(6):1051–1055. doi:10.1109/LGRS.2012.2188881.
- García-Pintado, J., Neal, J. C., Mason, D. C., Dance, S. L., and Bates, P. D., 2013. Scheduling satellite-based SAR acquisition for sequential assimilation of water level observations into flood modelling. *Journal of Hydrology*, 495: 252–266. doi:10.1016/j.jhydrol.2013.03.050.
- Giustarini, L., Matgen, P., Hostache, R., Montanari, M., Plaza, D., Pauwels, V. R. N., De Lannoy, G. J. M., De Keyser, R., Pfister, L., Hoffmann, L., and Savenije, H. H. G., 2011. Assimilating SAR-derived water level data into a hydraulic model: a case study. *Hydrology and Earth System Sciences*, 15(7):2349–2365. doi:10.5194/hess-15-2349-2011.
- Giustarini, L., Hostache, R., Matgen, P., Schumann, G. J.-P., Bates, P. D., and Mason, D. C., 2013. A Change Detection Approach to Flood Mapping in Urban Areas Using TerraSAR-X. *IEEE Transactions on Geoscience and Remote Sensing*, 51(4):2417–2430. doi:10.1109/TGRS.2012.2210901.
- Giustarini, L., Vernieuwe, H., Verwaeren, J., Chini, M., Hostache, R., Matgen, P., Verhoest, N., and De Baets, B., 2015. Accounting for image uncertainty in SAR-based flood mapping. *International Journal of Applied Earth Observation and Geoinformation*, 34:70–77. doi:10.1016/j.jag.2014.06.017.
- Giustarini, L., Hostache, R., Kavetski, D., Chini, M., Corato, G., Schlaffer, S., and Matgen, P., 2016. Probabilistic Flood Mapping Using Synthetic Aperture Radar Data. *IEEE Transactions on Geoscience and Remote Sensing*, 54(12):6958–6969. doi:10.1109/TGRS.2016.2592951.
- Grimaldi, S., Li, Y., Pauwels, V. R. N., and Walker, J. P., 2016. Remote Sensing-Derived Water Extent and Level to Constrain Hydraulic Flood Forecasting Models: Opportunities and Challenges. *Surveys in Geophysics*, 37(5):977–1034. doi:10.1007/s10712-016-9378-y.
- Henderson, F. M. and Lewis, A. J., 2008. Radar detection of wetland ecosystems: a review. *International Journal of Remote Sensing*, 29(20):5809–5835. doi:10.1080/01431160801958405.
- Henry, J.-B., Chastanet, P., Fellah, K., and Desnos, Y.-L., 2003. ENVISAT multipolarised ASAR data for flood mapping. In *Proceedings of IGARSS 2003*, volume 2, pages 1136–1138. IEEE. ISBN 0-7803-7929-2. doi:10.1109/IGARSS.2003.1294036.

- Henry, J.-B., Chastanet, P., Fellah, K., and Desnos, Y.-L., 2006. Envisat multi-polarized ASAR data for flood mapping. *International Journal of Remote Sensing*, 27(10):1921–1929. doi:10.1080/01431160500486724.
- Hess, L. L., Melack, J. M., Novo, E. M. L. M., Barbosa, C. C. F., and Gastil, M., 2003. Dual-season mapping of wetland inundation and vegetation for the central Amazon basin. *Remote Sensing of Environment*, 87(4):404–428. doi:10.1016/j.rse.2003.04.001.
- Hijmans, R. J., Cameron, S. E., Parra, J. L., Jones, P. G., and Jarvis, A., 2005. Very high resolution interpolated climate surfaces for global land areas. *International Journal of Climatology*, 25(15):1965–1978. doi:10.1002/joc.1276.
- Hornacek, M., Wagner, W., Sabel, D., Truong, H.-l., Snoeij, P., Hahmann, T., Diedrich, E., and Doubkova, M., 2012. Potential for High Resolution Systematic Global Surface Soil Moisture Retrieval via Change Detection using Sentinel-1. *IEEE Journal of Selected Topics in Applied Earth Observations and Remote Sensing*, 5(4):1303–1311. doi:10.1109/JSTARS.2012.2190136.
- Horritt, M. S., 1999. A statistical active contour model for SAR image segmentation. *Image and Vision Computing*, 17(3-4):213–224. doi:10.1016/S0262-8856(98)00101-2.
- Horritt, M. S., 2006. A methodology for the validation of uncertain flood inundation models. *Journal of Hydrology*, 326(1-4):153–165. doi:10.1016/j.jhydrol.2005.10.027.
- Horritt, M. S., Mason, D. C., and Luckman, A. J., 2001. Flood boundary delineation from Synthetic Aperture Radar imagery using a statistical active contour model. *International Journal of Remote Sensing*, 22:2489–2507. doi:10.1080/01431160152497691.
- Hostache, R., Matgen, P., and Wagner, W., 2012. Change detection approaches for flood extent mapping: How to select the most adequate reference image from online archives? *International Journal of Applied Earth Observation and Geoinformation*, 19:205–213. doi:10.1016/j.jag.2012.05.003.
- Jarvis, A., Reuter, H., Nelson, A., and Guevara, E., 2008. Hole-filled seamless SRTM data V4. URL <http://srtm.csi.cgiar.org>.
- Jongman, B., Ward, P. J., and Aerts, J. C., 2012. Global exposure to river and coastal flooding: Long term trends and changes. *Global Environmental Change*, 22(4):823–835. doi:10.1016/j.gloenvcha.2012.07.004.

- Jonsson, P. and Eklundh, L., 2002. Seasonality extraction by function fitting to time-series of satellite sensor data. *IEEE Transactions on Geoscience and Remote Sensing*, 40(8):1824–1832. doi:10.1109/TGRS.2002.802519.
- Junk, W. J., An, S., Finlayson, C. M., Gopal, B., Květ, J., Mitchell, S. A., Mitsch, W. J., and Robarts, R. D., 2012. Current state of knowledge regarding the world’s wetlands and their future under global climate change: a synthesis. *Aquatic Sciences*, 75(1):151–167. doi:10.1007/s00027-012-0278-z.
- Kasischke, E. S. and Bourgeau-Chavez, L. L., 1997. Monitoring South Florida wetlands using ERS-1 SAR imagery. *Photogrammetric Engineering & Remote Sensing*, 63(3):281–291.
- Kasischke, E. S., Smith, K. B., Bourgeau-Chavez, L. L., Romanowicz, E. A., Brunzell, S., and Richardson, C. J., 2003. Effects of seasonal hydrologic patterns in south Florida wetlands on radar backscatter measured from ERS-2 SAR imagery. *Remote Sensing of Environment*, 88(4):423–441. doi:10.1016/j.rse.2003.08.016.
- Kasischke, E. S., Bourgeau-Chavez, L. L., Rober, A. R., Wyatt, K. H., Waddington, J. M., and Turetsky, M. R., 2009. Effects of soil moisture and water depth on ERS SAR backscatter measurements from an Alaskan wetland complex. *Remote Sensing of Environment*, 113(9):1868–1873. doi:10.1016/j.rse.2009.04.006.
- Kaufman, L. and Rousseeuw, P., 1990. *Finding Groups in Data*. Wiley Series in Probability and Statistics. John Wiley & Sons, Inc., Hoboken, NJ, USA. ISBN 9780470316801. doi:10.1002/9780470316801.
- Kaufman, Y. J. and Remer, L. A., 1994. Detection of forests using mid-IR reflectance: an application for aerosol studies. *IEEE Transactions on Geoscience and Remote Sensing*, 32(3):672–683. doi:10.1109/36.297984.
- Kim, J.-W., Lu, Z., Jones, J. W., Shum, C., Lee, H., and Jia, Y., 2014. Monitoring Everglades freshwater marsh water level using L-band synthetic aperture radar backscatter. *Remote Sensing of Environment*, 150:66–81. doi:10.1016/j.rse.2014.03.031.
- Klemas, V., 2013. Remote sensing of emergent and submerged wetlands: an overview. *International Journal of Remote Sensing*, 34(18):6286–6320. doi:10.1080/01431161.2013.800656.

- Kornelsen, K. C. and Coulibaly, P., 2013. Advances in Soil Moisture Retrieval from Synthetic Aperture Radar and Hydrological Applications. *Journal of Hydrology*, 476:460–489. doi:10.1016/j.jhydrol.2012.10.044.
- Kuenzer, C., Guo, H., Huth, J., Leinenkugel, P., Li, X., and Dech, S., 2013a. Flood Mapping and Flood Dynamics of the Mekong Delta: ENVISAT-ASAR-WSM Based Time Series Analyses. *Remote Sensing*, 5(2):687–715. doi:10.3390/rs5020687.
- Kuenzer, C., Guo, H., Schlegel, I., Tuan, V., Li, X., and Dech, S., 2013b. Varying Scale and Capability of Envisat ASAR-WSM, TerraSAR-X Scansar and TerraSAR-X Stripmap Data to Assess Urban Flood Situations: A Case Study of the Mekong Delta in Can Tho Province. *Remote Sensing*, 5(10):5122–5142. doi:10.3390/rs5105122.
- Lang, M., Townsend, P., and Kasischke, E., 2008. Influence of incidence angle on detecting flooded forests using C-HH synthetic aperture radar data. *Remote Sensing of Environment*, 112(10):3898–3907. doi:10.1016/j.rse.2008.06.013.
- Lee, H., Yuan, T., Jung, H. C., and Beighley, E., 2015. Mapping wetland water depths over the central Congo Basin using PALSAR ScanSAR, Envisat altimetry, and MODIS VCF data. *Remote Sensing of Environment*, 159:70–79. doi:10.1016/j.rse.2014.11.030.
- Lee, J., 1983. A simple speckle smoothing algorithm for synthetic aperture radar images. *IEEE Transactions on Systems, Man and Cybernetics*, 13(1):85–89. doi:10.1109/TSMC.1983.6313036.
- Lehner, B., Verdin, K., and Jarvis, A., 2008. New global hydrography derived from spaceborne elevation data. *Eos Transactions AGU*, 89(10):93–94. doi:10.1029/2008EO100001.
- Lhermitte, S., Verbesselt, J., Jonckheere, I., Nackaerts, K., van Aardt, J. A. N., Verstraeten, W. W., and Coppin, P., 2008. Hierarchical image segmentation based on similarity of NDVI time series. *Remote Sensing of Environment*, 112:506–521. doi:10.1016/j.rse.2007.05.018.
- Long, S., Fatoyinbo, T. E., and Policelli, F., 2014. Flood extent mapping for Namibia using change detection and thresholding with SAR. *Environmental Research Letters*, 9(3):035002. doi:10.1088/1748-9326/9/3/035002.

- Lopes, A., Nezry, E., Touzi, R., and Laur, H., 1993. Structure detection and statistical adaptive speckle filtering in SAR images. *International Journal of Remote Sensing*, 14(9):1735–1758. doi:10.1080/01431169308953999.
- Lu, D., Mausel, P., Brondízio, E., and Moran, E., 2004. Change detection techniques. *International Journal of Remote Sensing*, 25(12):2365–2407. doi:10.1080/0143116031000139863.
- Marsh, T. and Hannaford, J., 2007. The summer 2007 floods in England and Wales – a hydrological appraisal. Technical report, Centre for Ecology & Hydrology, Wallingford, UK. URL [http://www.ceh.ac.uk/sites/default/files/ceh\\_floodingappraisal.pdf](http://www.ceh.ac.uk/sites/default/files/ceh_floodingappraisal.pdf).
- Martinis, S. and Rieke, C., 2015. Backscatter Analysis Using Multi-Temporal and Multi-Frequency SAR Data in the Context of Flood Mapping at River Saale, Germany. *Remote Sensing*, 7(6):7732–7752. doi:10.3390/rs70607732.
- Martinis, S. and Twele, A., 2010. A hierarchical spatio-temporal Markov model for improved flood mapping using multi-temporal X-band SAR data. *Remote Sensing*, 2(9):2240–2258. doi:10.3390/rs2092240.
- Martinis, S., Twele, A., and Voigt, S., 2009. Towards operational near real-time flood detection using a split-based automatic thresholding procedure on high resolution TerraSAR-X data. *Natural Hazards and Earth System Science*, 9(2):303–314. doi:10.5194/nhess-9-303-2009.
- Martinis, S., Twele, A., and Voigt, S., 2011. Unsupervised Extraction of Flood-Induced Backscatter Changes in SAR Data Using Markov Image Modeling on Irregular Graphs. *IEEE Transactions on Geoscience and Remote Sensing*, 49(1):251–263. doi:10.1109/TGRS.2010.2052816.
- Martinis, S., Kersten, J., and Twele, A., 2015. A fully automated TerraSAR-X based flood service. *ISPRS Journal of Photogrammetry and Remote Sensing*, 104:203–212. doi:10.1016/j.isprsjprs.2014.07.014.
- Mason, D., Speck, R., Devereux, B., Schumann, G.-P., Neal, J., and Bates, P., 2010. Flood Detection in Urban Areas Using TerraSAR-X. *IEEE Transactions on Geoscience and Remote Sensing*, 48(2):882–894. doi:10.1109/TGRS.2009.2029236.
- Mason, D. C., Davenport, I. J., Neal, J. C., Schumann, G. J.-P., and Bates, P. D., 2012. Near Real-Time Flood Detection in Urban and

- Rural Areas Using High-Resolution Synthetic Aperture Radar Images. *IEEE Transactions on Geoscience and Remote Sensing*, 50(8):3041–3052. doi:10.1109/TGRS.2011.2178030.
- Mason, D. C., Giustarini, L., Garcia-Pintado, J., and Cloke, H., 2014. Detection of flooded urban areas in high resolution Synthetic Aperture Radar images using double scattering. *International Journal of Applied Earth Observation and Geoinformation*, 28:150–159. doi:10.1016/j.jag.2013.12.002.
- Matgen, P., Montanari, M., Hostache, R., Pfister, L., Hoffmann, L., Plaza, D., Pauwels, V. R. N., De Lannoy, G. J. M., De Keyser, R., and Savenije, H. H. G., 2010. Towards the sequential assimilation of SAR-derived water stages into hydraulic models using the Particle Filter: proof of concept. *Hydrology and Earth System Sciences*, 14(9):1773–1785. doi:10.5194/hess-14-1773-2010.
- Matgen, P., Hostache, R., Schumann, G. J.-P., Pfister, L., Hoffmann, L., and Savenije, H., 2011. Towards an automated SAR-based flood monitoring system: Lessons learned from two case studies. *Physics and Chemistry of the Earth, Parts A/B/C*, 36(7-8):241–252. doi:10.1016/j.pce.2010.12.009.
- Matgen, P., Corato, G., Chini, M., Hostache, R., and Giustarini, L., 2015. Improved flood forecasting through the assimilation of SAR-derived flood probability maps into 2D hydrodynamic models. In *IEEE International Geoscience and Remote Sensing Symposium (IGARSS)*, Milan, Italy, July 26-31.
- Mercier, G., Derrode, S., Trouvé, E., and Bombrun, L., 2009. Change detection in remote sensing observation. In Chanussot, J., Collet, C., and Chehdi, K., editors, *Multivariate Image Processing: Methods and Applications*, pages 95–142. ISTE Ltd and John Wiley & Sons Inc. ISBN 978-1-84821-139-1.
- Michailovsky, C. I., McEnnis, S., Berry, P. A. M., Smith, R., and Bauer-Gottwein, P., 2012. River monitoring from satellite radar altimetry in the Zambezi River basin. *Hydrology and Earth System Sciences*, 16(7):2181–2192. doi:10.5194/hess-16-2181-2012.
- Mitchell, S. A., 2012. The status of wetlands, threats and the predicted effect of global climate change: the situation in Sub-Saharan Africa. *Aquatic Sciences*, 75(1):95–112. doi:10.1007/s00027-012-0259-2.

- Morandeira, N., Grings, F., Facchinetti, C., and Kandus, P., 2016. Mapping Plant Functional Types in Floodplain Wetlands: An Analysis of C-Band Polarimetric SAR Data from RADARSAT-2. *Remote Sensing*, 8(3):174. doi:10.3390/rs8030174.
- MunichRe, 2012. NatCatSERVICE Data Base. URL <http://www.munichre.com/de/reinsurance/business/non-life/natcatservice/index.html>.
- MunichRe, 2016. NatCatSERVICE – Loss events worldwide 1980-2015. Technical report. URL [https://www.munichre.com/site/touch-naturalhazards/get/documents\\_E-1125431578/mr/assetpool.shared/Documents/5\\_Touch/\\_NatCatService/Focus\\_analyses/Loss\\_events\\_worldwide\\_1980-2015.pdf](https://www.munichre.com/site/touch-naturalhazards/get/documents_E-1125431578/mr/assetpool.shared/Documents/5_Touch/_NatCatService/Focus_analyses/Loss_events_worldwide_1980-2015.pdf).
- Munyati, C., 2000. Wetland change detection on the Kafue Flats, Zambia, by classification of a multitemporal remote sensing image dataset. *International Journal of Remote Sensing*, 21(9):1787–1806. doi:10.1080/014311600209742.
- Nagler, T. and Rott, H., 2000. Retrieval of Wet Snow by Means of Multitemporal SAR Data. *IEEE Transactions on Geoscience and Remote Sensing*, 38(2):754–765. doi:10.1109/36.842004.
- Nakmuenwai, P., Yamazaki, F., and Liu, W., 2017. Automated Extraction of Inundated Areas from Multi-Temporal Dual-Polarization RADARSAT-2 Images of the 2011 Central Thailand Flood. *Remote Sensing*, 9(1):78. doi:10.3390/rs9010078.
- Nobre, A., Cuartas, L., Hodnett, M., Rennó, C., Rodrigues, G., Silveira, A., Waterloo, M., and Saleska, S., 2011. Height Above the Nearest Drainage - a hydrologically relevant new terrain model. *Journal of Hydrology*, 404(1): 13–29. doi:10.1016/j.jhydrol.2011.03.051.
- Nobre, A. D., Cuartas, L. A., Momo, M. R., Severo, D. L., Pinheiro, A., and Nobre, C. A., 2016. HAND contour: a new proxy predictor of inundation extent. *Hydrological Processes*, 30(2):320–333. doi:10.1002/hyp.10581.
- O’Grady, D., Leblanc, M., and Gillieson, D., 2011. Use of ENVISAT ASAR Global Monitoring Mode to complement optical data in the mapping of rapid broad-scale flooding in Pakistan. *Hydrology and Earth System Sciences*, 15(11):3475–3494. doi:10.5194/hess-15-3475-2011.

- O'Grady, D., Leblanc, M., and Gillieson, D., 2013. Relationship of local incidence angle with satellite radar backscatter for different surface conditions. *International Journal of Applied Earth Observation and Geoinformation*, 24:42–53. doi:10.1016/j.jag.2013.02.005.
- O'Grady, D., Leblanc, M., and Bass, A., 2014. The use of radar satellite data from multiple incidence angles improves surface water mapping. *Remote Sensing of Environment*, 140:652–664. doi:10.1016/j.rse.2013.10.006.
- Oh, Y., Sarabandi, K., and Ulaby, F., 1992. An empirical model and an inversion technique for radar scattering from bare soil surfaces. *IEEE Transactions on Geoscience and Remote Sensing*, 30(2):370–381. doi:10.1109/36.134086.
- Otsu, N., 1979. A Threshold Selection Method from Gray-Level Histograms. *IEEE Transactions on Systems, Man and Cybernetics*, 9(1):62–66. doi:10.1109/TSMC.1979.4310076.
- Ozesmi, S. L. and Bauer, M. E., 2002. Satellite remote sensing of wetlands. *Wetlands Ecology and Management*, 10(5):381–402.
- Pathe, C., Wagner, W., Sabel, D., Doubkova, M., and Basara, J. B., 2009. Using ENVISAT ASAR Global Mode Data for Surface Soil Moisture Retrieval Over Oklahoma, USA. *IEEE Transactions on Geoscience and Remote Sensing*, 47(2):468–480. doi:10.1109/TGRS.2008.2004711.
- Pierdicca, N., Chini, M., Pulvirenti, L., and Macina, F., 2008. Integrating Physical and Topographic Information Into a Fuzzy Scheme to Map Flooded Area by SAR. *Sensors*, 8(7):4151–4164. doi:10.3390/s8074151.
- Pierdicca, N., Pulvirenti, L., and Chini, M., 2013a. Dealing with flood mapping using SAR data in the presence of wind or heavy precipitation. In Notarnicola, C., Paloscia, S., and Pierdicca, N., editors, *Proc. SPIE*, volume 8891, page 88910K. doi:10.1117/12.2030105.
- Pierdicca, N., Pulvirenti, L., Chini, M., Guerriero, L., and Candela, L., 2013b. Observing floods from space: Experience gained from COSMO-SkyMed observations. *Acta Astronautica*, 84:122–133. doi:10.1016/j.actaastro.2012.10.034.
- Pierdicca, N., Fascetti, F., Pulvirenti, L., Crapolicchio, R., and Muñoz-Sabater, J., 2015. Analysis of ASCAT, SMOS, in-situ and land model soil

- moisture as a regionalized variable over Europe and North Africa. *Remote Sensing of Environment*, 170:280–289. doi:10.1016/j.rse.2015.09.005.
- Prigent, C., Papa, F., Aires, F., Rossow, W. B., and Matthews, E., 2007. Global inundation dynamics inferred from multiple satellite observations, 1993-2000. *Journal of Geophysical Research*, 112(D12):D12107. doi:10.1029/2006JD007847.
- Pulvirenti, L., Chini, M., Pierdicca, N., Guerriero, L., and Ferrazzoli, P., 2011a. Flood monitoring using multi-temporal COSMO-SkyMed data: Image segmentation and signature interpretation. *Remote Sensing of Environment*, 115(4):990–1002. doi:10.1016/j.rse.2010.12.002.
- Pulvirenti, L., Pierdicca, N., Chini, M., and Guerriero, L., 2011b. An algorithm for operational flood mapping from Synthetic Aperture Radar (SAR) data using fuzzy logic. *Natural Hazards and Earth System Science*, 11(2):529–540. doi:10.5194/nhess-11-529-2011.
- Pulvirenti, L., Chini, M., Pierdicca, N., and Boni, G., 2016. Use of SAR Data for Detecting Floodwater in Urban and Agricultural Areas: The Role of the Interferometric Coherence. *IEEE Transactions on Geoscience and Remote Sensing*, 54(3):1532–1544. doi:10.1109/TGRS.2015.2482001.
- Quegan, S., Le Toan, T., Yu, J. J., Ribbes, F., and Floury, N., 2000. Multi-temporal ERS SAR analysis applied to forest mapping. *IEEE Transactions on Geoscience and Remote Sensing*, 38(2):741–753. doi:10.1109/36.842003.
- R Core Team, 2014. *R: A Language and Environment for Statistical Computing*. R Foundation for Statistical Computing, Vienna, Austria. URL <https://www.r-project.org/>.
- Ramsar, 2015. Briefing Note 7: State of the World’s Wetlands and their Services to People: A compilation of recent analyses. Technical report, Ramsar Convention. URL [http://www.ramsar.org/sites/default/files/documents/library/bn7e\\_0.pdf](http://www.ramsar.org/sites/default/files/documents/library/bn7e_0.pdf).
- Ramsar, 2017. The List of Wetlands of International Importance. URL <http://www.ramsar.org/sites/default/files/documents/library/sitelist.pdf>.
- Refice, A., Capolongo, D., Pasquariello, G., DaAddabbo, A., Bovenga, F., Nutricato, R., Lovergine, F. P., and Pietranera, L., 2014. SAR and InSAR for Flood Monitoring: Examples With COSMO-SkyMed Data. *IEEE Journal*

- of Selected Topics in Applied Earth Observations and Remote Sensing*, 7(7): 2711–2722. doi:10.1109/JSTARS.2014.2305165.
- Rennó, C. D., Nobre, A. D., Cuartas, L. A., Soares, J. V., Hodnett, M. G., Tomasella, J., and Waterloo, M. J., 2008. HAND, a new terrain descriptor using SRTM-DEM: Mapping terra-firme rainforest environments in Amazonia. *Remote Sensing of Environment*, 112(9):3469–3481. doi:10.1016/j.rse.2008.03.018.
- Reschke, J., Bartsch, A., Schlaffer, S., and Schepaschenko, D., 2012. Capability of C-Band SAR for Operational Wetland Monitoring at High Latitudes. *Remote Sensing*, 4(12):2923–2943. doi:10.3390/rs4102923.
- Richards, J. A., 2009. *Remote Sensing with Imaging Radar*. Signals and Communication Technology. Springer, Berlin, Heidelberg. ISBN 978-3-642-02019-3. doi:10.1007/978-3-642-02020-9.
- Sabel, D., Bartalis, Z., Wagner, W., Doubkova, M., and Klein, J.-P., 2012. Development of a Global Backscatter Model in support to the Sentinel-1 mission design. *Remote Sensing of Environment*, 120:102–112. doi:10.1016/j.rse.2011.09.028.
- Saich, P. and Borgeaud, M., 2000. Interpreting ERS SAR signatures of agricultural crops in Flevoland, 1993-1996. *IEEE Transactions on Geoscience and Remote Sensing*, 38(2):651–657. doi:10.1109/36.841995.
- Santoro, M. and Wegmüller, U., 2014. Multi-temporal Synthetic Aperture Radar Metrics Applied to Map Open Water Bodies. *IEEE Journal of Selected Topics in Applied Earth Observations and Remote Sensing*, 7(8):3225–3238. doi:10.1109/JSTARS.2013.2289301.
- Santoro, M., Beer, C., Cartus, O., Schmullius, C., Shvidenko, A., McCallum, I., Wegmüller, U., and Wiesmann, A., 2011. Retrieval of growing stock volume in boreal forest using hyper-temporal series of Envisat ASAR ScanSAR backscatter measurements. *Remote Sensing of Environment*, 115(2):490–507. doi:10.1016/j.rse.2010.09.018.
- Santoro, M., Wegmüller, U., Lamarche, C., Bontemps, S., Defourny, P., and Arino, O., 2015. Strengths and weaknesses of multi-year Envisat ASAR backscatter measurements to map permanent open water bodies at global scale. *Remote Sensing of Environment*, 171:185–201. doi:10.1016/j.rse.2015.10.031.

- Schelle, P. and Pittock, J., 2005. Restoring the Kafue Flats: A partnership approach to environmental flows in Zambia. In *Brisbane River Symposium*, pages 1–10.
- Schlaffer, S., Matgen, P., Hollaus, M., and Wagner, W., 2015. Flood detection from multi-temporal SAR data using harmonic analysis and change detection. *International Journal of Applied Earth Observation and Geoinformation*, 38:15–24. doi:10.1016/j.jag.2014.12.001.
- Schlaffer, S., Chini, M., Dettmering, D., and Wagner, W., 2016. Mapping Wetlands in Zambia Using Seasonal Backscatter Signatures Derived from ENVISAT ASAR Time Series. *Remote Sensing*, 8(5):402. doi:10.3390/rs8050402.
- Schlaffer, S., Chini, M., Giustarini, L., and Matgen, P., 2017. Probabilistic mapping of flood-induced backscatter changes in SAR time series. *International Journal of Applied Earth Observation and Geoinformation*, 56:77–87. doi:10.1016/j.jag.2016.12.003.
- Schmitt, A. and Brisco, B., 2013. Wetland Monitoring Using the Curvelet-Based Change Detection Method on Polarimetric SAR Imagery. *Water*, 5(3):1036–1051. doi:10.3390/w5031036.
- Schumann, G., Pappenberger, F., and Matgen, P., 2008. Estimating uncertainty associated with water stages from a single SAR image. *Advances in Water Resources*, 31(8):1038–1047. doi:10.1016/j.advwatres.2008.04.008.
- Schumann, G. J.-P. and Moller, D. K., 2015. Microwave remote sensing of flood inundation. *Physics and Chemistry of the Earth, Parts A/B/C*, 83–84:84–95. doi:10.1016/j.pce.2015.05.002.
- Schumann, G. J.-P., Di Baldassarre, G., and Bates, P. D., 2009. The Utility of Spaceborne Radar to Render Flood Inundation Maps Based on Multialgorithm Ensembles. *IEEE Transactions on Geoscience and Remote Sensing*, 47(8):2801–2807. doi:10.1109/TGRS.2009.2017937.
- Schumann, G. J.-P., Neal, J. C., Mason, D. C., and Bates, P. D., 2011. The accuracy of sequential aerial photography and SAR data for observing urban flood dynamics, a case study of the UK summer 2007 floods. *Remote Sensing of Environment*, 115(10):2536–2546. doi:10.1016/j.rse.2011.04.039.
- Schumann, G. J.-P., Neal, J. C., Voisin, N., Andreadis, K. M., Pappenberger, F., Phanthuwongpakdee, N., Hall, A. C., and Bates, P. D., 2013. A first

- large-scale flood inundation forecasting model. *Water Resources Research*, 49(10):6248–6257. doi:10.1002/wrcr.20521.
- Schumann, G. J.-P., Frye, S., Wells, G., Adler, R., Brakenridge, R., Bolten, J., Murray, J., Slayback, D., Policelli, F., Kirschbaum, D., Wu, H., Cappelaere, P., Howard, T., Flamig, Z., Clark, R., Stough, T., Chini, M., Matgen, P., Green, D., and Jones, B., 2016. Unlocking the full potential of Earth observation during the 2015 Texas flood disaster. *Water Resources Research*, 52(5):3288–3293. doi:10.1002/2015WR018428.
- Schwatke, C., Dettmering, D., Bosch, W., and Seitz, F., 2015. DAHITI â an innovative approach for estimating water level time series over inland waters using multi-mission satellite altimetry. *Hydrology and Earth System Sciences*, 19(10):4345–4364. doi:10.5194/hess-19-4345-2015.
- Serpico, S. B., Dellepiane, S., Boni, G., Moser, G., Angiati, E., and Rudari, R., 2012. Information Extraction From Remote Sensing Images for Flood Monitoring and Damage Evaluation. *Proceedings of the IEEE*, 100(10):2946–2970. doi:10.1109/JPROC.2012.2198030.
- Small, D. and Schubert, A., 2008. Guide to ASAR Geocoding. Technical report, RSL, University of Zürich, Zürich. URL [http://www.geo.uzh.ch/microsite/rsl-documents/research/publications/other-sci-communications/2008\\_RSL-ASAR-GC-AD-v101-0335607552/2008\\_RSL-ASAR-GC-AD-v101.pdf](http://www.geo.uzh.ch/microsite/rsl-documents/research/publications/other-sci-communications/2008_RSL-ASAR-GC-AD-v101-0335607552/2008_RSL-ASAR-GC-AD-v101.pdf).
- Tarpanelli, A., Brocca, L., Melone, F., and Moramarco, T., 2013. Hydraulic modelling calibration in small rivers by using coarse resolution synthetic aperture radar imagery. *Hydrological Processes*, 27(9):1321–1330. doi:10.1002/hyp.9550.
- Torres, R., Snoeij, P., Geudtner, D., Bibby, D., Davidson, M., Attema, E., Potin, P., Rommen, B., Floury, N., Brown, M., Traver, I. N., Deghaye, P., Duesmann, B., Rosich, B., Miranda, N., Bruno, C., L’Abbate, M., Croci, R., Pietropaolo, A., Huchler, M., and Rostan, F., 2012. GMES Sentinel-1 mission. *Remote Sensing of Environment*, 120:9–24. doi:10.1016/j.rse.2011.05.028.
- Töyrä, J., Pietroniro, A., and Martz, L. W., 2001. Multisensor Hydrologic Assessment of a Freshwater Wetland. *Remote Sensing of Environment*, 75(2):162–173. doi:10.1016/S0034-4257(00)00164-4.

- Twele, A., Cao, W., Plank, S., and Martinis, S., 2016. Sentinel-1-based flood mapping: a fully automated processing chain. *International Journal of Remote Sensing*, 37(13):2990–3004. doi:10.1080/01431161.2016.1192304.
- Ulaby, F. T., Moore, R. K., and Fung, A. K., 1986. *Microwave Remote Sensing: Active and Passive - Volume III: From Theory to Applications*. Artech House, Norwood, USA. ISBN 0-89006-192-0.
- United Nations. Sendai Framework for Disaster Risk Reduction 2015-2030. 2015. URL <http://www.unisdr.org/we/inform/publications/43291>.
- Van doninck, J., Peters, J., Lievens, H., De Baets, B., and Verhoest, N. E. C., 2012. Accounting for seasonality in a soil moisture change detection algorithm for ASAR Wide Swath time series. *Hydrology and Earth System Sciences*, 16(3):773–786. doi:10.5194/hess-16-773-2012.
- Van doninck, J., Wagner, W., Melzer, T., De Baets, B., and Verhoest, N. E. C., 2014. Seasonality in the Angular Dependence of ASAR Wide Swath Backscatter. *IEEE Geoscience and Remote Sensing Letters*, 11(8):1423–1427. doi:10.1109/LGRS.2013.2294725.
- Verbesselt, J., Hyndman, R., Zeileis, A., and Culvenor, D., 2010. Phenological change detection while accounting for abrupt and gradual trends in satellite image time series. *Remote Sensing of Environment*, 114(12):2970–2980. doi:10.1016/j.rse.2010.08.003.
- Verbesselt, J., Zeileis, A., and Herold, M., 2012. Near real-time disturbance detection using satellite image time series. *Remote Sensing of Environment*, 123:98–108. doi:10.1016/j.rse.2012.02.022.
- Vörösmarty, C., 2002. Global water assessment and potential contributions from Earth Systems Science. *Aquatic Sciences*, 64:328–351. doi:10.1007/PL00012590.
- Wagner, W., Lemoine, G., Borgeaud, M., and Rott, H., 1999a. A study of vegetation cover effects on ERS scatterometer data. *IEEE Transactions on Geoscience and Remote Sensing*, 37(2):938–948. doi:10.1109/36.752212.
- Wagner, W., Lemoine, G., and Rott, H., 1999b. A Method for Estimating Soil Moisture from ERS Scatterometer and Soil Data. *Remote Sensing of Environment*, 70(2):191–207. doi:10.1016/S0034-4257(99)00036-X.

- Wagner, W., Noll, J., Borgeaud, M., and Rott, H., 1999c. Monitoring soil moisture over the Canadian Prairies with the ERS scatterometer. *IEEE Transactions on Geoscience and Remote Sensing*, 37(1):206–216. doi:10.1109/36.739155.
- Wagner, W., Pathe, C., Doubkova, M., Sabel, D., Bartsch, A., Hasenauer, S., Blöschl, G., Scipal, K., Martínez-Fernández, J., and Löw, A., 2008. Temporal Stability of Soil Moisture and Radar Backscatter Observed by the Advanced Synthetic Aperture Radar (ASAR). *Sensors*, 8(4):1174–1197. doi:10.3390/s8021174.
- Wang, Y., Hess, L. L., Filoso, S., and Melack, J. M., 1995. Understanding the radar backscattering from flooded and nonflooded Amazonian forests: Results from canopy backscatter modeling. *Remote Sensing of Environment*, 54(3):324–332. doi:10.1016/0034-4257(95)00140-9.
- Westerhoff, R. S., Kleuskens, M. P. H., Winsemius, H. C., Huizinga, H. J., Brakenridge, G. R., and Bishop, C., 2013. Automated global water mapping based on wide-swath orbital synthetic-aperture radar. *Hydrology and Earth System Sciences*, 17(2):651–663. doi:10.5194/hess-17-651-2013.
- White, L., Brisco, B., Dabboor, M., Schmitt, A., and Pratt, A., 2015. A Collection of SAR Methodologies for Monitoring Wetlands. *Remote Sensing*, 7(6):7615–7645. doi:10.3390/rs70607615.
- Wilks, D. S., 2011. *Statistical Methods in the Atmospheric Sciences*. Academic Press, Oxford, Amsterdam, Waltham, San Diego, 3rd edition. ISBN 978-0123850225.
- Winsemius, H. C., Aerts, J. C. J. H., van Beek, L. P. H., Bierkens, M. F. P., Bouwman, A., Jongman, B., Kwadijk, J. C. J., Ligtvoet, W., Lucas, P. L., van Vuuren, D. P., and Ward, P. J., 2015. Global drivers of future river flood risk. *Nature Climate Change*, 6(4):381–385. doi:10.1038/nclimate2893.
- Wood, M., Hostache, R., Neal, J., Wagener, T., Giustarini, L., Chini, M., Corato, G., Matgen, P., and Bates, P., 2016. Calibration of channel depth and friction parameters in the LISFLOOD-FP hydraulic model using medium-resolution SAR data and identifiability techniques. *Hydrology and Earth System Sciences*, 20(12):4983–4997. doi:10.5194/hess-20-4983-2016.
- Woodhouse, I., van der Sanden, J., and Hoekman, D., 1999. Scatterometer observations of seasonal backscatter variation over tropical rain for-

- est. *IEEE Transactions on Geoscience and Remote Sensing*, 37(2):859–861. doi:10.1109/36.752204.
- Woodhouse, I. H., 2005. *Introduction to Microwave Remote Sensing*. CRC Press. ISBN 041527124X.
- World Food Programme, 2010. Pakistan flood impact assessment. Technical report. URL <http://documents.wfp.org/stellent/groups/public/documents/ena/wfp225987.pdf>.
- Xie, H., Pierce, L. E., and Ulaby, F. T., 2002. Statistical properties of logarithmically transformed speckle. *IEEE Transactions on Geoscience and Remote Sensing*, 40(3):721–727. doi:10.1109/TGRS.2002.1000333.
- Yan, K., Di Baldassarre, G., Solomatine, D. P., and Schumann, G. J.-P., 2015. A review of low-cost space-borne data for flood modelling: topography, flood extent and water level. *Hydrological Processes*, 29:3368–3387. doi:10.1002/hyp.10449.
- Yuan, T., Lee, H., and Jung, H., 2015. Toward Estimating Wetland Water Level Changes Based on Hydrological Sensitivity Analysis of PALSAR Backscattering Coefficients over Different Vegetation Fields. *Remote Sensing*, 7(3):3153–3183. doi:10.3390/rs70303153.
- Zhang, M., Li, Z., Tian, B., Zhou, J., and Tang, P., 2016. The backscattering characteristics of wetland vegetation and water-level changes detection using multi-mode SAR: A case study. *International Journal of Applied Earth Observation and Geoinformation*, 45:1–13. doi:10.1016/j.jag.2015.10.001.
- Zlatanova, S., 2013. Flood and flood risk: Mapping, monitoring and damage assessment. In Altan, O., Backhaus, R., Boccardo, P., Tonolo, F. G., Trinder, J., van Manen, N., and Zlatanova, S., editors, *The Value of Geoinformation for Disaster and Risk Management (VALID) - Benefit Analysis and Stakeholder Assessment*, chapter 4.1, pages 33–43. Joint Board of Geospatial Information Societies, Copenhagen, Denmark. ISBN 978-87-90907-88-4. URL <http://www.un-spider.org/sites/default/files/VALIDPublication.pdf>.
- Zurbrügg, R., Wamulume, J., Kamanga, R., Wehrli, B., and Senn, D. B., 2012. River-floodplain exchange and its effects on the fluvial oxygen regime in a large tropical river system (Kafue Flats, Zambia). *Journal of Geophysical Research*, 117(G3):G03008. doi:10.1029/2011JG001853.

- Zwenzner, H. and Voigt, S., 2009. Improved estimation of flood parameters by combining space based SAR data with very high resolution digital elevation data. *Hydrology and Earth System Sciences*, 13(5):567–576. doi:10.5194/hess-13-567-2009.



# Appendix A

## Supplementary figures to Chapter 2: Mapping wetlands in Zambia using seasonal backscatter signatures derived from ENVISAT ASAR time series

*This appendix was published as supplementary material to: Schlaffer, S., Chini, M., Dettmering, D., Wagner, W. (2016) Mapping Wetlands in Zambia Using Seasonal Backscatter Signatures Derived from ENVISAT ASAR Time Series. Remote Sensing, 8(5), 402. For the original see <http://dx.doi.org/10.3390/rs8050402>.*

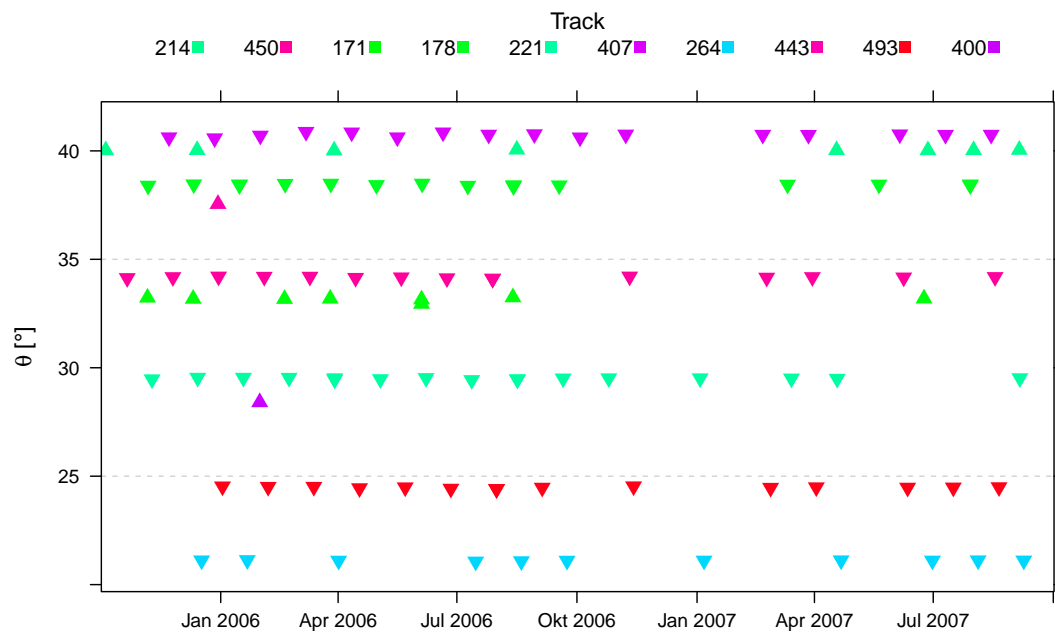


Figure A.1: Local incidence angles of ASAR scenes averaged over the Ka-fue Flats. Triangles sharing the same colour belong to the same track.  $\blacktriangle$  ascending,  $\blacktriangledown$  descending orbital node.

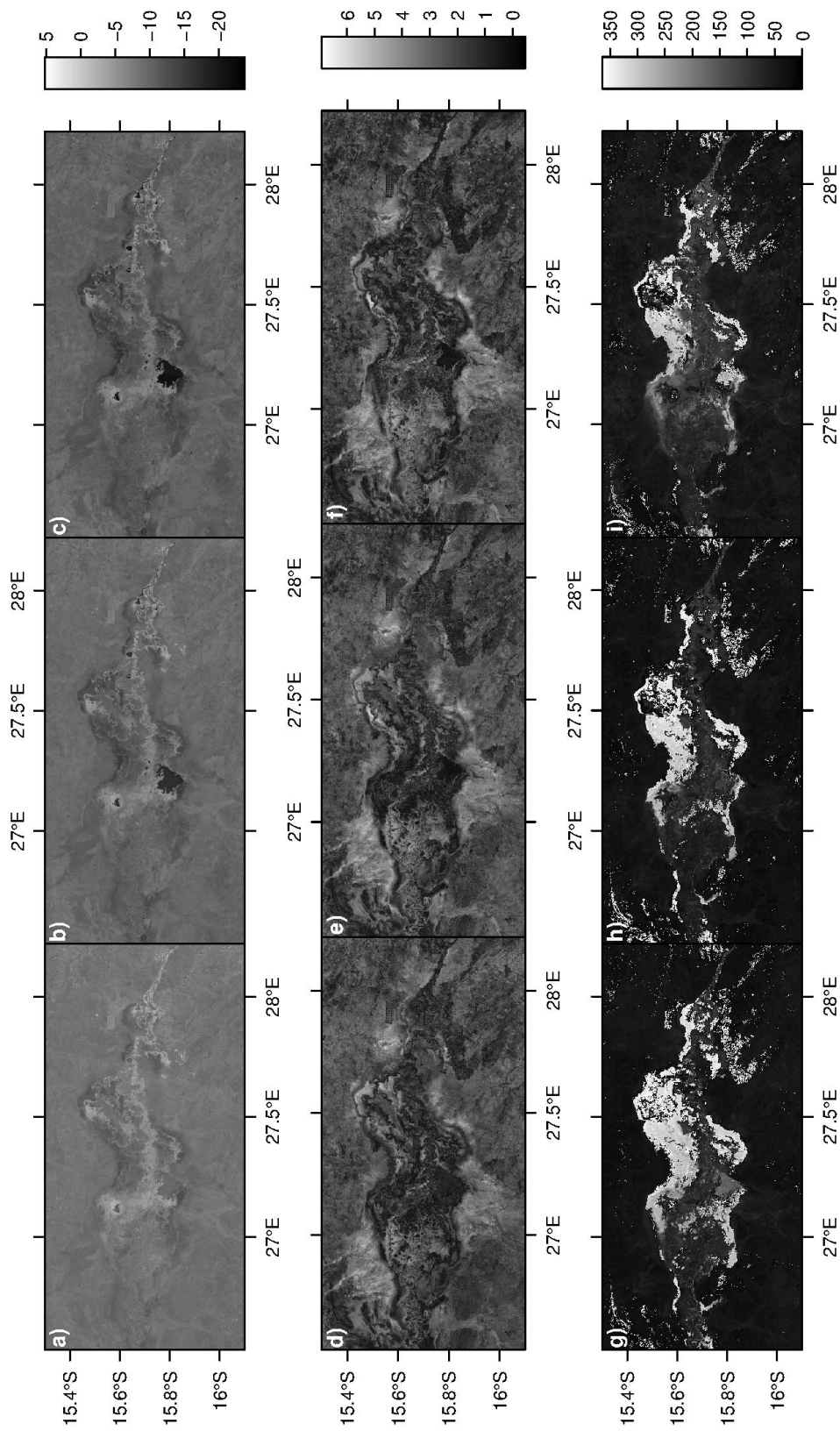


Figure A.2: Harmonic model parameters (a)  $\bar{\sigma}^0(15^\circ - 25^\circ)$  [dB], (b)  $\bar{\sigma}^0(25^\circ - 35^\circ)$  [dB], (c)  $\bar{\sigma}^0(35^\circ - 45^\circ)$  [dB], (d)  $A_1(15^\circ - 25^\circ)$  [dB], (e)  $A_1(25^\circ - 35^\circ)$  [dB], (f)  $A_1(35^\circ - 45^\circ)$  [dB], (g)  $\phi_1(15^\circ - 25^\circ)$  [DoY], (h)  $\phi_1(25^\circ - 35^\circ)$  [DoY], (i)  $\phi_1(35^\circ - 45^\circ)$  [DoY].

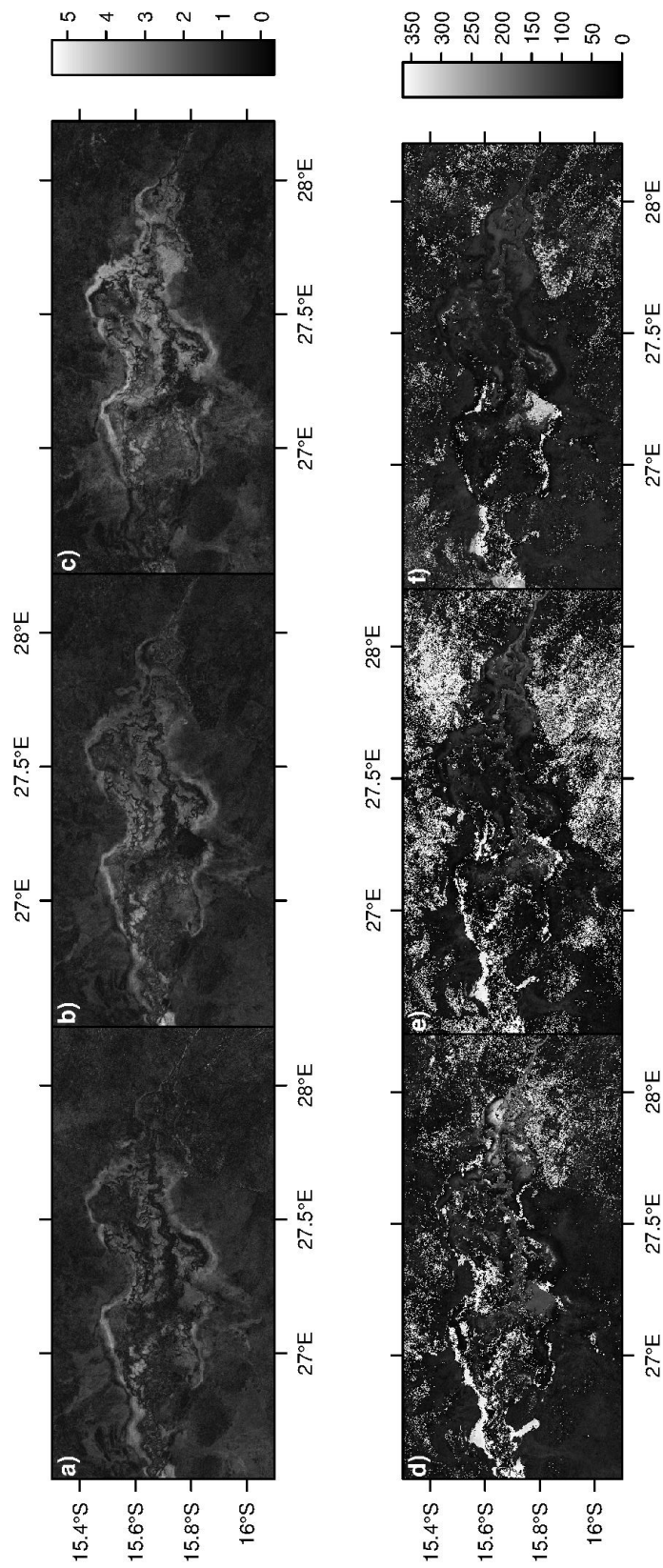


Figure A.3: Harmonic model parameters (a)  $A_2(15^\circ - 25^\circ)$  [dB], (b)  $A_2(25^\circ - 35^\circ)$  [dB], (c)  $A_2(35^\circ - 45^\circ)$  [dB], (d)  $\phi_2(15^\circ - 25^\circ)$  [DoY], (e)  $\phi_2(25^\circ - 35^\circ)$  [DoY], (f)  $\phi_2(35^\circ - 45^\circ)$  [DoY].

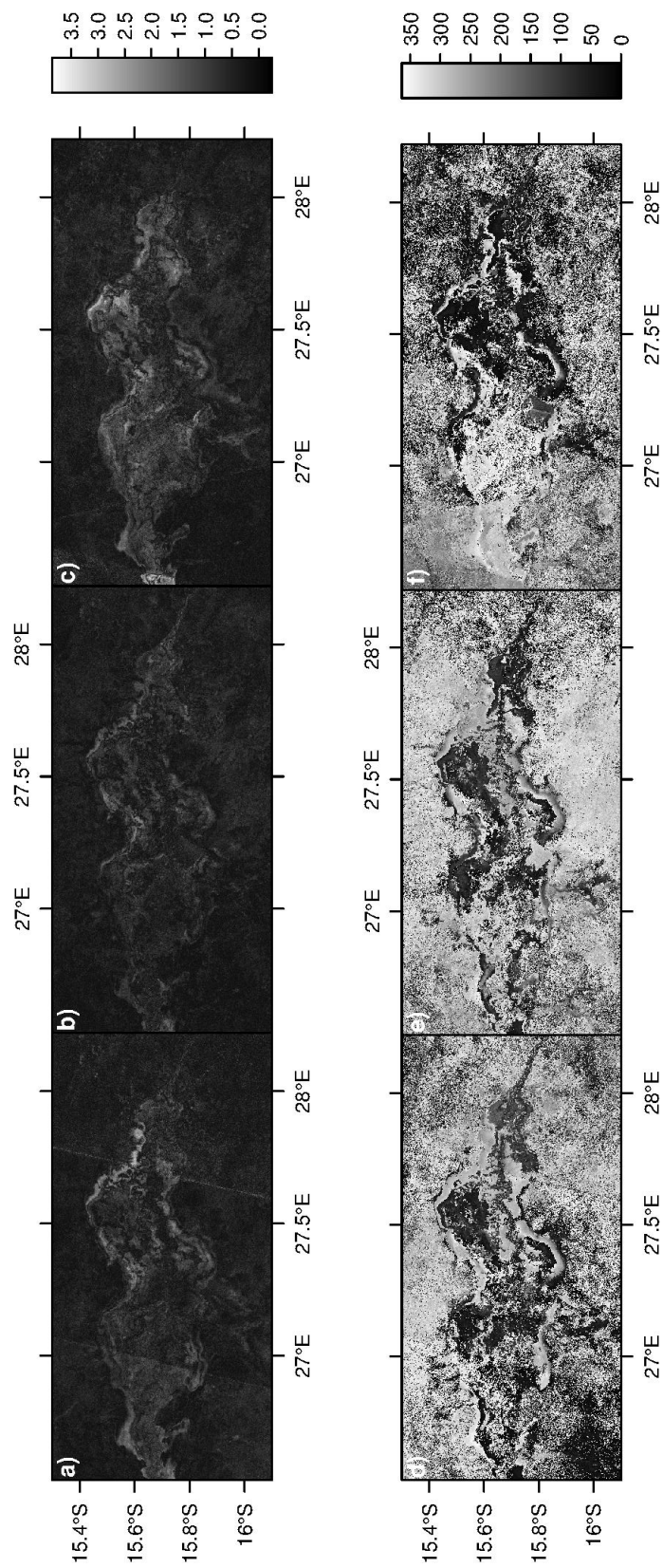


Figure A.4: Harmonic model parameters (a)  $A_3(15^\circ - 25^\circ)$  [dB], (b)  $A_3(25^\circ - 35^\circ)$  [dB], (c)  $A_3(35^\circ - 45^\circ)$  [dB], (d)  $\phi_3(15^\circ - 25^\circ)$  [DoY], (e)  $\phi_3(25^\circ - 35^\circ)$  [DoY], (f)  $\phi_3(35^\circ - 45^\circ)$  [DoY].

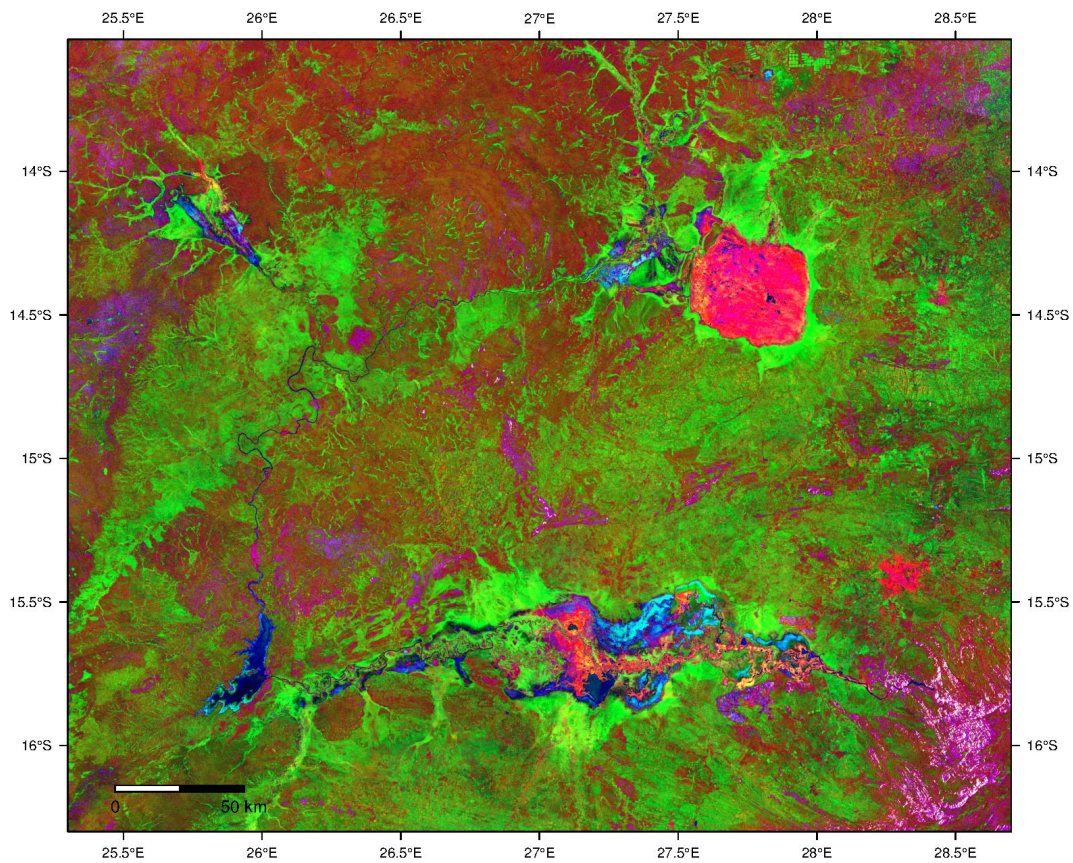


Figure A.5: RGB composite of harmonic model components used for wetland extent mapping in the Kafue River Basin (R:  $\bar{\sigma}^0$ ; G:  $A_1$ ; B:  $\phi_1$ ).

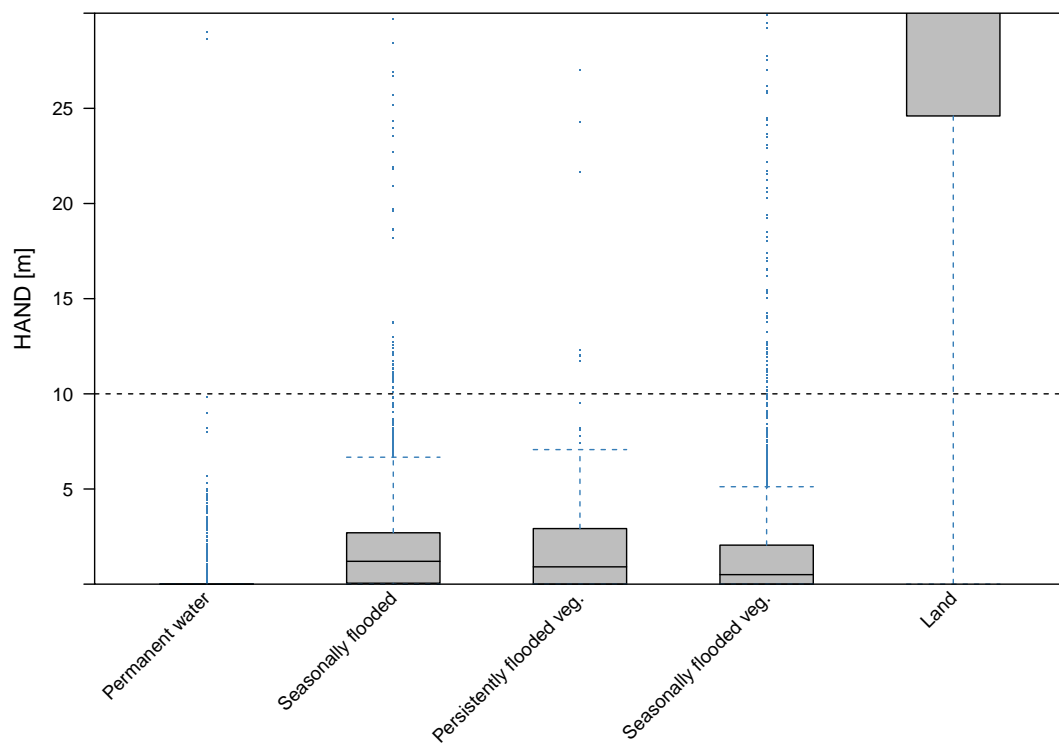


Figure A.6: Box-Whisker-Plots showing median (line) and interquartile range (box) of the Height Above Nearest Drainage (HAND) index for each of the derived classes. Whiskers span up to 1.5 times the interquartile range. The horizontal line shows the selected threshold value used for masking.



# Appendix B

## CV

# Stefan Schlaffer

Dipl.-Geoökologe

*Born 5 November 1979*

*Florianstr. 3  
92224 Amberg, Germany*

*E-mail: [stschlaffer@gmx.net](mailto:stschlaffer@gmx.net)  
Mobile: +49 162 9291162*

*[https://www.researchgate.net/profile/Stefan\\_Schlaffer](https://www.researchgate.net/profile/Stefan_Schlaffer)*

## professional experience

Feb. 2017-  
present

**American University of Armenia, Yerevan, Armenia**

CIM Integrated Expert

Establishment of a GIS and Remote Sensing Lab in support of German-Armenian international cooperation in integrated biodiversity management in the South Caucasus region

Sept. 2015-  
Mar. 2016

**Luxembourg Institute of Science and Technology, Belvaux, Luxembourg**

Guest Researcher, Marietta Blau scholar

Research collaboration in support of PhD thesis with the topic “*Derivation of land-surface backscatter signatures from SAR time series in support of flood and wetland delineation*”

- Probabilistic flood mapping using SAR time series
- Development of a wetland mapping algorithm

July 2010-  
July 2015

**Department of Geodesy and Geoinformation, Vienna University of Technology, Vienna, Austria**

Project Assistant

Involved in several international projects aimed at recovery of geophysical parameters using satellite data, funded by the European Space Agency (ESA), FFG and European Union

- Development of automated processing chains for derivation of flooded areas, wetlands and soil moisture from Synthetic Aperture Radar (SAR) data in the ESA-funded WATCHFUL, FAAPS, ALANIS-Methane, TIGER-NET and DUE Permafrost projects
- Project coordination in the ESA-funded STSE Water Cycle Feasibility Study (WATCHFUL) project

Sept. 2008-  
May 2010

**Dr.-Ing. Karl Ludwig Wasserwirtschaft - Wasserbau GmbH, Karlsruhe, Germany**

Hydrological Modeller

Involved in several projects funded by German flood prediction centres consisting of setup and calibration of operational flood prediction models and climate change impact studies

- Hydrological modelling using the model system LARSIM for the German states Bavaria, North Rhine-Westphalia, Hesse and Baden-Württemberg
- Responsible for quality control and management of input data using statistical analysis methods

Aug. 2007-  
Aug. 2008

**Center for Environmental Systems Research, University of Kassel, Kassel, Germany**

Research Assistant

Research projects “GLOWA-Jordan-River” and “MoMo” funded by the German Ministry of Education and Research (BMBF)

- Software development for geostatistical regionalisation of meteorological parameters
- Water balance modelling for several test sites in Israel

## education

Mar. 2013-  
present

**Vienna University of Technology, Vienna, Austria**

PhD studies in Geoinformation and Remote Sensing

Oct. 2000-  
Jan. 2007

**University of Bayreuth, Bayreuth, Germany**

Geoecology (Diplom, equiv. to M.Sc.)

Major subjects: hydrology, soil ecology; minor subjects: hydrogeology, development studies

Master's thesis: *Tree Species Effects on N Mineralisation in Tropical Plantations Compared to Primary Forest and Grassland*

Aug. 2003-  
June 2004

**University of Guadalajara, Guadalajara, Mexico**

Exchange student (agronomy)

## IT skills

Programming: R, Python, IDL, Fortran

GIS/Remote sensing: ArcGIS, QGIS, ENVI, ESA SNAP, Sarscape

Databases: MySQL, PostgreSQL

Hydrological models: LARSIM

## languages

Native German; fluent English; advanced Spanish; intermediate French

## additional skills

- Microwave and optical remote sensing
- Hydrological modelling
- Processing of large datasets
- Project coordination
- Writing of publications, project proposals and technical reports

## scholarships

- Marietta Blau scholarship of the Austrian Ministry of Science, Research and Economy (2015-2016)
- Travel grant of Vienna University of Technology (2016)
- Research scholarship of the German Academic Exchange Service (2005)

## publications

**Schlaffer, S.**, Chini, M., Giustarini, L., Matgen, P. (2017) Probabilistic mapping of flood-induced backscatter changes in SAR time series. *Int. J. Appl. Earth Obs. Geoinf.*, 56, 77-87.

**Schlaffer, S.**, Chini, M., Dettmering, D., Wagner, W. (2016) Mapping Wetlands in Zambia Using Seasonal Backscatter Signatures derived from ENVISAT ASAR Time Series. *Remote Sens.* 8(5), 402.

Giustarini, L., Hostache, R., Kavetski, D., Chini, M., Corato, G., **Schlaffer, S.**, Matgen, P. (2016) Probabilistic flood mapping using Synthetic Aperture Radar data. *IEEE Trans. Geosci. Remote Sens.*, 54(12), 6958-6969.

**Schlaffer, S.**, Matgen, P., Hollaus, M., Wagner, W. (2015) Flood detection from multi-temporal SAR data using harmonic analysis and change detection. *Int. J. Appl. Earth Obs. Geoinf.*, 38, 15-24.

Munier, S., Aires, F., **Schlaffer, S.**, Prigent, C., Papa, F., et al. (2014) Combining datasets of satellite-retrieved products for basin-scale water balance study: 2. Evaluation on the Mississippi Basin and closure correction model. *J. Geophys. Res. Atm.*, 119, 12,100-12,115.

Reschke, J., Bartsch, A., **Schlaffer, S.**, Schepaschenko, D. (2012) Capability of C-Band SAR for Operational Wetland Monitoring at High Latitudes. *Remote Sens.*, 4(10), 2923-2943.

Bartsch, A., Trofaier, A.M., Hayman, G., Sabel, D., **Schlaffer, S.**, Clark, D.B., Blyth, E. (2012) Detection of open water dynamics with ENVISAT ASAR in support of land surface modelling at high latitudes. *Biogeosci.*, 9(2), 703-714.

Wimmer, F., **Schlaffer, S.**, a. d. Beek, T., Menzel, L. (2009) Distributed modelling of climate change impacts on snow sublimation in Northern Mongolia. *Adv. Geosci.*, 21, 117-124.

Peer review for *IEEE Trans. Geosci. Remote Sens.*, *IEEE J. Sel. Top. Appl. Earth Obs. Remote Sens.*, *Int. J. Appl. Earth Obs. Geoinf.*, *Int. J. Remote Sens.*, *Remote Sens. Lett.*, *Hydrol. Sci. J.*

## selected presentations

**Schlaffer, S.**, Dettmering, D., Chini, M. (2016) Relationships between C-band SAR backscatter and wetland water height from altimeter. *ESA Living Planet Symposium*, 9-13 May 2016, Prague, Czech Republic.

**Schlaffer, S.**, Wagner, W. (2015) Seasonal flood dynamics in a tropical wetland from multi-temporal ENVISAT ASAR data using harmonic analysis. Talk, *Mapping Water Bodies from Space*, 18-19 March 2015, ESA-ESRIN, Frascati, Italy.

**Schlaffer, S.**, Giustarini, G., Wagner, W. (2014) Impact of LiDAR-derived surface properties on SAR backscatter from flooded areas. *IEEE Int. Geosci. Remote Sens. Symp. (IGARSS)*, 13-18 July 2014, Quebec City, Canada.

**Schlaffer, S.**, Naeimi, V. (2014) Flood mapping at TU Vienna using multi-temporal SAR data – from ENVISAT to Sentinel-1. *4<sup>th</sup> Workshop of the Global Flood Working Group*, 4-6 April 2014, ECMWF, Reading, UK.

**Schlaffer, S.**, Hollaus, M., Wagner, W., Matgen, P. (2012) Flood delineation from synthetic aperture radar data with the help of a priori knowledge from historical acquisitions and digital elevation models in support of near-real-time flood mapping. *Proc. SPIE 8538*, 853813.

**Schlaffer, S.**, Kidd, R.A., Haas, E.M., Wagner, W. (2012) Validation of Geoland2 small water bodies product: methodological overview. *Geophys. Res. Abstr.*, 14, EGU2012-11225.

**Schlaffer, S.**, Paulik, C., Bartsch, A., Wagner, W. (2012) Microwave remote sensing of soil moisture and surface water. Invited talk, *GHG-Europe Peatland Synthesis Workshop*, Edinburgh, Scotland, UK, 21-23 November 2012.